

Summer 2015

# Resolving the Timing of Late Pleistocene Dome Emplacement at Mono Craters, California, from U–Th and Ar/Ar Dating

Mae Marcaida  
*San Jose State University*

Follow this and additional works at: [https://scholarworks.sjsu.edu/etd\\_theses](https://scholarworks.sjsu.edu/etd_theses)

---

## Recommended Citation

Marcaida, Mae, "Resolving the Timing of Late Pleistocene Dome Emplacement at Mono Craters, California, from U–Th and Ar/Ar Dating" (2015). *Master's Theses*. 4599.  
DOI: <https://doi.org/10.31979/etd.4rh3-fz5y>  
[https://scholarworks.sjsu.edu/etd\\_theses/4599](https://scholarworks.sjsu.edu/etd_theses/4599)

This Thesis is brought to you for free and open access by the Master's Theses and Graduate Research at SJSU ScholarWorks. It has been accepted for inclusion in Master's Theses by an authorized administrator of SJSU ScholarWorks. For more information, please contact [scholarworks@sjsu.edu](mailto:scholarworks@sjsu.edu).

RESOLVING THE TIMING OF LATE PLEISTOCENE DOME EMPLACEMENT AT  
MONO CRATERS, CALIFORNIA, FROM  $^{238}\text{U}$ - $^{230}\text{Th}$  AND  $^{40}\text{Ar}/^{39}\text{Ar}$  DATING

A Thesis

Presented to

The Faculty of the Department of Geology

San José State University

In Partial Fulfillment

of the Requirements for the Degree

Master of Science

by

Mae Marcaida

August 2015

© 2015

Mae Marcaida

ALL RIGHTS RESERVED

The Designated Thesis Committee Approves the Thesis Titled

RESOLVING THE TIMING OF LATE PLEISTOCENE DOME EMPLACEMENT AT  
MONO CRATERS, CALIFORNIA, FROM  $^{238}\text{U}$ - $^{230}\text{Th}$  AND  $^{40}\text{Ar}/^{39}\text{Ar}$  DATING

by

Mae Marcaida

APPROVED FOR THE DEPARTMENT OF GEOLOGY

SAN JOSÉ STATE UNIVERSITY

August 2015

Dr. Jonathan Miller                      Department of Geology

Dr. Robert Miller                        Department of Geology

Dr. Jorge Vazquez                        U.S. Geological Survey

## ABSTRACT

### RESOLVING THE TIMING OF LATE PLEISTOCENE DOME EMPLACEMENT AT MONO CRATERS, CALIFORNIA, FROM $^{238}\text{U}$ - $^{230}\text{Th}$ AND $^{40}\text{Ar}/^{39}\text{Ar}$ DATING

by Mae Marcaida

The Mono Craters chain in eastern California is one of the youngest sites of rhyolitic volcanism in North America and comprises at least 28 overlapping lava domes, flows, and tephra rings of mostly Holocene age. New U-series and  $^{40}\text{Ar}/^{39}\text{Ar}$  geochronological data presented here extend the age of the Mono Craters into the Late Pleistocene. Ion microprobe  $^{238}\text{U}$ - $^{230}\text{Th}$  isochron dating of unpolished rims of allanite and zircon and  $^{40}\text{Ar}/^{39}\text{Ar}$  laser fusion and step-heating dating of sanidine from the porphyritic biotite-bearing dome lavas of the Mono Craters yield Late Pleistocene ages, but the two techniques yield discordant results. The  $^{238}\text{U}$ - $^{230}\text{Th}$  isochron method gives ages of  $26 \pm 1.2$  ka,  $38 \pm 1.2$  ka, and  $42 \pm 1.1$  ka for domes 31 (newly recognized), 24, and 19, respectively, whereas the corresponding  $^{40}\text{Ar}/^{39}\text{Ar}$  sanidine ages are all older by an amount that exceed analytical errors. The anomalously older  $^{40}\text{Ar}/^{39}\text{Ar}$  sanidine ages are attributed to excess argon from incompletely degassed antecrysts and/or melt inclusions trapped in juvenile phenocrysts. Explosive eruptions preceded dome emplacement and produced tephra layers in the Wilson Creek formation of ancestral Mono Lake. The independently dated tephra layers can be correlated to the domes via titanomagnetite geochemistry. Correlation of specific tephras to the domes verifies that the  $^{238}\text{U}$ - $^{230}\text{Th}$  isochron rim ages of euhedral zircon and allanite provide the best estimates of eruption ages for the Mono Craters.

## ACKNOWLEDGEMENTS

I have been fortunate to have the mentorship of a number of dedicated scientists over the last several years. First, I thank my advisor, Dr. Jonathan Miller, who patiently listened to my project idea and expertly guided me into crafting that idea into a Master's thesis. I have benefited greatly from his wealth of knowledge and expertise in igneous petrology, and I treasure his remarkable insight. I also thank my committee member, Dr. Robert Miller who challenged me to recognize the importance of understanding the regional tectonics that cause volcanism in my study area.

This project would not have been possible without funding from the U.S. Geological Survey California Volcano Observatory and the support of my colleagues at the USGS. Dr. Margaret Mangan has been my supervisor and mentor for the last six years. I am most grateful for her endless encouragement and confidence in me. My main USGS collaborators are Dr. Jorge Vazquez and Dr. Andy Calvert, and I thank them both for their guidance. Jorge is my second committee member who has been as enthusiastic about this project as I have been from the beginning. He has motivated me to pursue several scientific questions and has been tireless in answering my own persistent questions. Andy has demonstrated remarkable patience in helping me understand the complicated world of mass spectrometry and argon geochronology.

In the various field and laboratory aspects of my project, I have received tremendous help from many people. I thank my energetic field assistants, Alyssa Rasis and Marsha Lidzbarski, as well as Dr. Wes Hildreth, who kindly accompanied us in our search for an elusive outcrop. I also thank Marcus Bursik, Manny Nathenson, and Solene

Pouget for their insightful help during our earlier field session. James Saburomaru, Dean Miller, and Katie Sullivan, the staff of the USGS  $^{40}\text{Ar}/^{39}\text{Ar}$  Laboratory in Menlo Park, were extremely patient in teaching me how to process samples for argon geochronology. Ben Haskins and Leslie Hayden graciously assisted me with grain mounts and carbon coating for SEM and microprobe analysis. I sincerely thank Dr. Matt Coble for his timely assistance at the USGS-Stanford SHRIMP lab. I thank Dr. Seth Burgess for sharing some key lab techniques and for helping me with the HF acid work. I also thank Dr. Mark Stelten, who kindly reviewed a section of my thesis and has taken the time to discuss my work.

Lastly, I am grateful to have had Heather Bleick in my life. She taught me everything I know in the laboratory and instilled in me the importance of good lab etiquette. She showed me how to use the electron microprobe, and she shared her data analysis techniques with me. She patiently listened to everything that I have to say, both academic and personal, and she always had the most sensible advice. I have become a better scientist and person because she had been both my mentor and my friend.

## TABLE OF CONTENTS

INTRODUCTION .....	1
GEOLOGICAL BACKGROUND.....	6
Geologic Setting.....	6
Previous Work .....	7
<i>Ages of domes of the Mono Craters .....</i>	<i>7</i>
<i>Ages of the Wilson Creek formation tephra layers.....</i>	<i>11</i>
<i>Age of Ash 15 and coeval geomagnetic excursion .....</i>	<i>14</i>
<i>Correlation between Mono Craters domes and the Wilson Creek tephra layers .....</i>	<i>15</i>
OBJECTIVES AND SIGNIFICANCE.....	18
BASIC PRINCIPLES OF DATING METHODS.....	19
$^{238}\text{U}$ - $^{230}\text{Th}$ disequilibrium dating of accessory minerals.....	19
$^{40}\text{Ar}/^{39}\text{Ar}$ dating of sanidine .....	23
METHODS .....	24
Sampling and sample description .....	24
Sample preparation .....	26
<i>Allanite and zircon extraction and processing.....</i>	<i>26</i>
<i>Sanidine extraction and processing .....</i>	<i>28</i>
Electron microprobe analysis.....	29
SIMS $^{238}\text{U}$ - $^{230}\text{Th}$ analysis .....	29
<i>Pre-analysis preparation.....</i>	<i>29</i>
<i>Analytical setup.....</i>	<i>30</i>

<i>Data treatment and correction</i> .....	31
<sup>40</sup> Ar/ <sup>39</sup> Ar analytical procedure: USGS <sup>40</sup> Ar/ <sup>39</sup> Ar Laboratory, Menlo Park, CA .....	35
<i>Data presentation</i> .....	37
RESULTS .....	38
Titanomagnetite chemistry .....	38
<sup>238</sup> U– <sup>230</sup> Th geochronology .....	40
<sup>40</sup> Ar/ <sup>39</sup> Ar geochronology .....	47
<i>Laser total-fusion analyses</i> .....	47
<i>Furnace incremental-heating analyses</i> .....	51
DISCUSSION .....	55
Eruption ages of domes of the Mono Craters .....	55
Wilson Creek tephras as independent age constraints for Mono Craters lavas .....	59
Late Pleistocene volcanism at Mono Craters and vicinity .....	60
CONCLUSIONS .....	64
REFERENCES CITED .....	66
APPENDIX 1: Expanded details of dating methods .....	74
APPENDIX 2: Backscattered electron images of all analyzed zircon and allanite .....	78
APPENDIX 3: Complete titanomagnetite data of dome 31, sample 14MCMM12 .....	89
APPENDIX 4: Complete sanidine <sup>40</sup> Ar/ <sup>39</sup> Ar laser total-fusion data .....	90
APPENDIX 5: Complete sanidine <sup>40</sup> Ar/ <sup>39</sup> Ar furnace incremental-heating data .....	93
APPENDIX 6: Complete sanidine data of dome 19, sample 11JAVMC06 .....	95

## LIST OF FIGURES

Figure 1. Aerial photograph of the Mono Lake–Long Valley region.....	2
Figure 2. General geologic map of the Mono Lake basin.....	3
Figure 3. General geologic map of the Mono Craters .....	8
Figure 4. The Wilson Creek formation and its geomagnetic excursion .....	12
Figure 5. Titanomagnetite data of Wilson Creek tephras and Mono Craters domes.....	17
Figure 6. General $^{238}\text{U}$ – $^{230}\text{Th}$ isochron diagram .....	22
Figure 7. Photos of sampled outcrops and Google Earth terrain image of dome 24 .....	25
Figure 8. Photos of dome 19 hand samples and clean sanidine phenocrysts.....	27
Figure 9. Representative secondary electron images of analyzed zircon and allanite.....	32
Figure 10. $^{238}\text{U}$ – $^{230}\text{Th}$ isochron diagrams of zircon and allanite standards .....	34
Figure 11. Titanomagnetite data of dome 31, sample 14MCMM12 .....	39
Figure 12. $^{238}\text{U}$ – $^{230}\text{Th}$ isochron diagram of dome 19, sample 11JAVMC06.....	44
Figure 13. $^{238}\text{U}$ – $^{230}\text{Th}$ isochron diagram of dome 24, sample 11MCMM05 .....	45
Figure 14. $^{238}\text{U}$ – $^{230}\text{Th}$ isochron diagram of dome 31, sample 14MCMM12 .....	46
Figure 15. Sanidine $^{40}\text{Ar}/^{39}\text{Ar}$ laser data of dome 19, sample 11JAVMC06.....	49
Figure 16. Sanidine $^{40}\text{Ar}/^{39}\text{Ar}$ laser data of dome 31, sample 14MCMM12 .....	50
Figure 17. Sanidine $^{40}\text{Ar}/^{39}\text{Ar}$ incremental data of dome 19, sample 11JAVMC06.....	53
Figure 18. Sanidine $^{40}\text{Ar}/^{39}\text{Ar}$ incremental data of dome 31, sample 14MCMM12.....	54
Figure 19. Schematic diagram of Late Pleistocene volcanism at Mono Craters .....	62

## LIST OF TABLES

Table 1. $^{238}\text{U}$ – $^{230}\text{Th}$ composition of zircon and allanite unpolished rims.....	41
Table 2. Summary of $^{40}\text{Ar}/^{39}\text{Ar}$ age results.....	48

## INTRODUCTION

The mid-Pliocene to Recent landscape east of the Sierra Nevada Mountains, in the Mono Lake–Long Valley region of eastern California (Fig. 1), was characterized by persistent volcanic activity with several successive and spatially discrete foci of silicic magmatism (Hildreth, 2004). One of the most recently active magmatic foci within the region is the Mono–Inyo Craters volcanic chain, a 30-km long chain of north-trending volcanic vents from the south shore of Mono Lake, extending through the western part of Long Valley caldera to north of Mammoth Mountain (Fig. 2). Mono Craters comprise the northern portion of the Mono–Inyo chain and form an arcuate, 17-km long group of about 28 overlapping lava domes, flows, and tephra rings. The Inyo Craters are a 12-km long chain of about seven volcanic features similar to the northern-lying Mono Craters. The record of Holocene volcanism at the Mono–Inyo chain is well constrained by tephrostratigraphy and radiocarbon dating (Wood, 1977; Miller, 1985; Sieh and Bursik, 1986; Bursik and Sieh, 1989, 2013). The youngest eruptions occurred from the northern end of the Mono Craters about 600 years ago, nearly contemporaneous with eruptions from the Inyo Craters to the south (Miller, 1985; Sieh and Bursik, 1986).

Volcanological studies of the Mono–Inyo Craters are relevant to hazard assessment in the Mono Lake–Long Valley region because of the very young age of volcanic activity involving multiple eruptions occurring within a short time span. A complete and reliable geochronological framework underpins assessments of long-term hazard probabilities. However, the geochronological framework of the Mono–Inyo chain remains largely incomplete; despite a relatively comprehensive Holocene tephra record

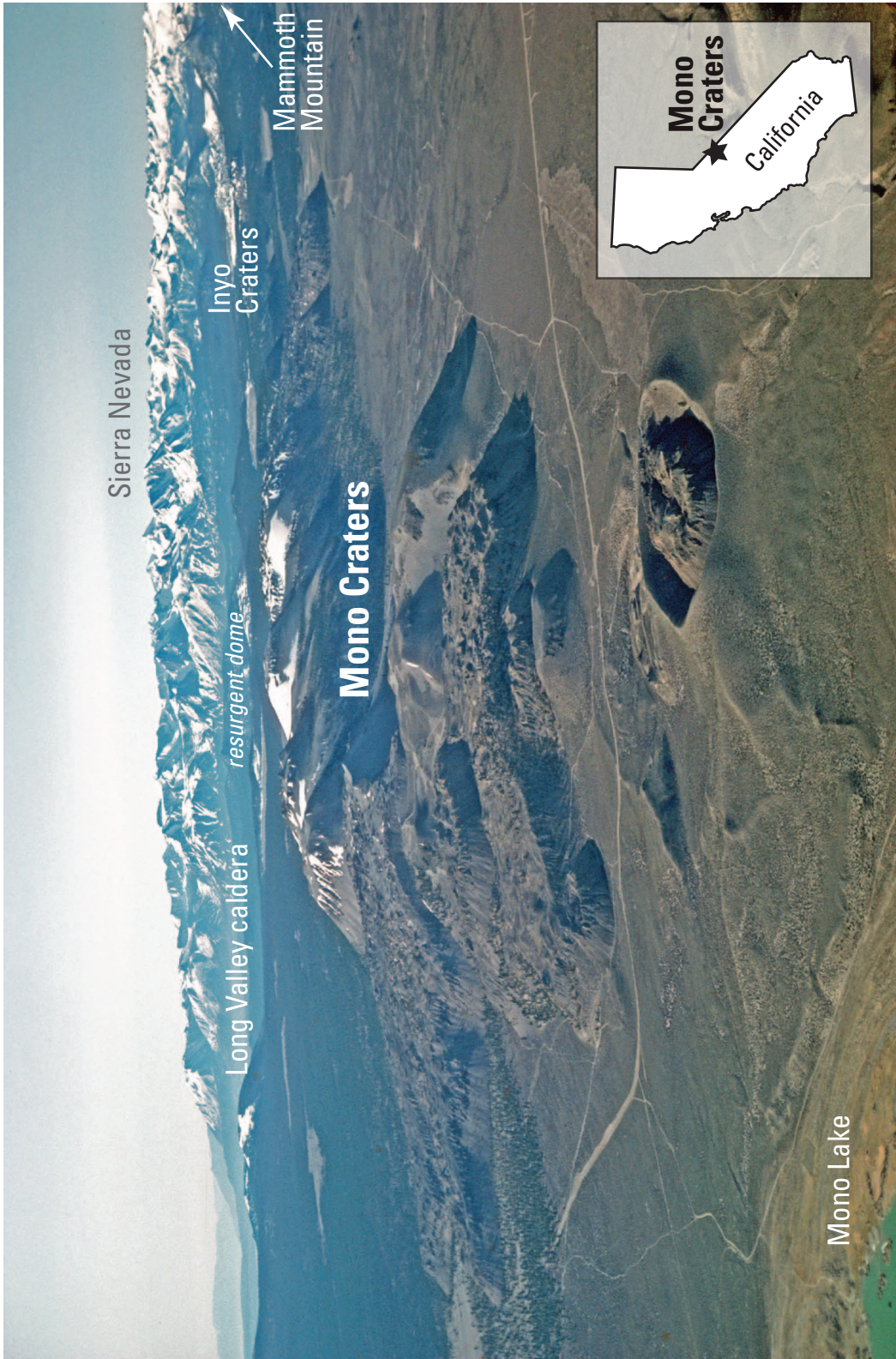


Figure 1. South-facing aerial view of the Mono Lake–Long Valley region, with the Mono Craters in the foreground and the Sierra Nevada in the background. The structurally-uplifted resurgent dome within Long Valley caldera is shown. USGS photo by D.P. Hill (1982).

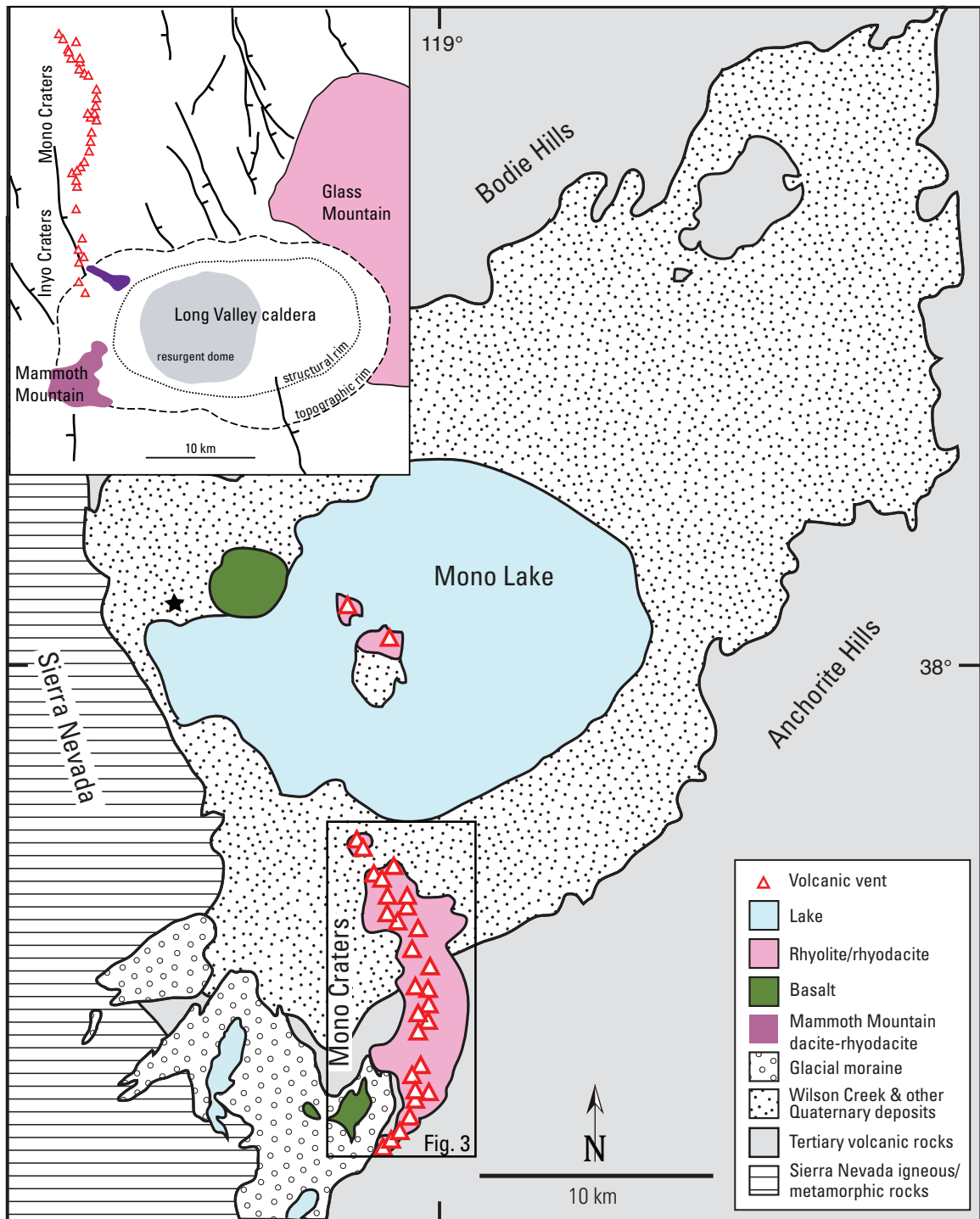


Figure 2. General geologic map of the Mono Lake basin late Quaternary volcanic features and lake deposits. Black star shows location of Figure 4. Inset: the Mono–Inyo chain and other features of the Mono Lake–Long Valley volcanic region; ca. 41–27 ka trachydacite lavas in purple; faults as heavy black lines with ticks on down-dropped block. Adapted from Kistler (1966), Lajoie (1968), Bailey (1989), and Hildreth (2004).

(Bursik and Sieh, 2013), it represents only the last 5000 years of the Mono–Inyo Craters eruptive history. In addition, the timing of late Pleistocene dome emplacement at Mono Craters is poorly resolved, with most of the chronology based on hydration-rind dating of obsidian (Wood, 1983; Bursik and Sieh, 1989). In order to better constrain the timing of early eruptive activity at Mono Craters, high-resolution geochronologic dating techniques were applied to domes with the most subdued morphology that likely represent the earliest rhyolitic dome emplacement events.

The geochronologic approach of this study was a combined  $^{238}\text{U}$ – $^{230}\text{Th}$  and  $^{40}\text{Ar}/^{39}\text{Ar}$  dating that provided two independent, but complementary, age constraints for the Mono Craters rhyolite domes:  $^{238}\text{U}$ – $^{230}\text{Th}$  zircon and allanite crystallization ages and  $^{40}\text{Ar}/^{39}\text{Ar}$  sanidine eruption ages. Zircon and allanite are common accessory minerals in the Mono Craters rhyolites and are ideal phases for dating by  $^{238}\text{U}$ – $^{230}\text{Th}$  disequilibrium methods because these minerals incorporate significant amounts of U and Th isotopes. Sanidine is a major mineral phase in the porphyritic rhyolite domes of the Mono Craters and is ideal for  $^{40}\text{Ar}/^{39}\text{Ar}$  dating because of its high K contents and its ability to retain radiogenic argon in its mineral structure below its closure temperature (Dalrymple and Lanphere, 1969; McDougall and Harrison, 1991). Because sanidine accumulates radiogenic argon only after post-eruptive cooling,  $^{40}\text{Ar}/^{39}\text{Ar}$  ages of sanidine are usually interpreted to date eruption. By contrast,  $^{238}\text{U}$ – $^{230}\text{Th}$  ages of igneous accessory minerals have generally been used to elucidate the timescales of crystallization in the magma chamber because diffusion of U and Th is negligible at magmatic temperatures (Vazquez and Reid, 2004; Cherniak, 2010). *In situ* analyses of unpolished grain faces of accessory

minerals that were in contact with melt can, in favorable cases (i.e., continuous crystallization in the interval leading to eruption), effectively date the eruption (e.g., Vazquez and Lidzbarski, 2012; Wright et al., 2015). Here, I present results from both dating techniques and argue that  $^{238}\text{U}$ – $^{230}\text{Th}$  ages of rims of coexisting zircon and allanite provide the best estimates of eruption ages for the Mono Craters rhyolites.

## **GEOLOGICAL BACKGROUND**

### **Geologic Setting**

The Mono Lake–Long Valley volcanic region is situated in the western margin of the Basin and Range Province (Bailey, 1989). Volcanism in the region began ca. 4 Ma ago with widespread eruptions of mafic and intermediate lavas accompanying the onset of large-scale normal faulting and formation of the eastern front of the Sierra Nevada (Bailey, 2004), followed by multiple high-silica rhyolitic eruptions from vents that formed the Glass Mountain complex (Fig. 2, inset; Metz and Mahood, 1985; Hildreth, 2004). The most prominent feature in the region is Long Valley caldera, which resides in a left-step of the major Sierra Nevada range-bounding faults (Fig. 2, inset; Bailey, 1989). Long Valley caldera formed as a result of the 770-ka eruption (Rivera et al., 2011) that produced 600 km<sup>3</sup> of compositionally zoned rhyolitic Bishop Tuff magma, accompanied by subsidence of a 15- by 30-km elliptical crustal block as the underlying magma chamber was partially evacuated (Hildreth and Mahood, 1986). Resurgent doming in the central part of Long Valley caldera occurred shortly afterwards, and postcaldera rhyolites were erupted within the caldera between ca. 750 ka and ca. 100 ka (Figs. 1 and 2; Hildreth, 2004). On the southwest topographic rim of the caldera, a series of dome-building eruptions between ca. 100 ka and ca. 50 ka, unrelated to the Long Valley magmatic system, formed the dacitic to rhyodacitic Mammoth Mountain lava dome complex, which vented west of the ring-fault structural margin of the caldera (Fig. 2, inset; Mahood et al., 2010; Hildreth et al., 2014). On the northwest topographic rim of the caldera, a southeast-trending chain of five trachydacite domes was emplaced from ca.

41–27 ka across the northwest moat (Fig. 2, inset; Mahood et al., 2010; Hildreth et al., 2014). North of the caldera, explosive rhyolitic eruptions began along the Mono–Inyo Craters volcanic chain as early as ca. 64 ka (Fig. 3; Vazquez and Lidzbarski, 2012), and the latest eruptions occurred about 500–600 years ago along the north and south end of the Mono–Inyo chain (Miller, 1985; Bursik and Sieh, 1989). These Holocene eruptions are hypothesized to have resulted from intrusion and venting of an 8–10-km-long, north-striking dike into the shallow crust (Sieh and Bursik, 1986; Bursik and Sieh, 1989). The Mono–Inyo Craters volcanic chain is recognized as chemically distinct from both the Long Valley and Mammoth Mountain magmatic systems and is one of the youngest areas of rhyolitic volcanism in the western United States (Hildreth, 2004).

## **Previous Work**

### ***Ages of domes of the Mono Craters***

An early study of the Mono Craters volcanic chain by Putnam (1938) suggested a Late Pleistocene age for the domes, flows, and tephra rings of the Mono Craters, based on his field observations of glacial moraine and lake shoreline relationships. Evernden and Curtis (1966) were the first to apply the K–Ar dating method to sanidine from Late Pleistocene volcanic rocks, and they reported ages of ca. 56 ka and ca. 5 ka for two Mono Craters domes. Subsequent K–Ar work by Dalrymple (1967) revised these earlier ages and included new K–Ar sanidine ages for seven additional rhyolite domes, with ages ranging from ca. 12 ka to ca. 6 ka (Fig. 3). For four of the same domes analyzed by Dalrymple (1967), Taddeucci et al. (1968) used the U-series disequilibrium dating method and measured the activities of U–Th isotopes in hornblende-glass pairs by alpha

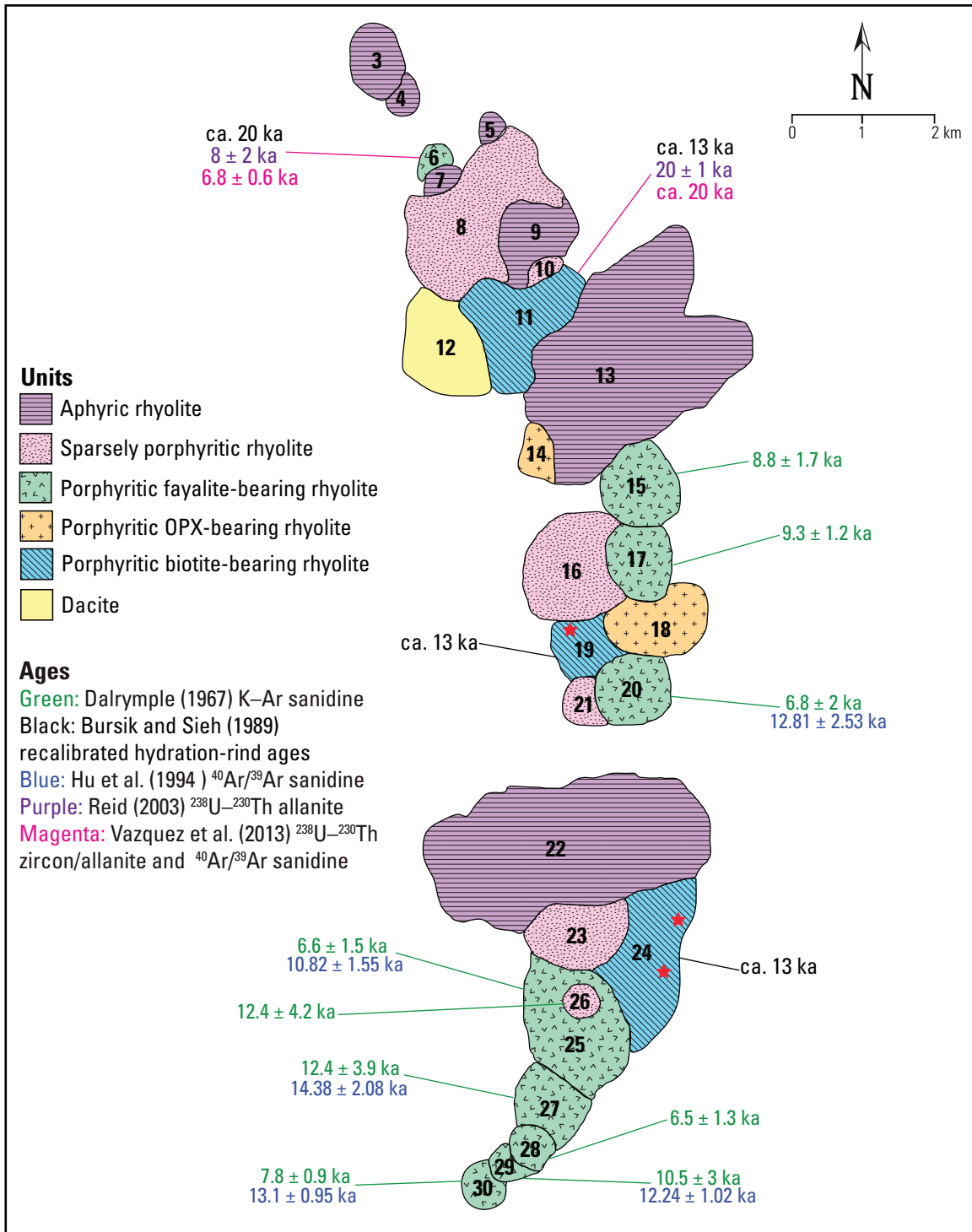


Figure 3. General geologic map of the the Mono Craters. Individual dome numbers are in black. Domes with published radiometric ages are indicated, along with the oldest domes from the chronology of Bursik and Sieh (1989). Red star indicates sampled site. Modified from Wood (1983) and Kelleher and Cameron (1990).

spectrometry. Their application of U-series dating in the Mono Craters yielded Holocene ages that are generally consistent with the K–Ar ages of Dalrymple (1967). Hydration-rind dating of obsidian from several domes and flows of the Mono Craters also yielded similar Holocene ages (Friedman, 1968). This method was developed by Friedman and Smith (1960) for dating obsidian artifacts, and it consists of measuring the thicknesses of rinds of hydrated glass, which form when atmospheric or soil moisture diffuses into a fresh glass surface. Calibrating the thickness data against the thickness of a material of known age produces a hydration rate. Friedman (1968) used a hydration rate of  $5 \mu^2/1000$  years, which he derived from Glass Mountain, Medicine Lake, California, to estimate the ages for obsidians from Mono Craters.

Following the work of Friedman (1968), Wood (1983) estimated the hydration-rind ages of twenty-six exposed Mono Craters domes and flows and constructed the first relatively complete chronology of the eruptive history of the Mono Craters volcanic chain. Because there is no consistent agreement between the existing K–Ar ages (Dalrymple, 1967), which could have been used for calibration, and his estimated hydration-rind ages, Wood (1983) used the hydration rate of  $5 \mu^2/1000$  years originally assumed by Friedman (1968) to convert the relative hydration-rind thicknesses to estimated ages for the Mono Craters. Bursik and Sieh (1989) sought to resolve this “less satisfactory” method of calibration by correlating a radiocarbon-dated tephra layer (Lajoie, 1968) to a hydration-rind-dated dome (Wood, 1983) with similar phenocryst assemblage. Their recalibrated obsidian hydration-rind chronology for the Mono Craters

suggests that, with few exceptions, nearly all domes and flows of the Mono Craters were extruded within the last 10,000 years (Fig. 3).

Kelleher and Cameron (1990) suggested that the sequence of dome emplacement at Mono Craters based on the current obsidian hydration rind ages (Bursik and Sieh, 1989) generally correlates with the textural and mineralogical groupings of the domes, which are numbered 3 to 30 from north to south (Fig. 3; Wood, 1983). Most of the Mono Craters are high-silica rhyolites (76–77 wt% SiO<sub>2</sub>), except for one dacitic dome (67–69 wt% SiO<sub>2</sub>) near the northern end of the chain (Carmichael, 1967; Lajoie, 1968; Kelleher and Cameron, 1990). Dacitic dome 12 is generally recognized as the oldest Mono Craters dome because its western flank is cut by an ancient shoreline of ancestral Mono Lake, whereas the lower elevation domes closer to the lake are not terraced (Lajoie, 1968; Wood, 1983; Bursik and Sieh, 1989). The high-silica rhyolitic domes are divided into textural subgroups (porphyritic, sparsely porphyritic, and aphyric; Wood, 1983). The porphyritic domes, subdivided into biotite-bearing, orthopyroxene-bearing, and fayalite-bearing lithologies by Kelleher and Cameron (1990), are apparently older than the sparsely porphyritic domes. The aphyric rhyolites are the youngest domes of the volcanic chain, based on well constrained radiocarbon ages of their tephra deposits, and were emplaced during two eruptive episodes at ca. 1.2 ka and ca. 0.6 ka (Wood, 1983; Sieh and Bursik, 1986).

Subsequent radiometric dating methods applied to select domes of the Mono Craters yielded results that do not agree with previous age estimates for the same domes based on the radiocarbon-calibrated hydration rind chronology (Bursik and Sieh, 1989).

$^{40}\text{Ar}/^{39}\text{Ar}$  step-heating experiments on sanidine from five domes with previous K–Ar analyses (Dalrymple, 1967) yielded  $^{40}\text{Ar}/^{39}\text{Ar}$  ages between ca. 14 ka and ca. 11 ka (Fig. 3; Hu et al., 1994).  $^{238}\text{U}$ – $^{230}\text{Th}$  dating of allanite using the ion microprobe yielded model ages that fall in the range of ca. 20 ka and ca. 7 ka for four Mono Craters domes (Reid, 2003). The most notable result of the U–Th study is the allanite crystallization age of  $8 \pm 2$  ka for the porphyritic fayalite-bearing dome 6 (Reid, 2003), which was previously inferred to be one of the oldest domes of the Mono Craters based on its recalibrated hydration rind age of ca. 20 ka (Bursik and Sieh, 1989). Recent, combined  $^{238}\text{U}$ – $^{230}\text{Th}$  dating on allanite and zircon rims and  $^{40}\text{Ar}/^{39}\text{Ar}$  dating on sanidine of domes 6 and 11 of the Mono Craters yielded concordant ages of ca. 7 ka and ca. 20 ka, respectively (Fig. 3; Vazquez et al., 2013), which are consistent with earlier  $^{238}\text{U}$ – $^{230}\text{Th}$  dating of allanite from the same domes (Reid, 2003). Concordance between ages derived from multiple dating methods indicate that dome 11 was likely emplaced at ca. 20 ka, much earlier than the apparently oldest dome 6, which has an early-Holocene age that is similar to those from K–Ar (Dalrymple, 1967) for some of the other fayalite-bearing domes (Fig. 3).

#### ***Ages of the Wilson Creek formation tephra layers***

The earliest signs of volcanic activity from the Mono Craters are preserved as numerous tephra layers intercalated with Late Pleistocene lakebeds of Mono Lake, informally known as the Wilson Creek formation (Figs. 2 and 4A; Lajoie, 1968). It is well exposed at the type locality along Wilson Creek, where there are nineteen distinct tephra layers numbered 1 through 19 from top to bottom of the section (Fig. 4A; Lajoie, 1968). These tephra layers provide important chronostratigraphic markers to correlate

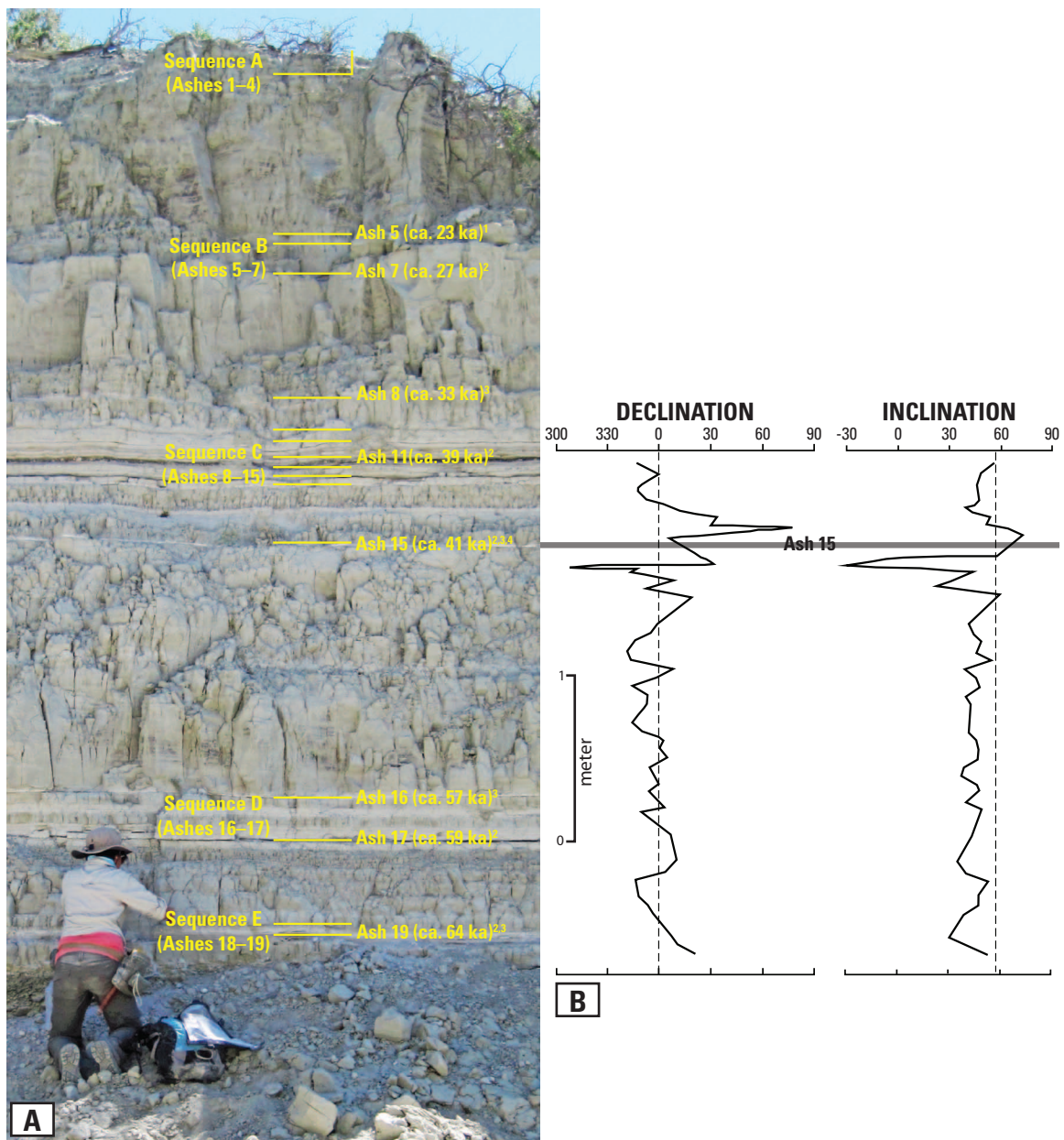


Figure 4. (A) The Wilson Creek formation at the type locality along Wilson Creek, with approximately the same scale as (B). Sequence A tephras have been eroded away in this outcrop. Representative ages of the tephras are shown: <sup>1</sup>Chen et al., 1996; <sup>2</sup>Vazquez and Lidzbarski, 2012; <sup>3</sup>Zimmerman et al., 2006; <sup>4</sup>Cox et al., 2012. Modified from Marcaida et al. (2014). USGS photo by M. Nathenson (2011). (B) Declination and inclination of the geomagnetic excursion recorded in the Wilson Creek formation measured and characterized by Liddicoat and Coe (1979). The eastward swing in declination and steepening of inclination is preceded by an even greater swing to westerly declination and shallow inclination. Ash 15 (indicated in gray) bisects the geomagnetic excursion. Modified from Liddicoat and Coe (1979).

the time series from Wilson Creek sediments to pluvial deposits elsewhere in the Great Basin and the western United States (e.g., Benson et al., 1990, 1998, 2003; Zimmerman et al., 2006, 2011).

Early studies using  $^{14}\text{C}$  dating of fossil ostracods constrained the age of the Wilson Creek formation to between ca. 23 ka and ca. 13 ka (Lajoie, 1968). Additional radiocarbon-age data on tufa (carbonate precipitate) and ostracods by Benson et al. (1990) extended the age of the base of the Wilson Creek formation to ca. 36 ka. Chen et al. (1996) directly dated two tephra layers (Ashes 5 and 12) using the  $^{40}\text{Ar}/^{39}\text{Ar}$  technique and reported a range of sanidine ages; they interpreted the youngest populations for each tephra layer as eruption ages because they are generally consistent with the stratigraphically equivalent  $^{14}\text{C}$  ages (Benson et al., 1990). However,  $^{14}\text{C}$  dating of carbonates and  $^{40}\text{Ar}/^{39}\text{Ar}$  dating of sanidine yielded discordant results for the portion of the Wilson Creek stratigraphy below Ash 5 due to open-system contamination by modern carbon (Hajdas et al., 2004) and the presence of xenocrysts and/or excess argon (Kent et al., 2002; Zimmerman et al., 2006; Cassata et al., 2010). For example, all analyzed sanidine from Ash 8 yielded apparent  $^{40}\text{Ar}/^{39}\text{Ar}$  ages between ca. 808 ka and ca. 763 ka, which Kent et al. (2002) interpreted as xenocrystic sanidine from the Bishop Tuff through which Ash 8 likely erupted. Kent et al. (2002) also obtained a wide range of  $^{40}\text{Ar}/^{39}\text{Ar}$  sanidine ages for Ashes 15 and 16 that are significantly older than the radiocarbon ages for carbonates at the same stratigraphic level. Subsequent  $^{40}\text{Ar}/^{39}\text{Ar}$  analyses by Zimmerman et al. (2006) for Ash 16, and Cassata et al. (2010) for Ashes 13, 15, and 19, found similar multimodal sanidine age populations within each tephra layer, which were

interpreted by all as resulting from xenocrystic contamination and/or excess argon from juvenile phenocrysts. Consequently, the youngest sanidine populations for each tephra layer were considered maximum constraints on depositional ages instead of eruption ages (Kent et al., 2002; Zimmerman et al., 2006, 2011; Cassata et al., 2010).

Because the published age constraints for the stratigraphy below Ash 5 were unreliable, Zimmerman et al. (2006) correlated the relative magnetic paleointensity record of Wilson Creek sediments to the age-calibrated Global Paleointensity Stack as an independent method of estimating the ages of the Wilson Creek formation. Their paleointensity-based ages are ca. 25–67 ka for the portion of the stratigraphy between Ashes 5 and 19, which increased the age of the base of the Wilson Creek formation from ca. 36 ka to ca. 67 ka (Fig. 4A). High-resolution tephrochronology work by Vazquez and Lidzbarski (2012) yielded stratigraphically consistent ages that are concordant with the magnetostratigraphy of Zimmerman et al. (2006). Using U–Th dating of crystal surfaces, Vazquez and Lidzbarski (2012) determined ages of allanite and zircon rims from pumice pyroclasts. Their results indicate that Ashes 7–19 were erupted between ca. 27 ka and ca. 64 ka, although ages of zircon antecryts in the tephras extend back to ca. 90–100 ka (see also, Cassata et al., 2010).

#### ***Age of Ash 15 and coeval geomagnetic excursion***

Ash 15 was erupted during a prominent geomagnetic excursion recorded in the Wilson Creek formation (Fig. 4B; Denham and Cox, 1971; Liddicoat and Coe, 1979) and is an important chronostratigraphic marker for paleomagnetic and paleoclimatic studies in the western United States (e.g., Benson et al., 1990, 1998; Zimmerman et al., 2006). The

original  $^{14}\text{C}$ -based chronology led to the conclusion that the age of Ash 15 and its coeval excursion was ca. 25 ka. Because of its unique age relative to the previously identified Laschamp event (Bonhommet and Zahringer, 1969), this excursion was named the “Mono Lake” excursion (Denham and Cox, 1971; Liddicoat and Coe, 1979). Additional radiocarbon dating, as well as correlation of Ash 15 to tephra interbedded with Pleistocene lake sediments in Nevada, refined the age of the Mono Lake excursion to ca. 32 ka (Benson et al., 2003).

Two geomagnetic excursions recorded in deep-sea sediments dated at ca. 32 ka and ca. 41 ka were correlated to the Mono Lake and Laschamp excursions, respectively (Chanell et al., 2006). The ca. 41 ka Laschamp event has been independently dated in lavas at its type locality near Laschamp and Olby, France (Singer et al., 2009). Recent direct dating of Ash 15 using (U–Th)/He (Cox et al., 2012) and U–Th methods (Vazquez and Lidzbarski, 2012) each yielded ages of ca. 40–41 ka, which agree with the relative paleointensity-based age of ca. 40 ka (Zimmerman et al., 2006), indicating that the geomagnetic excursion bisected by Ash 15 is instead a record of the global Laschamp event as originally proposed by Kent et al. (2002) and Zimmerman et al. (2006).

#### ***Correlation between Mono Craters domes and the Wilson Creek tephra layers***

Because of their proximity, the Mono Craters have long been recognized as the sources for the rhyolitic tephra in the Wilson Creek formation (e.g., Lajoie, 1968; Wood, 1983). However, few attempts had been made to correlate the tephra layers to specific Mono Craters domes because of the relative homogeneity of their respective whole-rock and glass compositions (Lajoie, 1968; Kelleher and Cameron, 1990; Madsen et al., 2002;

Benson et al., 2003). In addition, the available geochronological data indicate that most of the Mono Craters are <20 ka (Dalrymple, 1967; Wood, 1983; Bursik and Sieh, 1989; Hu et al., 1994), whereas most of the Wilson Creek tephras are >20 ka (Chen et al., 1996; Zimmerman et al., 2006; Vazquez and Lidzbarski, 2012). This apparent lack of age overlap has led researchers to conclude that most, if not all, of the source vents to the Wilson Creek tephras, are now buried by the currently exposed domes (e.g., Bursik and Sieh, 1989). However, a reappraisal of this interpretation is in order, in light of results from a recent detailed study of the Wilson Creek stratigraphy by Marcaida et al. (2014), which demonstrates that compositions of titanomagnetite crystals in the tephras provide unique geochemical fingerprints for most of the tephra-producing eruptions of the Mono Craters during the Late Pleistocene. Furthermore, Marcaida et al. (2014) identified three potential source vents using this fingerprinting technique, suggesting that multiple domes in the Mono Craters chain reflect volcanism older than 20 ka. Specifically, similar compositions of titanomagnetite from both pumice and lava potentially correlate several Wilson Creek tephra layers to porphyritic biotite-bearing domes 11, 24, and 19 of the Mono Craters (Fig. 5; Marcaida et al. 2014). Similar ca. 20 ka ages for dome 11 and Ash 3 support the titanomagnetite correlation (Fig. 5A; Vazquez et al., 2013). Dome 19 has titanomagnetite with similar bimodal chemistry to titanomagnetites from Ash 15 (Fig. 5B), whereas dome 24 has three potential correlative tephra layers based on indistinguishable titanomagnetite chemistry (Fig. 5C; Marcaida et al., 2014).

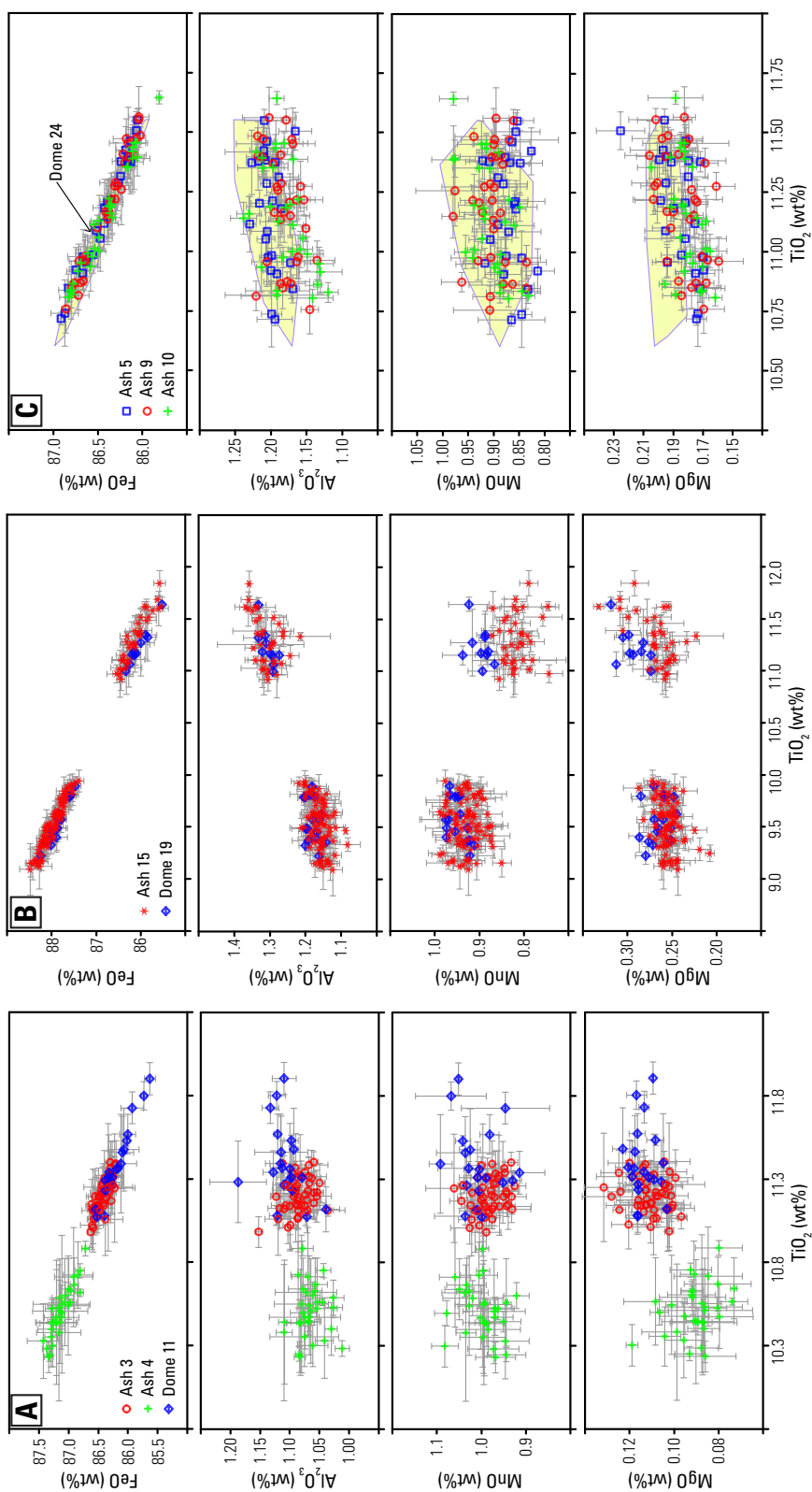


Figure 5. Major- and minor-element titanomagnetite chemistry of select Wilson Creek tephra layers showing closely matching compositions with (A) dome 11, (B) dome 19, and (C) dome 24 (yellow polygon) of the Mono Craters. Each data point is the mean and standard deviation of one titanomagnetite crystal analyzed in three different spots using the electron microprobe. Modified figure and caption from Marcaida et al. (2014).

## OBJECTIVES AND SIGNIFICANCE

The overall goal of this study is to provide a new geochronological framework for Late Pleistocene volcanism at Mono Craters that integrates the revised chronology of the Wilson Creek stratigraphy (Zimmerman et al., 2006; Vazquez and Lidzbarski, 2012) and new radiometric ages for select Mono Craters domes (this study). I focus on the apparently oldest rhyolitic domes (Wood, 1983; Bursik and Sieh, 1989) that are potential source vents to several Wilson Creek tephra layers, specifically, the porphyritic biotite-bearing domes 19 and 24 of the Mono Craters (Marcaida et al., 2014). That dome 19 is likely the extrusive equivalent of Ash 15 based on titanomagnetite correlation is particularly significant, as geochronological work on dome 19 provides an independent method of dating the geomagnetic excursion bisected by the tephra. In addition, because dome 24 may have been the source vent for several Wilson Creek tephra layers, it is possible that dome 24 is a composite dome and may represent multiple eruptions.

The specific objectives of this study are to:

1. Determine eruption ages for domes 19 and 24 of the Mono Craters using combined  $^{40}\text{Ar}/^{39}\text{Ar}$  dating on sanidine with  $^{238}\text{U}$ - $^{230}\text{Th}$  dating on zircon and allanite rims, which dates the final increment of crystallization prior to eruption.
2. Determine if dome 24 of the Mono Craters is a composite dome based on data obtained from reconnaissance aerial terrain imagery, electron microprobe analysis of titanomagnetite, and combined U-series and Ar/Ar geochronology.

## BASIC PRINCIPLES OF DATING METHODS

### $^{238}\text{U}$ – $^{230}\text{Th}$ disequilibrium dating of accessory minerals

$^{238}\text{U}$  decays to stable  $^{206}\text{Pb}$  through a series of short-lived daughter isotopes, which are themselves radioactive, with half-lives ( $t_{1/2}$ ) ranging from seconds to several hundred thousand years. In this decay chain, the longest-lived intermediate nuclides are  $^{234}\text{U}$  ( $t_{1/2} = 245$  ka) and its daughter  $^{230}\text{Th}$  ( $t_{1/2} = 75.7$  ka). Because the half-lives of the intermediate nuclides are much shorter relative to the parent  $^{238}\text{U}$  ( $t_{1/2} = 4.5$  Ga), any U-bearing system will eventually reach a state of secular equilibrium, whereby the rates of decay or activities (number of atoms multiplied by the decay constant) of all radionuclides become unity. However, natural geological processes disturb the system by separating the radioactive daughters from their parents and from each other because of differences in their chemical properties. After such disturbance, the system eventually returns to secular equilibrium after about five half-lives of the longest-lived intermediate daughter nuclide. For any specific parent-daughter pair in the decay chain, the time required to return to secular equilibrium is the useful time range for dating; application of  $^{238}\text{U}$ – $^{230}\text{Th}$  disequilibrium dating is thus limited to rocks younger than ca. 375 ka (or five half-lives of daughter  $^{230}\text{Th}$ ).

During magmatic processes, the daughter isotope  $^{234}\text{U}$  is not fractionated chemically from the parent  $^{238}\text{U}$ ; therefore  $^{238}\text{U}$  and  $^{234}\text{U}$  are always effectively in secular equilibrium, i.e., their activities are equal. Because U and Th are different chemical species, the daughter isotope  $^{230}\text{Th}$  is fractionated from U during magmatic processes, which results in parent-daughter disequilibrium. In evolved melts, for example,

crystallization of accessory minerals such as zircon and allanite strongly fractionates U and Th because of contrasting mineral-melt partition coefficients (Mahood and Hildreth, 1983). U is preferentially concentrated in zircon relative to Th, and Th is much more strongly enriched in allanite than U. Thus, zircon and allanite initially crystallize in a state of pronounced radioactive disequilibrium relative to the melt, and this makes these phases ideal for *in situ* dating by  $^{238}\text{U}$ – $^{230}\text{Th}$  disequilibrium methods (e.g. Reid et al., 1997; Vazquez and Reid, 2004; Vazquez and Lidzbarski, 2012).

After crystallization, the isotopic abundances of U and Th in a mineral phase change only in response to radioactive decay and ingrowth. Thus, the net activity of  $^{230}\text{Th}$  is the sum of  $^{230}\text{Th}$  ingrowth from U decay and the initial  $^{230}\text{Th}$ :

$$(^{230}\text{Th}) = (^{238}\text{U})(1 - e^{-\lambda_{230}t}) + (^{230}\text{Th})(e^{-\lambda_{230}t}) \quad (1)$$

Where activities of  $^{238}\text{U}$  and  $^{230}\text{Th}$  are denoted in parentheses,  $\lambda_{230}$  is the decay constant of  $^{230}\text{Th}$  and  $t$  is the age of the crystallization. Because most naturally occurring Th exists as  $^{232}\text{Th}$  ( $t_{1/2} = 14$  Ga), its activity is effectively constant over the timescales of  $^{230}\text{Th}$  disequilibrium, and so Equation 1 is normalized to the activity of  $^{232}\text{Th}$ :

$$\frac{(^{230}\text{Th})}{(^{232}\text{Th})} = \frac{(^{238}\text{U})}{(^{232}\text{Th})}(1 - e^{-\lambda_{230}t}) + \frac{(^{230}\text{Th})}{(^{232}\text{Th})}(e^{-\lambda_{230}t}) \quad (2)$$

The above equation allows the use of the Th isotope isochron diagram (Kigoshi, 1967; Allègre, 1968) to date the event that produced the disequilibrium, which, in the case of accessory minerals, is crystallization. The basic assumption is that crystallization occurred over very brief timescales relative to the half-life of  $^{230}\text{Th}$ . With this assumption, any mineral that crystallized from the same magma at the same time would

have the same initial  $(^{230}\text{Th})/(^{232}\text{Th})$  but with variable  $(^{238}\text{U})/(^{232}\text{Th})$  in an isochron diagram. On a plot of  $(^{230}\text{Th})/(^{232}\text{Th})$  versus  $(^{238}\text{U})/(^{232}\text{Th})$ , cogenetic minerals would thus define a linear array (isochron) whose slope  $m$  is a function of time (Fig. 6). The age of crystallization  $t$  is calculated from the slope:

$$t = -\frac{\ln(1-m)}{\lambda_{230}} \quad (3)$$

The isotopic abundance of initial  $^{230}\text{Th}$  is constrained by the intercept of the isochron with the equiline or the line of equal  $(^{230}\text{Th})/(^{232}\text{Th})$  and  $(^{238}\text{U})/(^{232}\text{Th})$ , i.e., the line representing secular equilibrium (Fig. 6). As time passes after initial crystallization and excess  $^{238}\text{U}$  or  $^{230}\text{Th}$  decays, the isochron rotates about its point of intersection (equipoint) with the equiline as the system evolves and moves towards secular equilibrium. Because of the much longer half-lives of  $^{238}\text{U}$  and  $^{232}\text{Th}$  relative to  $^{230}\text{Th}$ ,  $(^{230}\text{Th})/(^{232}\text{Th})$  either increases or decreases depending on the initial sense of disequilibrium, whereas  $(^{238}\text{U})/(^{232}\text{Th})$  remains essentially constant, i.e., points move in a vertical trajectory up or down the equiline until the system reaches secular equilibrium at ca. 375 ka (Fig. 6).

$^{238}\text{U}$ - $^{230}\text{Th}$  dating of accessory minerals using secondary ion mass spectrometry (SIMS) has been documented in numerous studies (e.g., Reid et al., 1997; Bacon et al. 2000; Lowenstern et al., 2000; Reid and Coath, 2000; Charlier et al., 2003; Vazquez and Reid, 2004; Schmitt and Vazquez, 2006; Simon et al., 2009; Vazquez and Lidzbarski, 2012; Stelten et al., 2013; Coombs and Vazquez, 2014; Vazquez et al., 2014; Wright et al., 2015). Details of  $^{238}\text{U}$ - $^{230}\text{Th}$  dating method using SIMS are in Appendix 1.

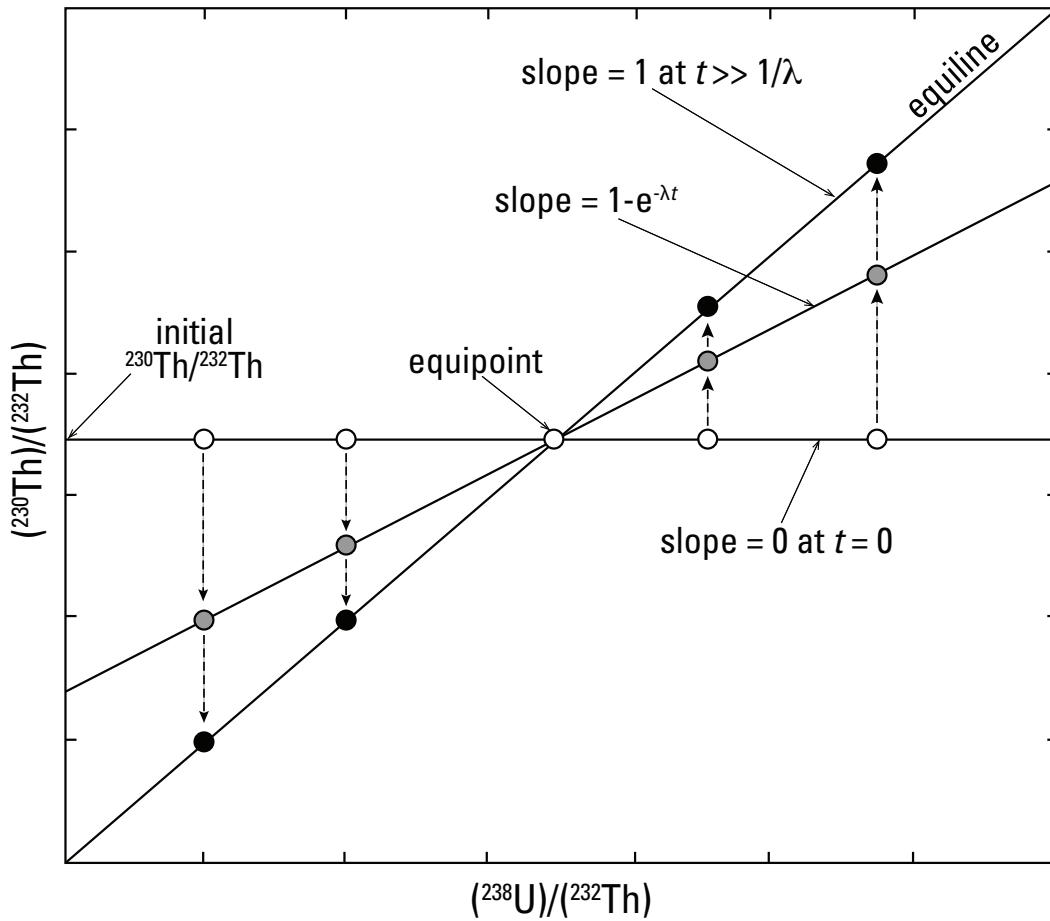


Figure 6. Isotopic evolution of isochronous rocks or minerals on the  $(^{230}\text{Th})/(^{232}\text{Th})$  vs.  $(^{238}\text{U})/(^{232}\text{Th})$  isochron diagram. Symbols: white circles are cogenetic samples with variable U/Th at the time of initial fractionation ( $t = 0$ ); gray circles represent samples after elapsed time,  $t > 0$ ; black circles represent samples after ca. 375 ka ( $t \gg 1/\lambda$ ), where samples are at secular equilibrium (represented by the equiline). Allanite with low U/Th ratio plots to the left of the equipoint, whereas zircon with high U/Th ratio plots to the right of the equipoint. After Dickin (2005).

## **$^{40}\text{Ar}/^{39}\text{Ar}$ dating of sanidine**

$^{40}\text{K}$  ( $t_{1/2} = 1.25 \text{ Ga}$ ) is a naturally occurring radioactive isotope of K that undergoes a dual decay to stable daughter isotopes  $^{40}\text{Ca}$  and  $^{40}\text{Ar}$ . Although only <11% of  $^{40}\text{K}$  decays to radiogenic argon ( $^{40}\text{Ar}^*$ ), this branch of the  $^{40}\text{K}$  decay process is the basis of the K–Ar isotopic dating method, from which the  $^{40}\text{Ar}/^{39}\text{Ar}$  dating method is derived (Dalrymple and Lanphere, 1969; McDougall and Harrison, 1999).

In principle, the age of any K-bearing sample is determined from the ratio of the amount of parent isotope  $^{40}\text{K}$  and the amount of daughter isotope  $^{40}\text{Ar}^*$  accumulated over geologic time. Because Ar, as a noble gas, diffuses relatively easily at magmatic temperatures, the accumulation of  $^{40}\text{Ar}^*$  in volcanic rocks (and constituent minerals) only begins upon eruption and rapid cooling to temperatures below which Ar diffusion is negligible (McDougall and Harrison, 1999). If the erupted magma has degassed completely and cooled in equilibrium with the atmosphere, any pre-existing (“initial”)  $^{40}\text{Ar}^*$  isotopes are lost, and the initially trapped Ar is atmospheric (non-radiogenic) in composition. Sanidine feldspar is common in high- $\text{SiO}_2$  dacitic to rhyolitic rocks and is often used for dating an eruption because its compact crystal structure limits the incorporation of initial Ar at magmatic temperatures (e.g., Renne, 1997), and it quantitatively retains all the  $^{40}\text{Ar}^*$  produced within it after cooling and crystallization.

Details of the  $^{40}\text{Ar}/^{39}\text{Ar}$  dating method are in Appendix 1.

## **METHODS**

### **Sampling and sample description**

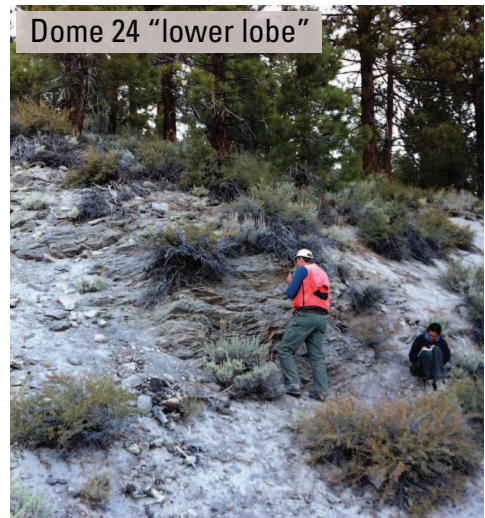
Domes 19 and 24 of the Mono Craters have relatively subdued morphology with limited exposures because they are thickly mantled by tephra from the most recent eruptions of the Mono Craters. Sampling was done in two field sessions on October 2011 and July 2014. Great care was taken to locate outcrops that were in place and to collect samples that show no significant weathering. Several kilograms of rocks were collected from unweathered interiors of dome outcrops near the top of dome 19 (sample 11JAVMC06; Fig. 7A), whereas samples from dome 24 were collected in road cut exposures near Pumice Mine Road (sample 11MCMM05; Figs. 7B and 7C). This was the same outcrop sampled as dome 24 by Wood (1983) and Kelleher (1986), based on sample site descriptions in their respective publications.

Aerial terrain imagery of dome 24 reveals two distinct lava flow lobes (Fig. 7C); the upper lobe of lava appears to crosscut the lower lobe of lava, which was sampled in the earlier field session (Fig. 7B). In July 2014, despite relatively dense tree cover, an outcrop of the upper lava flow lobe was found and sampled due north of the channel separating the distinct flow lobes (sample 14MCMM12; Figs. 7C and 7D). In the subsequent section, the two lava flow lobes of dome 24 are referred to as dome 24 “lower lobe” (sample 11MCMM05) and dome 24 “upper lobe” (sample 14MCMM12).

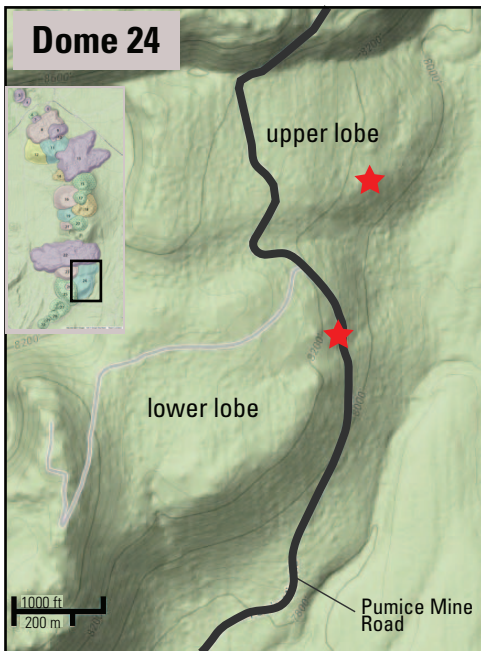
Complete petrographic and mineralogical descriptions of domes 19 and 24 of the Mono Craters are in Kelleher (1986) and Kelleher and Cameron (1990). In general, the porphyritic biotite-bearing domes 19 and 24 contain 8–10% phenocrysts of



**A**



**B**



**C**



**D**

Figure 7. Field photos of sampled domes and Google Earth terrain image of dome 24. (A) Sampled outcrop near the top of the dome 19, and (B) sampled outcrop of dome 24 along Pumice Mine Road. Photos taken in October 2011. (C) Aerial terrain image of dome 24 showing two distinct lava flow lobes, with the “upper lobe” crosscutting the “lower lobe”. Red star indicates location of sampled outcrops shown in (B) and (D). Inset map in (C) shows location of dome 24 relative to the rest of the Mono Craters domes. (D) An outcrop of the upper lava flow lobe sampled in July 2014. See Figure 3 for site locations on the Mono Craters map and Table 1 for sample numbers and GPS coordinates.

predominantly quartz, sanidine, and plagioclase, with minor amounts of biotite, hornblende, and titanomagnetite, and common accessory minerals allanite and zircon.

### **Sample preparation**

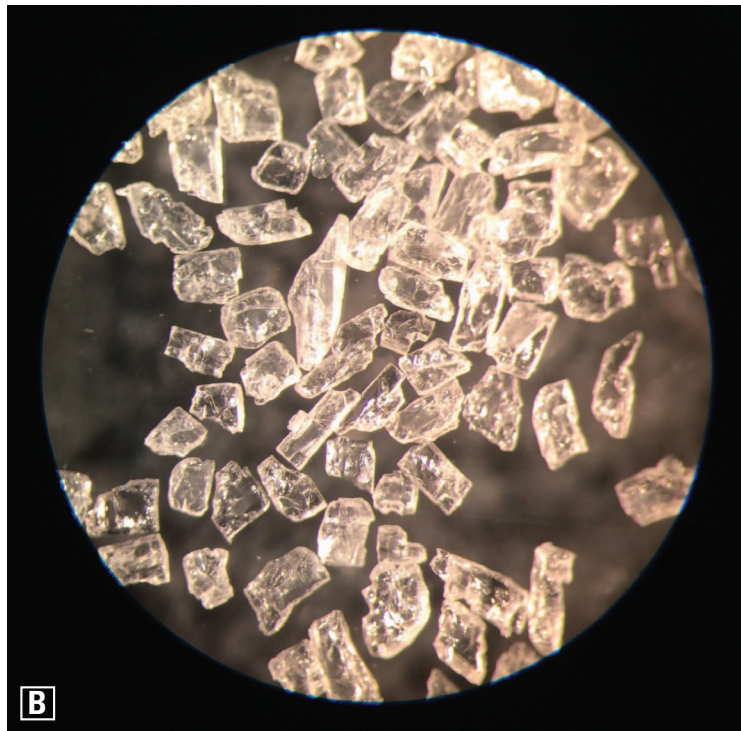
About one kilogram of dome rocks (Fig. 8A) for each sample was crushed using a hammer and metal plate, broken down to sand-sized particles using a roller mill, dry-sieved to different size fractions, washed in deionized water using an ultrasonic bath, and dried in an oven. The 500–1000  $\mu\text{m}$  size fraction was processed for sanidine phenocrysts, whereas the  $<500$   $\mu\text{m}$  size fraction was processed for accessory minerals. Ferromagnetic minerals (e.g., titanomagnetite) within both size fractions were removed with a strong permanent magnet before further processing. The extracted titanomagnetite for samples 11JAVMC06 (dome 19) and 11MCMM05 (dome 24 “lower lobe”) had been analyzed earlier, and their compositional data were reported in Marcaida et al. (2014).

### ***Allanite and zircon extraction and processing***

The ultrasonic probe was used to disaggregate the  $<500$   $\mu\text{m}$  bulk sample, and fine particles in suspension were decanted. After drying, the remaining material was split into two fractions based on their magnetic susceptibilities using the Frantz Isodynamic Magnetic Separator. The heavy minerals were obtained by standard density separation techniques using methylene iodide with density set to  $\sim 3.0$   $\text{g}/\text{cm}^3$ . After heavy liquid separation, the heavy mineral fraction was thoroughly rinsed with acetone and deionized water in an ultrasonic bath, then air-dried. Allanite (density  $>3.5$   $\text{g}/\text{cm}^3$ ) was concentrated in the more magnetic fraction (i.e., magnetic at 0.5 amperes), whereas zircon (density  $>4.5$   $\text{g}/\text{cm}^3$ ) was preferentially concentrated in the less magnetic fraction



**A**



**B**

Figure 8. (A) Approximately one kilogram of hand-sampled pieces from dome 19 (sample 11JAVMC06) processed for sanidine and accessory minerals zircon and allanite. (B) Clean, hand-picked sanidine separates from dome 24 “upper lobe” (sample 14MCMM12). Grain sizes range from 500–1000  $\mu\text{m}$ .

(i.e., nonmagnetic at 0.5 amperes). Individual allanite and zircon grains were handpicked under a binocular microscope. Although invariably broken, selected allanite grains had exposed crystal faces. Because most zircons were  $<100\ \mu\text{m}$  and encased in groundmass glass, handpicked zircon grains were bathed in full strength (48%) hydrofluoric (HF) acid for  $\sim 3$  minutes to remove adhering glass.

### ***Sanidine extraction and processing***

The Frantz Isodynamic Magnetic Separator was used up to 1.5 amperes to concentrate the nonmagnetic fraction, which isolated feldspar and quartz from glass fragments and other phenocrysts. To separate sanidine from quartz and plagioclase, heavy liquid density techniques were used: methylene iodide was set to a density of  $2.59\ \text{g/cm}^3$ , which floated sanidine ( $2.57\ \text{g/cm}^3$ ) and sank quartz ( $2.65\ \text{g/cm}^3$ ) and plagioclase ( $2.63\text{--}2.77\ \text{g/cm}^3$ ). This was followed by thorough cleaning using acetone and deionized water in an ultrasonic bath. To remove adhering glass, sanidine separates were etched in dilute ( $\sim 8\%$ ) HF acid using an ultrasonic bath for gentle disaggregation, thoroughly rinsed in deionized water, and then air-dried. Sample 11MCMM05 (dome 24 “lower lobe”) yielded  $<30$  mg of sanidine after processing, which was not enough for  $^{40}\text{Ar}/^{39}\text{Ar}$  analysis. This was likely due to an incorrect methylene iodide density setting during heavy liquid separation of this particular sample. For samples 11JAVMC06 (dome 19) and 14MCMM12 (dome 24 “upper lobe”),  $\sim 100$  sanidine grains were handpicked under a binocular microscope for  $^{40}\text{Ar}/^{39}\text{Ar}$  laser fusion technique (Fig. 8B), with an additional 50–60 mg of clean sanidine grains handpicked for incremental heating technique.

### **Electron microprobe analysis**

To evaluate the hypothesis that two distinct lava flow lobes comprise dome 24, titanomagnetite crystals from the “upper lobe” (sample 14MCMM12) of dome 24 were mounted in epoxy, polished, and carbon-coated for electron microprobe analysis. Thirty-seven titanomagnetite crystals were analyzed following the methods and analytical setup of Marcaida et al. (2014). New titanomagnetite compositional data for sample 14MCMM12 were obtained using the JEOL 8900 electron microprobe at the U.S. Geological Survey (USGS) in Menlo Park, California, and were compared to the published titanomagnetite data of the “lower lobe” of dome 24 (sample 11MCMM05; Marcaida et al., 2014).

### **SIMS $^{238}\text{U}$ – $^{230}\text{Th}$ analysis**

#### ***Pre-analysis preparation***

Selected allanite and zircon grains were mounted with reference standards of known age and composition for “rim” (unpolished crystal surface) analysis at the Stanford–USGS Micro Analysis Center. Allanite grains from dome 19 (sample 11JAVMC06) and dome 24 “lower lobe” (sample 11MCMM05) were pressed into soft polished indium metal with crystal faces parallel to the mount surface, whereas allanite grains from dome 24 “upper lobe” (sample 14MCMM12) were mounted in standard epoxy mount for minimal grinding (with 2000 grit for ~15 min) and polishing to remove adhering glass and expose crystal faces. Individual zircon crystals for each sample were embedded in indium metal and required no polishing after HF-acid treatment. To create a sample map for use during analysis, all mounts were imaged using reflected light with a

petrographic microscope. To remove surface contaminants prior to placement in the instrument, the sample mounts were thoroughly cleaned with soapy water, 1 M hydrochloric acid, and/or an EDTA solution, and rinsed in deionized water. After drying in a vacuum oven for ~15 min, the sample mounts were coated with a thin (~10 nm) layer of gold to produce a conductive surface.

### ***Analytical setup***

Allanite and zircon SIMS analyses were conducted using the Stanford–USGS Sensitive High-Resolution Ion Microprobe with Reverse Geometry (SHRIMP–RG; Bacon et al., 2012) in two analytical sessions (April 2014 and March 2015) with identical setup. A primary ion beam of  $O_2^-$  with intensities of 15–25 nA and accelerating voltage of 10 kV was focused into a ~40  $\mu\text{m}$  diameter spot of sample surface and was rastered for ~10 seconds to remove any surface contaminants, including the gold coat, before analysis. The primary beam excavated ~4–6 ng of material, which resulted in an analysis pit depth of 5–6  $\mu\text{m}$ . The positive secondary ions generated were accelerated at 10 kV into the mass spectrometer, with the energy selection slit set to sample at >40 eV offset. The secondary ion arrival rates were measured by a single electron multiplier with a 25 ns collector deadtime in the ion counting system. The mass spectrometer was tuned to mass resolutions of 8500–9500 (10% peak height) to fully resolve any potential mass interferences. Isotopic data were collected in eight mass scans per analysis, scanning for six peaks during allanite analysis and for seven peaks during zircon analysis. Count times per scan ranged from 2 s to 90 s for each peak, and a typical duration for each analysis was about 35 min.

The primary  $O_2^-$  ion beam generates more secondary molecular ion species than their corresponding atomic ion species; thus, oxide ions yield better intensities (Reid et al., 1997). Allanite and zircon analyses measured intensities of  $^{232}Th^+$ ,  $^{230}Th^{16}O^+$  (~246 amu),  $^{232}Th^{16}O^+$  (~248 amu), and  $^{238}U^{16}O^+$  (~254 amu). Background intensity was measured at 0.05 amu above the mass of  $^{230}Th^{16}O^+$  to monitor tailing from the adjacent, more abundant  $^{232}Th^{16}O^+$  peak. The intensity of  $^{232}Th^{12}C^+$  (~244 amu) was measured to monitor the presence of carbon in the analyzed spot, because high  $^{232}Th^{12}C^+$  indicates carbon contamination, which forms a molecule ( $^{232}Th_2^{12}C^{16}O^+$ ) with an unresolvable mass interference on the  $^{230}Th^{16}O^+$  peak (Schmitt, 2011). Additionally, zircon analyses measured  $^{90}Zr_2^{16}O^+$  intensities to track Zr emission from zircon. All the raw count data collected were converted to isotope ratios after correcting for background and 25 ns collector deadtime using the SQUID2 software (Ludwig, 2008).

### ***Data treatment and correction***

After SIMS analysis, all zircon and allanite grains were imaged with a scanning electron microscope (SEM) to document grain shape and the position of the analysis spot on the crystal face (Fig. 9; Appendix 2). Several spot analyses with elevated  $^{232}Th^{12}C^+$  show evidence of beam overlap onto the indium mount (Fig. 9C); these data were discarded. A few high  $^{232}Th^{12}C^+$  allanite analyses show evidence of analysis on adhering glass instead of a crystal face (Fig. 9D) and were also discarded.

The measured isotopic ratios of Th and U were corrected to account for relative ionization because secondary ion yields differ between elements (Reid et al., 1997; Schmitt, 2011). Consequently, reference allanite and zircon standards were intermittently

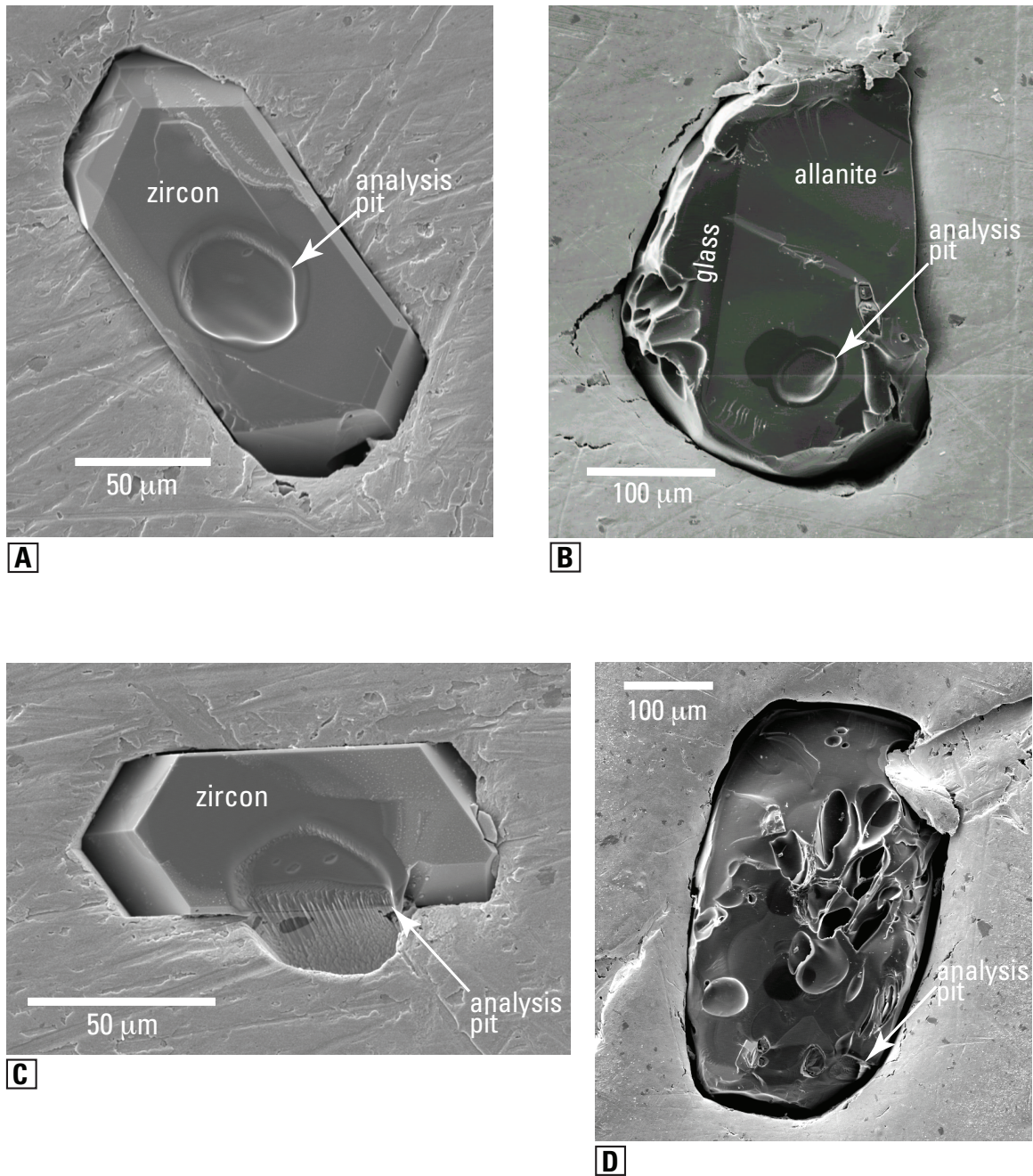


Figure 9. Backscattered electron images of analyzed unpolished zircon and allanite crystals embedded in indium metal. (A) Euhedral zircon and (B) allanite with “good” analysis spots well within grain boundaries. (C) Euhedral zircon showing a “bad” analysis spot, with evidence of beam overlap with indium mount. (D) Glass-encased (no exposed crystal face) allanite showing another “bad” analysis spot on the adhering vesicular glass. Zircon and allanite crystals are from dome 19 (sample 11JAVMC06).

analyzed along with the unknowns throughout each analytical session. Allanite standards include fragments from a Proterozoic pegmatitic allanite crystal from Arendal, Norway and from Pacoima Canyon, California, as well as allanite crystals from the ca. 770 ka Bishop Tuff. Zircon standards include Bishop Tuff zircon and a Neo-Proterozoic natural zircon standard (z6266). Analyzing  $(^{230}\text{Th})/(^{238}\text{U})$  for these ancient standards should yield the secular equilibrium value of 1, and a relative sensitivity factor (RSF) for each analytical session was determined by comparing the measured  $(^{230}\text{Th})/(^{238}\text{U})$  to the secular equilibrium value. Applying the RSF to the uncorrected U–Th isochron values for the standards yielded slopes that were within error of the equiline (Fig. 10). These session-specific RSF values and their uncertainties were propagated through the age calculation of the unknowns. Activity ratios of  $^{230}\text{Th}^{16}\text{O}^+ / ^{232}\text{Th}^{16}\text{O}^+$  and  $^{238}\text{U}^{16}\text{O}^+ / ^{232}\text{Th}^{16}\text{O}^+$  were derived by multiplying the measured molar ratios with their respective decay constants using  $9.1705 \times 10^{-6} \text{ a}^{-1}$  for  $^{230}\text{Th}$  (Cheng et al., 2013),  $4.9475 \times 10^{-11} \text{ a}^{-1}$  for  $^{232}\text{Th}$ , and  $1.55125 \times 10^{-10} \text{ a}^{-1}$  for  $^{238}\text{U}$  (Jaffey et al., 1971). U-series activity ratios for both allanite and zircon analyses were plotted on an isochron diagram, and isochron ages (Eq. 3) were obtained for each unknown sample using an error-weighted least-squares regression (Mahon, 1996) in Isoplot (Ludwig, 2008). Isochron ages are reported at the 95% confidence level along with the mean square of weighted deviates (MSWD), which is a statistical parameter used to assess the goodness of fit of the regression line (Wendt and Carl, 1991; Mahon, 1996). Individual data analyses were excluded if they produced  $\text{MSWD} > 2.0$  for a given isochron, thus eliminating only obvious outliers from the age calculation.

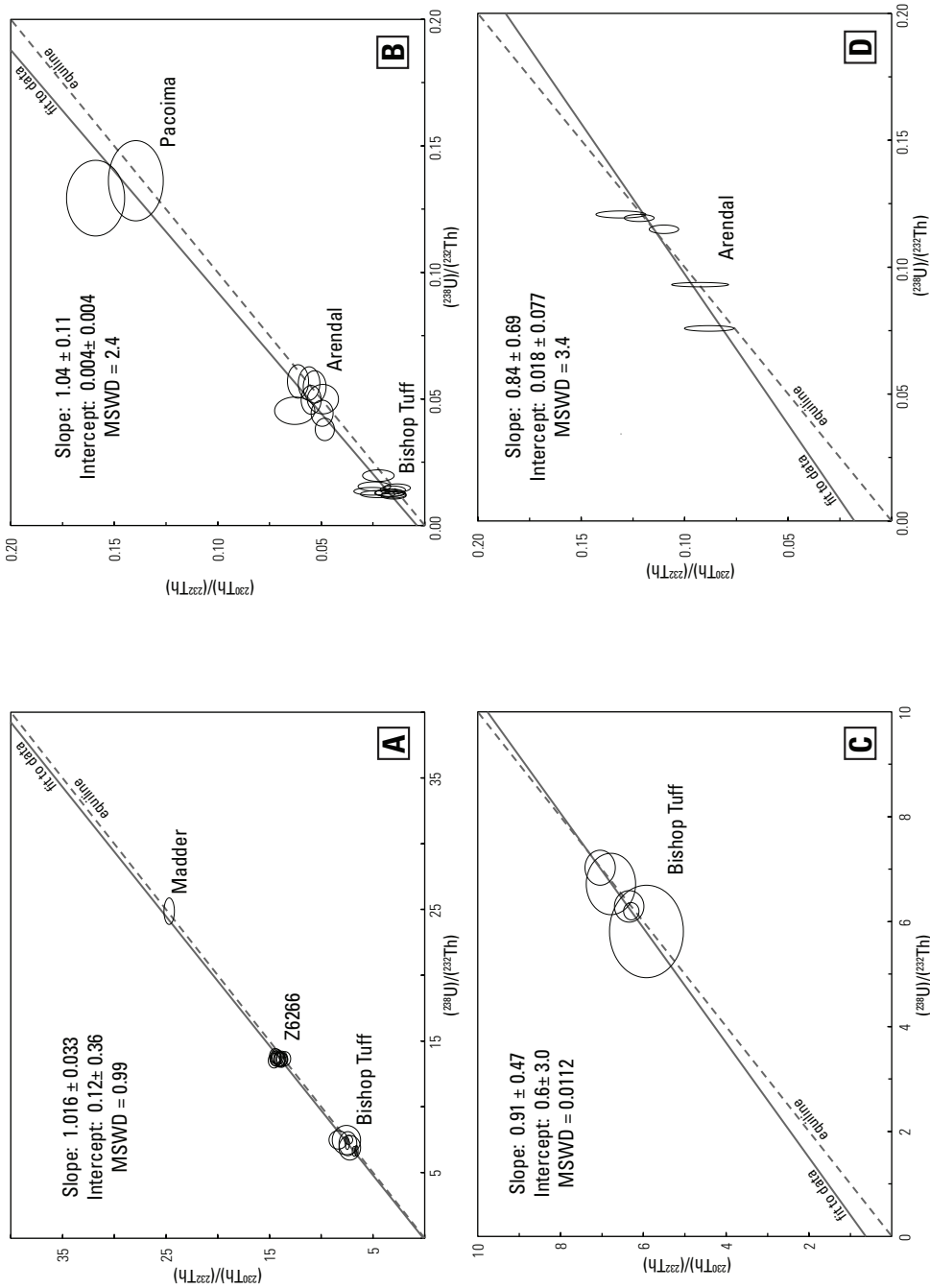


Figure 10. U–Th isochron diagrams of zircon and allanite standards. After correction, data for these ancient zircons and allanites plot within the  $2\sigma$  error of the equiline. (A) Zircon and (B) allanite standards for the April 2014 analytical session, during which the unknowns from dome 19 (sample 11JAVMC06) and dome 24 “lower lobe” (sample 11MCM05) were analyzed. (C) Zircon and (D) allanite standards for the March 2015 analytical session, during which the unknowns from dome 24 “upper lobe” (sample 14MCM12) were analyzed.

#### **$^{40}\text{Ar}/^{39}\text{Ar}$ analytical procedure: USGS $^{40}\text{Ar}/^{39}\text{Ar}$ Laboratory, Menlo Park, CA**

For irradiation, hand picked, clean sanidine separates for laser fusion technique were packaged in aluminum foil, whereas the 50–60 mg samples meant for incremental heating were packaged in copper foil. Each aluminum and copper foil packets (marked with a unique code number) were loaded and sealed in a quartz vial along with fluence monitors interspersed evenly among the unknown samples. To reduce neutron-induced production of interfering argon isotopes during irradiation, the quartz vial was wrapped in 0.5-mm-thick cadmium foil before irradiating for 60 minutes in the USGS TRIGA reactor in Denver, Colorado (Dalrymple et al., 1981). Continuous rotation and oscillation through the reactor centerline of the cadmium-lined quartz vial during irradiation minimize neutron flux gradients, which were determined from the co-irradiated fluence monitors and calculated by interpolation as  $J$  factors for each sample position. Reactor constants used for interference corrections were indistinguishable from recent irradiations:  $^{40}\text{Ar}/^{39}\text{Ar}_K = 0.00010 \pm 0.00038$ ,  $^{39}\text{Ar}/^{37}\text{Ar}_{Ca} = 0.00071 \pm 0.00005$ , and  $^{36}\text{Ar}/^{37}\text{Ar}_{Ca} = 0.000281 \pm 0.000006$ .

The Bodie Hills sanidine was used as fluence monitor with an age of 9.6345 Ma. This monitor is an internal USGS standard calibrated to secondary standard Taylor Creek sanidine ( $t = 27.87$  Ma), which is in turn calibrated against the K–Ar dated, primary intra-laboratory standard SB-3 biotite ( $t = 162.9$  Ma; Lanphere and Dalrymple, 2000). Using these standard ages, the more widely used sanidine monitor from Fish Canyon Tuff yields an age of 27.63 Ma. Irradiation parameters were calculated (Appendix 1, Eq. 1) from multiple analyses of the co-irradiated Bodie Hills sanidine (from each monitor position)

by single-crystal total fusion using a continuous laser system and a MAP 216 mass spectrometer at the USGS in Menlo Park, California, described in Dalrymple (1989).

Along with the sanidine fluence monitors, single irradiated sanidine grains from samples 11JAVMC06 and 14MCMM12 were loaded into individual wells on a copper planchette for argon analysis using the laser system, where a CO<sub>2</sub> laser was focused on each sanidine and heated until total fusion. For incremental heating, the irradiated copper foil packets were loaded into a high vacuum sample chamber and were dropped into a molybdenum-lined custom resistance furnace and heated in stepwise increments to a specified temperature for 10 min, from 650 °C to 1500 °C in 12 steps of 75 °C to 100 °C. In both laser fusion and incremental heating experiments, the extracted gas was isolated and purified in the argon extraction line for 5 min before the argon isotopes were measured in the mass spectrometer.

Raw count data (in unit volts) collected from 5 mass scans over the range of 40 to 36 amu were fitted with time zero regressions to obtain raw intercepts, which correspond to peak heights for measured isotopes <sup>40</sup>Ar, <sup>39</sup>Ar, <sup>38</sup>Ar, <sup>37</sup>Ar, and <sup>36</sup>Ar. Peak heights were corrected for background (or system blanks), which was measured before, during, and following each experiment, and mass discrimination, which was monitored by analyzing splits of atmospheric argon from a reservoir attached to the extraction line. Peak heights of <sup>39</sup>Ar and <sup>37</sup>Ar were corrected for decay ( $t_{1/2} = 269$  years and  $t_{1/2} = 35$  days, respectively) before interference corrections for all peaks using the reactor constants. The measured argon isotopes were then ratioed and apparent <sup>40</sup>Ar/<sup>39</sup>Ar ages for individual analyses were calculated (Appendix 1, Eq. 2) from the derived ratios of <sup>40</sup>Ar\*/<sup>39</sup>Ar<sub>K</sub> and the decay

constants recommended by Steiger and Jäger (1977). These apparent ages were calculated with the assumption that the initially trapped, non-radiogenic argon is atmospheric in composition ( $^{40}\text{Ar}/^{36}\text{Ar} = 295.5$ ; Nier, 1950). Uncertainties in apparent ages of individual analyses are reported at the 1- $\sigma$  level and include errors in  $J$ -values, isotope measurements, correction factors, and background.

### ***Data presentation***

$^{40}\text{Ar}/^{39}\text{Ar}$  data for laser fusion analyses are presented as age-probability density plots (ideograms) and isotope correlation diagrams and reported as error-weighted mean and isochron ages, respectively, at the 95% confidence level. Argon isotope data are plotted using the inverse isochron method and fit with a York (1969) linear least-squares regression, and the initial  $^{40}\text{Ar}/^{36}\text{Ar}$  ratio (95% confidence) is reported along with the isochron age. For incremental heating analyses, ages are reported as total gas, plateau, and isochron ages.  $^{40}\text{Ar}/^{39}\text{Ar}$  data are presented as age spectra, with apparent ages ( $\pm 1\sigma$ ) from individual temperature steps plotted against cumulative  $^{39}\text{Ar}$ -release. Total gas ages ( $\pm 2\sigma$ ) were calculated using the sum of individual isotopes across all steps to derive the total  $^{40}\text{Ar}^*/^{39}\text{Ar}_k$  ratio, analogous to a laser fusion age determination. Plateau ages (95% confidence) were calculated following the commonly accepted criteria of a well-defined plateau (horizontal age spectrum with no significant slope) from three contiguous steps that constitute at least 50% of  $^{39}\text{Ar}$  released (Fleck et al., 1977). The plateau gas fractions were plotted in an isotope correlation diagram to derive an isochron age, which is considered reliable if concordant with the plateau age, and if the isochron  $^{40}\text{Ar}/^{36}\text{Ar}$  intercept is indistinguishable from the atmospheric ratio.

## RESULTS

### Titanomagnetite chemistry

The chemistry of titanomagnetites from dome 24 “upper lobe” (sample 14MCMM12) is presented in Figure 11, and complete analytical data are found in Appendix 3. Most titanomagnetites are compositionally homogeneous, and the few crystals displaying exsolution patterns were not analyzed. Average compositions for 37 titanomagnetites were ~12.5 wt% TiO<sub>2</sub> and ~85 wt% FeO, with minor components Al<sub>2</sub>O<sub>3</sub>+MgO+MnO comprising <2.5 wt%. These new titanomagnetite data were compared with published values for domes 11, 19, and 24 (“lower lobe”) of the Mono Craters (Marcaida et al., 2014). The “upper lobe” of dome 24 (sample 14MCMM12) has titanomagnetites that are compositionally distinct from titanomagnetites of the other Mono Craters domes. In particular, there is no overlap between titanomagnetites from the “lower lobe” (sample 11MCMM05) and the “upper lobe” (sample 14MCMM12) of dome 24 (Fig. 11A), and this “upper lobe” is hereafter treated as a distinct dome. Because the “dome 24” designation in published literature refers to the lower lobe of lava (e.g., Wood, 1983; Bursik and Sieh, 1989; Kelleher and Cameron, 1990; Marcaida et al., 2014), the “upper lobe” of dome 24 is provisionally named dome 31 (after Wood, 1983), pending confirmation from geochronological work.

Comparison with titanomagnetites from the Mono Craters-sourced Wilson Creek formation tephra layers (Marcaida et al., 2014) shows closely matching compositions between Ash 7 titanomagnetite and dome 31 titanomagnetite (Fig. 12B), which potentially correlates Ash 7 to the newly recognized dome 31 of the Mono Craters.

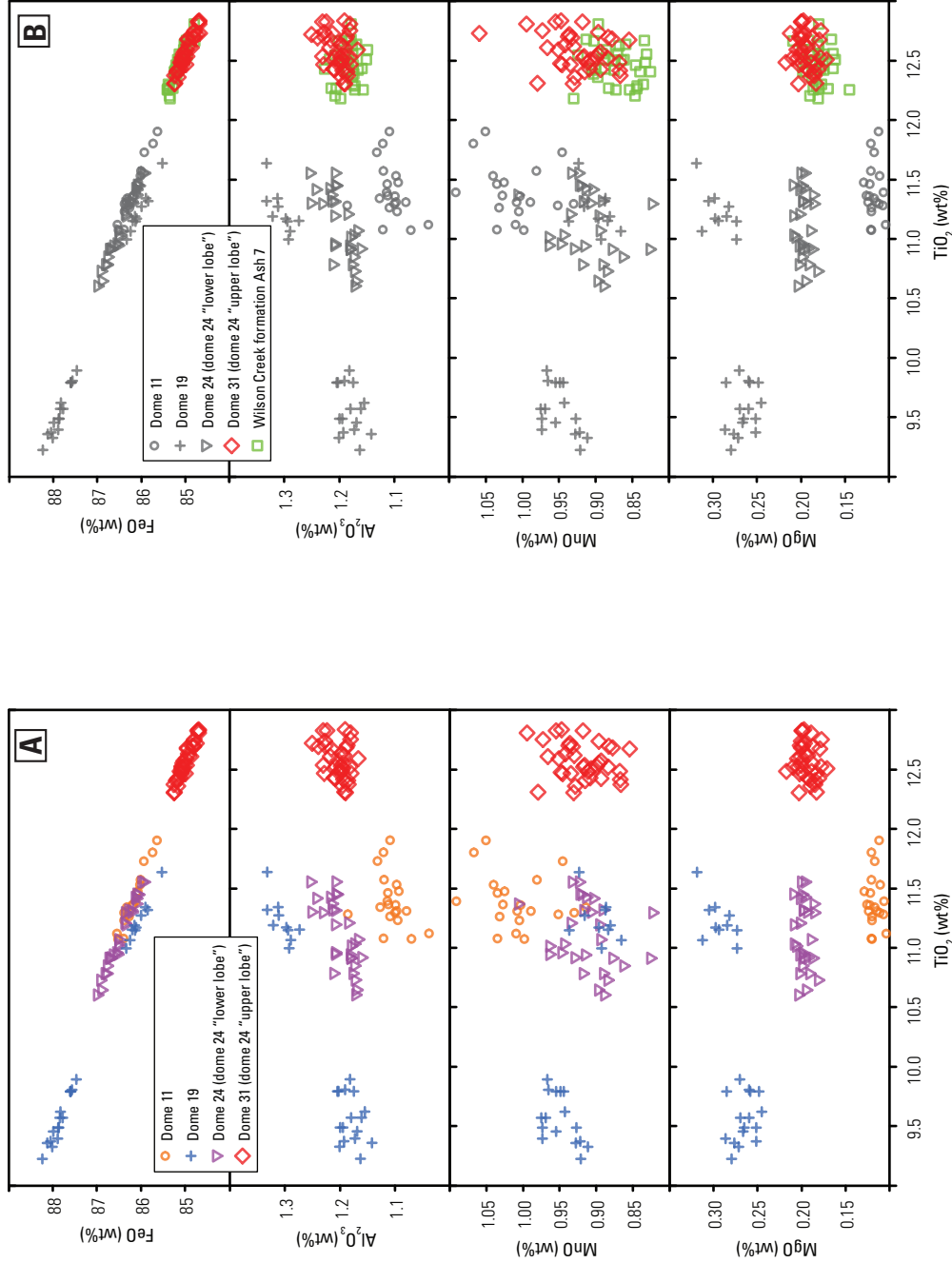


Figure 11. (A) Titanomagnetite data for domes 11, 19 (sample 11JAVMC06), and 24 (“lower lobe”; sample 11MCM05) from Marcaida et al. (2014). Titanomagnetites from the “upper lobe” and “lower lobe” of dome 24 are distinct. Dome 24 “upper lobe” (sample 14MCM12) is hereafter referred to as dome 31. (B) Titanomagnetites from dome 31 have compositions that closely match those of Wilson Creek formation Ash 7 titanomagnetites (data from Marcaida et al., 2014).

## **$^{238}\text{U}$ – $^{230}\text{Th}$ geochronology**

$^{238}\text{U}$ – $^{230}\text{Th}$  compositions and activity ratios of coexisting allanite and zircon from select domes of the Mono Craters are summarized in Table 1. All analyzed zircons are euhedral, whereas allanite grains are subhedral to euhedral and typically have glass adhering to crystal edges (Figs. 9A and 9B; Appendix 2). Analyses of unpolished allanite and zircon rims yield U–Th activity ratios that are in radioactive disequilibrium. On the  $(^{230}\text{Th})/(^{232}\text{Th})$  versus  $(^{238}\text{U})/(^{232}\text{Th})$  diagram, zircon analyses display excess  $^{238}\text{U}$  and plot to the right of the equiline, whereas allanite analyses show  $^{238}\text{U}$  deficiencies and plot to the left of the equiline. Rims on coexisting allanite and zircon yield a well-defined isochron for each of the studied domes, the slope of which gives high-precision (2–5%) late Pleistocene crystallization ages for Mono Craters domes 19, 24, and 31. Dome 19 has a  $^{238}\text{U}$ – $^{230}\text{Th}$  isochron age of  $42.5 \pm 1.1$  ka, with a MSWD of 1.5 from 51 rim analyses of 50 individual zircon and allanite crystals (Fig. 12). Dome 24 zircon and allanite rims have a  $^{238}\text{U}$ – $^{230}\text{Th}$  isochron age of  $38.0 \pm 1.2$  ka (MSWD 2.0,  $n = 40$ ; Fig. 13). Dome 31 has the youngest zircon-allanite population in this study with rims yielding a  $^{238}\text{U}$ – $^{230}\text{Th}$  isochron age of  $26.2 \pm 1.2$  ka (MSWD 2.0,  $n = 36$ ; Fig. 14).

Reported isochron ages for domes 19 and 24 exclude a minority of allanite and zircon with apparently older and/or younger rims, although the isochron ages would only differ by several hundred years if all analyses were included in the age calculation (Figs. 12 and 13, red ellipses). Dome 31 excludes two zircon analyses with older apparent rim ages (Fig. 14, red ellipses), and the reported isochron age is younger by ca. 2 ka with the exclusion of the two outliers.

Table 1.  $^{238}\text{U}/^{230}\text{Th}$  composition of zircon and allanite rims.

Sample	$(^{238}\text{U})/(^{232}\text{Th})$	$\pm (1\sigma)$	$(^{230}\text{Th})/(^{232}\text{Th})$	$\pm (1\sigma)$
<b>Dome 19, sample 11JAVMC06, 37.8703°N 119.0166°W</b>				
<i>zircon</i>				
DOME19-1	9.40	0.20	3.364	0.103
DOME19-2	7.53	0.14	3.082	0.105
DOME19-3	6.14	0.18	2.556	0.083
DOME19-4	9.06	0.27	3.608	0.125
DOME19-5	9.43	0.30	3.539	0.127
DOME19-6	5.91	0.35	2.575	0.126
DOME19-7	8.20	0.20	3.101	0.116
DOME19-8	8.41	0.23	3.464	0.091
DOME19-10	5.91	0.12	2.506	0.099
DOME19-11	7.29	0.21	2.852	0.080
DOME19-13	7.25	0.21	2.923	0.148
DOME19-14	7.86	0.14	2.980	0.098
DOME19-16	8.25	0.14	3.278	0.118
DOME19-17	7.80	0.17	2.808	0.094
DOME19-19	8.09	0.21	3.060	0.095
DOME19-21	7.42	0.16	3.113	0.089
DOME19-25	7.29	0.18	3.195	0.104
DOME19-27	5.15	0.29	2.246	0.064
DOME19-28	8.53	0.16	3.368	0.100
DOME19-29	7.70	0.27	3.191	0.107
DOME19-30	7.38	0.18	3.069	0.148
DOME19-31	3.87	0.06	1.958	0.053
<b>DOME19-32</b>	<b>8.91</b>	<b>0.31</b>	<b>3.980</b>	<b>0.086</b>
DOME19-33	7.97	0.15	3.080	0.078
DOME19-34	6.75	0.11	2.924	0.080
DOME19-35	8.63	0.16	3.351	0.075
DOME19-36	6.81	0.31	2.696	0.096
DOME19-37	6.65	0.17	2.694	0.077
DOME19-38	6.68	0.12	2.752	0.070
DOME19-39	7.95	0.19	3.248	0.106
DOME19-40	8.93	0.16	3.536	0.099
<i>allanite</i>				
DOME19-1.1	0.01979	0.00094	0.595	0.013
DOME19-2.1	0.01865	0.00088	0.575	0.014
DOME19-3.3	0.01470	0.00070	0.612	0.012
DOME19-4.1	0.01747	0.00083	0.579	0.011
DOME19-4.2	0.01478	0.00070	0.566	0.021
DOME19-8.1	0.01675	0.00091	0.612	0.016
<b>DOME19-11.1</b>	<b>0.01685</b>	<b>0.00080</b>	<b>0.533</b>	<b>0.015</b>
DOME19-12.1	0.02028	0.00096	0.573	0.013
DOME19-13.1	0.01488	0.00071	0.598	0.015
DOME19-14.1	0.01764	0.00083	0.615	0.013
DOME19-15.1	0.01723	0.00081	0.613	0.015
DOME19-16.1	0.01690	0.00080	0.589	0.015
DOME19-17.1	0.01573	0.00075	0.569	0.015
DOME19-19.1	0.01710	0.00091	0.634	0.014
DOME19-20.1	0.02078	0.00099	0.596	0.013
DOME19-21.1	0.01851	0.00088	0.612	0.014
DOME19-22.1	0.01826	0.00087	0.604	0.015
DOME19-23.1	0.02113	0.00100	0.596	0.023
DOME19-24.1	0.01619	0.00077	0.579	0.013
DOME19-25.1	0.02121	0.00100	0.589	0.013
DOME19-26.1	0.01764	0.00089	0.639	0.020
DOME19-27.1	0.01584	0.00075	0.616	0.015

Table 1 (*continued*)

Sample	$(^{238}\text{U})/(^{232}\text{Th})$	$\pm (1\sigma)$	$(^{230}\text{Th})/(^{232}\text{Th})$	$\pm (1\sigma)$
<b>Dome 24, sample 11MCM05, 37.8347°N 118.9996°W</b>				
<i>zircon</i>				
DOME24-1	8.92	0.21	3.13	0.13
DOME24-2	5.08	0.27	2.06	0.05
DOME24-3	8.29	0.29	3.05	0.07
DOME24-4	5.99	0.11	2.40	0.05
DOME24-5	7.74	0.13	3.22	0.11
DOME24-6	8.77	0.17	3.10	0.09
DOME24-7	8.35	0.16	3.14	0.08
DOME24-8	8.44	0.25	3.75	0.10
DOME24-9	8.34	0.24	3.16	0.09
DOME24-10	7.85	0.43	2.99	0.15
DOME24-13	11.23	0.29	3.92	0.12
DOME24-14	8.87	0.28	3.13	0.13
DOME24-15	9.32	0.22	3.24	0.11
DOME24-17	6.96	0.12	2.71	0.07
DOME24-18	8.31	0.16	2.90	0.08
DOME24-19	10.19	0.29	3.33	0.10
DOME24-20	8.44	0.36	3.02	0.15
DOME24-21	8.98	0.33	3.57	0.11
DOME24-22	7.86	0.17	2.89	0.19
DOME24-24	8.09	0.14	2.90	0.07
DOME24-25	7.84	0.16	2.77	0.06
DOME24-26	7.98	0.16	2.58	0.06
DOME24-29	8.08	0.19	3.08	0.13
DOME24-30	7.81	0.19	2.78	0.08
DOME24-31	7.54	0.13	3.01	0.07
<i>allanite</i>				
DOME_24-1.1	0.01608	0.00078	0.578	0.014
DOME_24-2.1	0.01678	0.00080	0.625	0.014
DOME_24-3.1	0.01824	0.00087	0.606	0.014
DOME_24-4.1	0.01693	0.00080	0.623	0.012
DOME_24-5.1	0.10314	0.02405	0.631	0.024
DOME_24-6.1	0.01932	0.00091	0.585	0.013
DOME_24-8.1	0.01600	0.00076	0.608	0.013
DOME_24-12.1	0.02021	0.00096	0.631	0.012
DOME_24-13.1	0.01753	0.00084	0.607	0.013
DOME_24-15.1	0.01743	0.00082	0.636	0.012
DOME_24-16.1	0.01743	0.00082	0.633	0.014
DOME_24-17.1	0.01896	0.00090	0.556	0.010
DOME_24-18.1	0.02000	0.00095	0.649	0.021
DOME_24-19.1	0.01638	0.00078	0.672	0.021
DOME_24-20.1	0.01864	0.00088	0.572	0.013
DOME_24-21.1	0.01845	0.00087	0.621	0.014
DOME_24-22.1	0.01795	0.00086	0.604	0.013
DOME_24-23.1	0.01848	0.00087	0.600	0.013
DOME_24-24.1	0.01964	0.00093	0.579	0.014

Table 1 (*continued*)

Sample	$(^{238}\text{U})/(^{232}\text{Th})$	$\pm (1\sigma)$	$(^{230}\text{Th})/(^{232}\text{Th})$	$\pm (1\sigma)$
<b>Dome 31, sample 14MCM12, 37.8375°N 118.9977°W</b>				
<i>zircon</i>				
MM12-1.1	5.80	0.06	1.86	0.07
MM12-2.1	8.40	0.40	2.91	0.27
MM12-3.1	8.85	0.09	2.52	0.13
MM12-4.1	6.40	0.16	2.02	0.14
MM12-5.1	8.00	0.26	2.25	0.18
MM12-6.1	10.18	0.24	2.74	0.15
MM12-7.1	8.51	0.21	2.26	0.10
MM12-8.1	7.87	0.17	2.37	0.08
MM12-9.1	11.65	0.47	3.60	0.29
MM12-10.1	10.01	0.15	2.76	0.14
MM12-11.1	8.45	0.39	2.44	0.21
MM12-12.1	8.89	0.10	2.45	0.16
MM12-13.1	7.54	0.27	2.15	0.08
MM12-14.1	9.68	0.12	2.26	0.14
MM12-15.1	8.00	0.17	2.10	0.08
MM12-16.1	9.23	0.18	2.69	0.10
MM12-17.1	8.75	0.20	3.13	0.18
MM12-18.1	8.38	0.13	2.41	0.10
MM12-19.1	8.84	0.10	2.44	0.16
MM12-20.1	9.50	0.26	2.89	0.17
MM12-21.1	10.23	0.17	2.89	0.12
MM12-22.1	5.24	0.19	2.22	0.06
MM12-23.1	5.56	0.15	1.85	0.07
MM12-24.1	6.77	0.17	2.06	0.08
MM12-25.1	6.52	0.12	3.97	0.11
MM12-26.1	9.51	0.09	2.49	0.11
MM12al-4.1	5.12	0.11	1.84	0.06
<i>allanite</i>				
MM12al-1.1	0.03304	0.00022	0.623	0.014
MM12al-2.1	0.04221	0.00027	0.655	0.014
MM12al-3.1	0.04033	0.00023	0.613	0.020
MM12al-5.1	0.03281	0.00020	0.617	0.015
MM12al-6.1	0.04352	0.00031	0.588	0.016
MM12al-7.1	0.03985	0.00019	0.609	0.012
MM12al-8.1	0.04237	0.00026	0.646	0.012
MM12al-9.1	0.03991	0.00032	0.627	0.012
MM12al-10.1	0.05036	0.00161	0.643	0.018
MM12al-11.1	0.04033	0.00047	0.679	0.025
MM12al-12.1	0.04239	0.00093	0.614	0.014

Activity ratios were calculated from measured atomic ratios and decay constants for  $^{230}\text{Th}$  ( $9.1705 \times 10^{-6} \text{ a}^{-1}$ ; Cheng et al., 2013),  $^{232}\text{Th}$  ( $4.94752 \times 10^{-11} \text{ a}^{-1}$ ), and  $^{238}\text{U}$  ( $1.55125 \times 10^{-10} \text{ a}^{-1}$ ). Isotopic ratios in red are not included in the isochron age calculation.

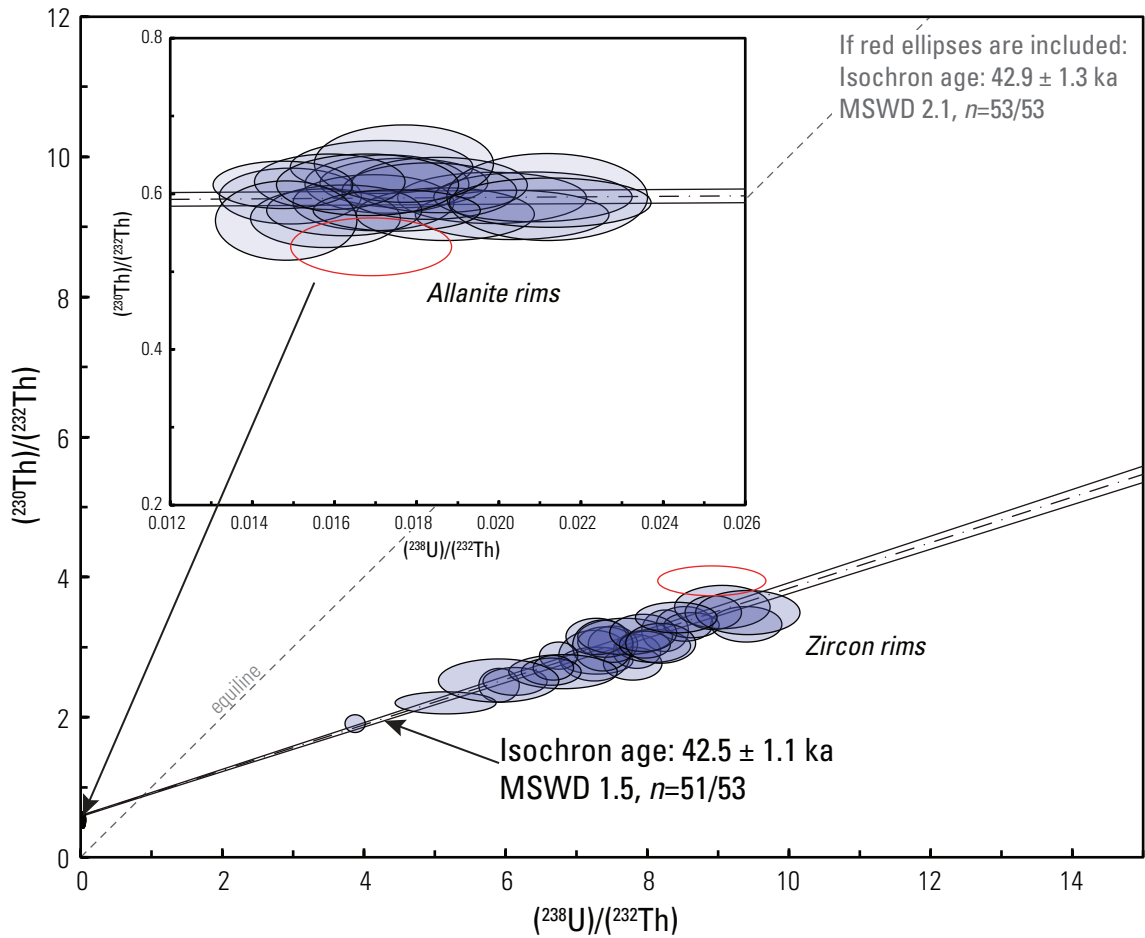


Figure 12.  $^{238}\text{U}$ - $^{230}\text{Th}$  isochron diagram for allanite (inset) and zircon rims from dome 19 of the Mono Craters (sample 11JAVMC06). The isochron is shown with a  $1\text{-}\sigma$  error envelope, and the isochron age is reported at the 95% confidence level. Each ellipse represents a distinct crystal with  $2\text{-}\sigma$  analytical uncertainties; red ellipses are excluded from the isochron age calculation. MSWD: mean square of weighted deviates;  $n$  is the number of analyses.

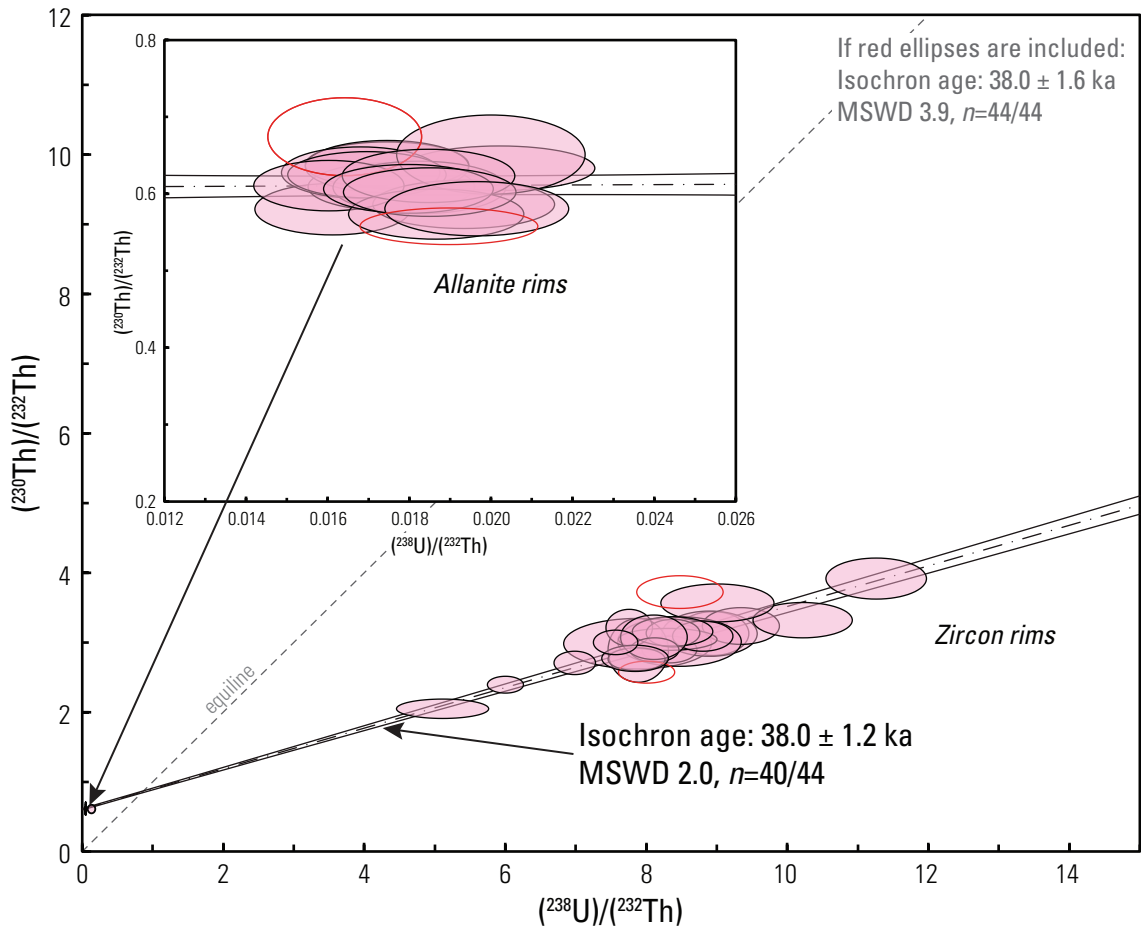


Figure 13.  $^{238}\text{U}$ – $^{230}\text{Th}$  isochron diagram for allanite (inset) and zircon rims from dome 24 of the Mono Craters (sample 11MCMM05). The isochron is shown with a 1- $\sigma$  error envelope, and the isochron age is reported at the 95% confidence level. Each ellipse represents a distinct crystal with 2- $\sigma$  analytical uncertainties; red ellipses are excluded from the isochron age calculation. MSWD: mean square of weighted deviates;  $n$  is the number of analyses.

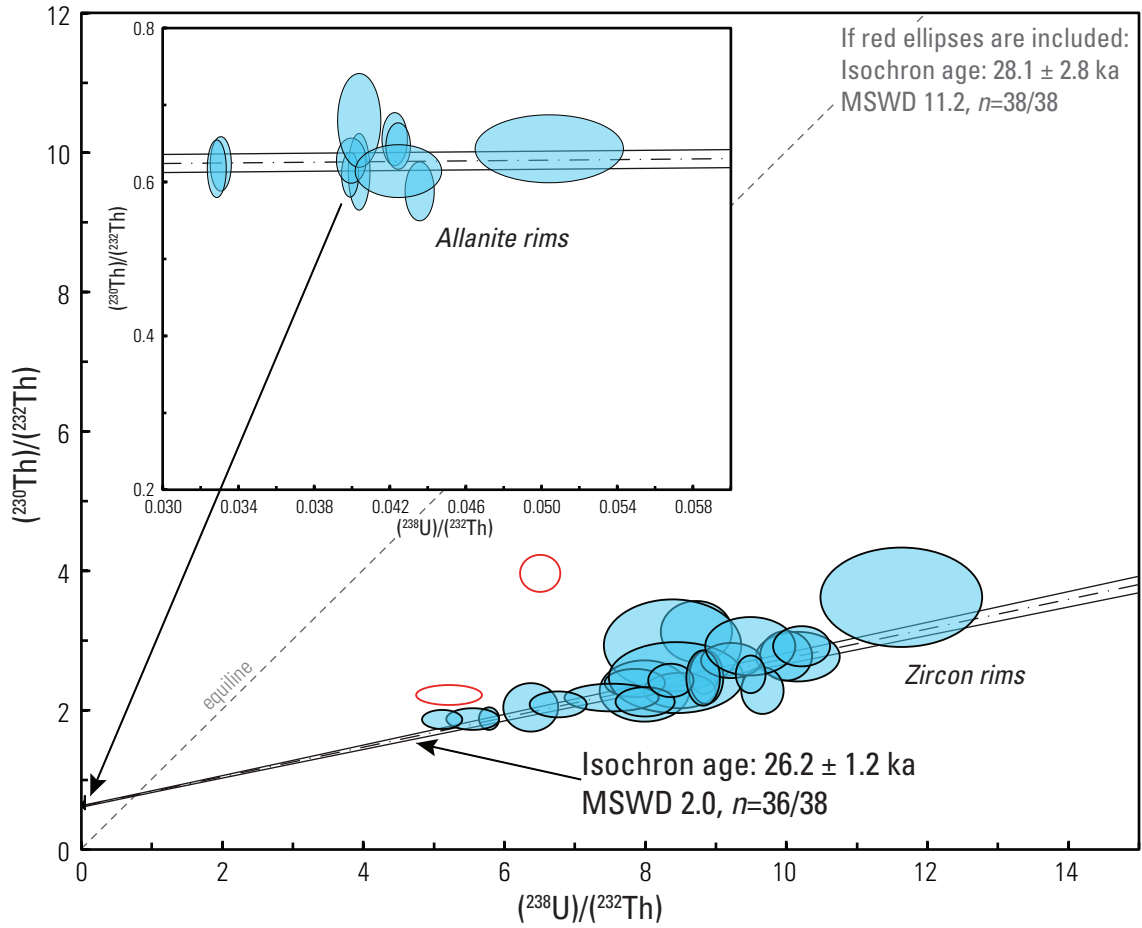


Figure 14.  $^{238}\text{U}$ – $^{230}\text{Th}$  isochron diagram for allanite (inset) and zircon rims from dome 31 of the Mono Craters (sample 14MCMM12). The isochron is shown with a 1- $\sigma$  error envelope, and the isochron age is reported at the 95% confidence level. Each ellipse represents a distinct crystal with 2- $\sigma$  analytical uncertainties; red ellipses are excluded from the isochron age calculation. MSWD: mean square of weighted deviates;  $n$  is the number of analyses.

## **$^{40}\text{Ar}/^{39}\text{Ar}$ geochronology**

### ***Laser total-fusion analyses***

$^{40}\text{Ar}/^{39}\text{Ar}$  sanidine age data are summarized in Table 2. All data are shown in complete detail in Appendix 4. For a given sample, K/Ca ratios (a function of K-content from measurements of  $^{39}\text{Ar}$  and  $^{37}\text{Ar}$ ) and radiogenic yield (%  $^{40}\text{Ar}^*$ ; the percent of measured  $^{40}\text{Ar}$  that cannot be attributed to atmospheric argon) were used to evaluate the apparent ages of individual analyses, wherein analyses with low K/Ca ratios for sanidine (<20) and/or radiogenic yield with anomalously low values (<0) were excluded from the data set (Appendix 4). Error-weighted mean and isochron ages for each analyzed dome sample were then calculated from the edited data set. Single-crystal laser analyses of 36 individual sanidine grains from dome 19 (sample 11JAVMC06) yielded a mean age of  $59.4 \pm 7.6$  ka (MSWD 1.08) and an isochron age of  $54 \pm 11$  ka (MSWD 1.04) with a  $^{40}\text{Ar}/^{36}\text{Ar}$  ( $299.8 \pm 5.6$ ) intercept within error of the atmosphere (Fig. 15A). Analyses of 27 sanidine crystals from dome 31 (sample 14MCMM12) yielded analytically equivalent weighted mean and isochron ages of  $33.8 \pm 9.3$  ka (MSWD 0.64) and  $32 \pm 15$  ka (MSWD 0.65), respectively, with a  $^{40}\text{Ar}/^{36}\text{Ar}$  intercept of  $296.4 \pm 3.8$  (Fig. 16).

The percentage content of  $^{40}\text{Ar}^*$  ranges from 0 to 12% for sample 14MCMM12 (dome 31), and 0 to 26% for sample 11JAVMC06 (dome 19). Given the overall low values of radiogenic yield, the spread along the isochron is very limited (Figs. 15 and 16), and uncertainties regarding the isochron ages are around 20–47% (at the 95% confidence level) for both samples. To increase precision, additional laser analyses were conducted for sample 11JAVMC06 (dome 19) wherein multi-grain aliquots of sanidine (5 grains)

Table 2. Summary of sanidine  $^{40}\text{Ar}/^{39}\text{Ar}$  age data.

Method	Age (ka)	MSWD	Initial $^{40}\text{Ar}/^{36}\text{Ar}$
<b>Dome 19, sample 11JAVMC06</b>			
Laser total-fusion			
<i>Single-crystal (n = 36/38)</i>			
Wtd. mean	59.4 ± 7.6	1.08	-
Isochron	54 ± 11	0.93	299.8 ± 5.6
<i>Multi-grain (n = 41/45)</i>			
Wtd. mean	49.9 ± 2.3	1.6	-
Isochron	37 ± 15	1.4	329 ± 32
<i>Combined (n = 77/83)</i>			
Wtd. mean	50.4 ± 2.1	1.4	-
Isochron	47.3 ± 3.1	1.3	302.8 ± 5.4
Furnace incremental-heating			
Total gas	48.0 ± 1.8 (2σ)	-	-
*Plateau	50.9 ± 2.7	2.6	-
*Isochron	54 ± 11	0.93	299.8 ± 5.6
<b>Dome 31, sample 14MCM12</b>			
Single-crystal laser total-fusion (n = 27/30)			
Wtd. mean	33.8 ± 9.3	0.64	-
Isochron	32 ± 15	0.65	296.4 ± 3.8
Furnace incremental-heating			
Total gas	27.5 ± 1.6 (2σ)	-	-
Plateau		no plateau	
Isochron	36.6 ± 3.8	3.5	283.4 ± 6.9

All ages calculated relative to 9.6345 Bodie Hills sanidine and decay constants of Steiger and Jäger (1977). All uncertainties are given at the 95% confidence level, except where indicated.

$n$  is the number of experiments used to calculate the age versus the total number of experiments.

MSWD: mean square of weighted deviates; where no initial  $^{40}\text{Ar}/^{36}\text{Ar}$  is reported, initial Ar composition is assumed to be atmospheric (295.5).

\*Plateau and isochron ages calculated from 4 out of 12 temperature steps.

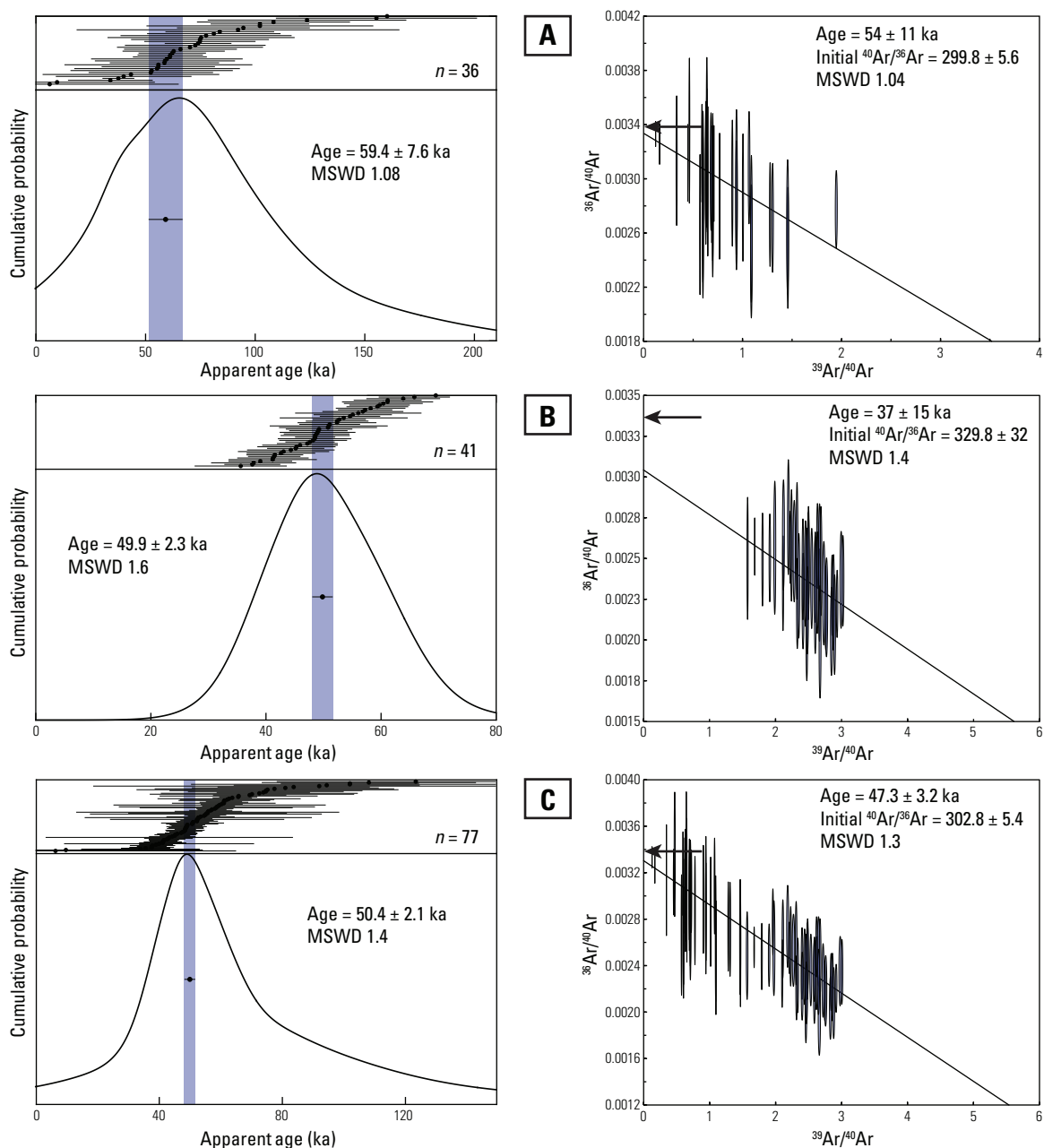


Figure 15. Age-probability (ideograms; left) and isochron plots (right) of  $^{40}\text{Ar}/^{39}\text{Ar}$  laser fusion data of dome 19 sanidine (sample 11JAVMC06). Ideograms: black dot is a single analysis with  $1\sigma$  error bars; weighted mean ages are at the 95% confidence level and indicated by a 2- $\sigma$  vertical blue band. Isochron plots: error ellipse is 2 $\sigma$  and is a single analysis; isochron ages and initial  $^{40}\text{Ar}/^{36}\text{Ar}$  ratios are at the 95% confidence level; black arrow indicates  $^{40}\text{Ar}/^{36}\text{Ar}$  atmospheric composition. Ideograms and isochron plots for (A) single-grain sanidine laser analysis, (B) multi-grain sanidine laser analysis, and (C) combined data set from (A) and (B). Complete  $^{40}\text{Ar}/^{39}\text{Ar}$  data is in Appendix 4. MSWD: mean square of weighted deviates;  $n$  is the number of analysis.

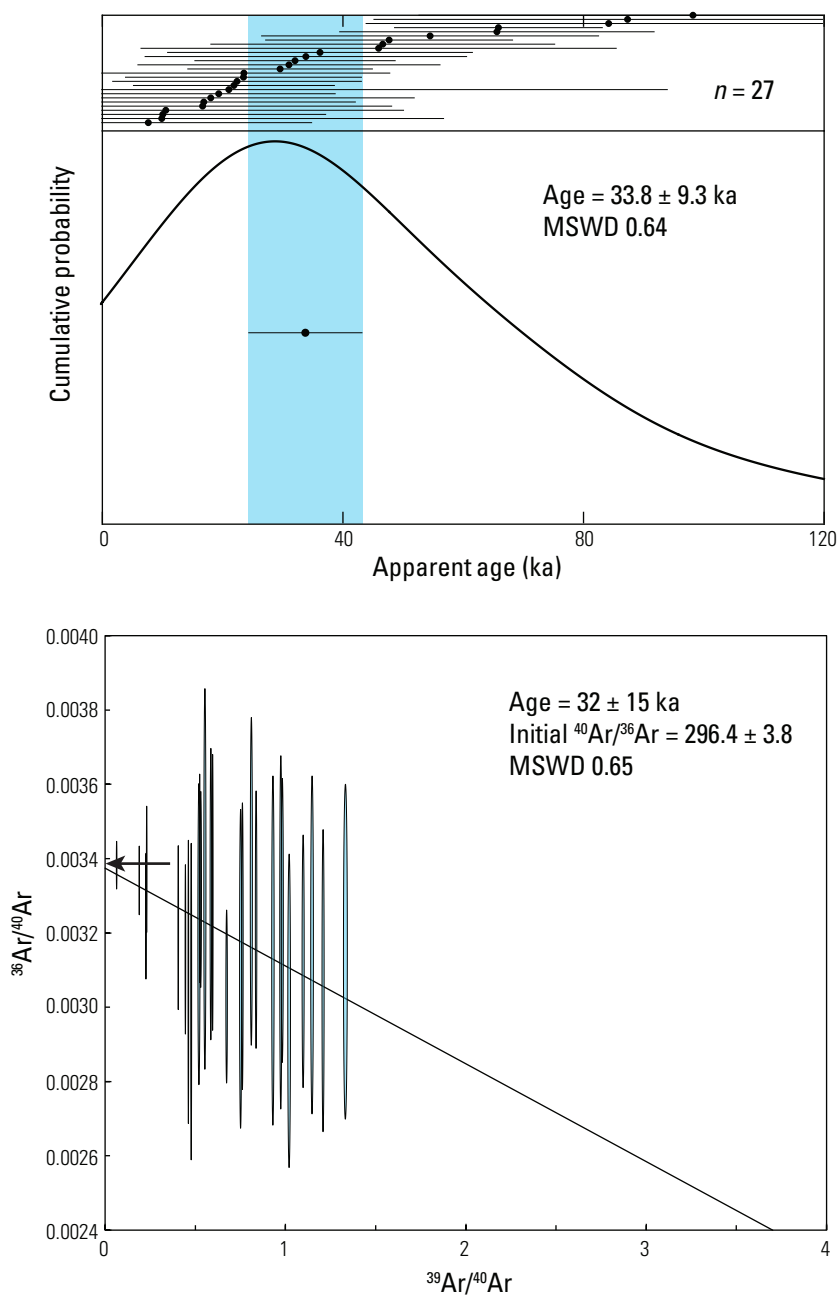


Figure 16. Ideogram (top) and isochron plot (bottom) of  $^{40}\text{Ar}/^{39}\text{Ar}$  laser fusion data of dome 31 sanidine (sample 14MCMM12). Ideogram: black dot is a single analysis with  $1\sigma$  error bars; weighted mean age is at the 95% confidence level and indicated by a  $2\text{-}\sigma$  vertical blue band. Isochron plot: error ellipse is  $2\sigma$  and is a single analysis; isochron age and initial  $^{40}\text{Ar}/^{36}\text{Ar}$  ratio are at the 95% confidence level; black arrow indicates  $^{40}\text{Ar}/^{36}\text{Ar}$  atmospheric composition. Complete  $^{40}\text{Ar}/^{39}\text{Ar}$  data is in Appendix 4. MSWD: mean square of weighted deviates;  $n$  is the number of analysis.

were fused as a set. The new experiments yielded higher percentage of  $^{40}\text{Ar}^*$  (19–41%; Fig. 15B), and thus more precise apparent ages compared to the earlier single-grain analyses. The weighted mean age of sanidines from dome 19 is calculated to about 5% precision ( $49.9 \pm 2.3$  ka, MSWD 1.6,  $n = 41$ ), although the uncertainty with the isochron age remained at about  $\pm 40\%$  ( $37 \pm 15$  ka, MSWD 1.4,  $^{40}\text{Ar}/^{36}\text{Ar} = 329 \pm 32$ ) because there was too little spread in the isotopic data (Fig. 15B). Combining both single-grain and multi-grain laser analyses yielded weighted mean and isochron ages with about 4–7% precision (Fig. 15C). From the combined data set, the error-weighted mean age of sanidine from dome 19 is  $50.4 \pm 2.1$  ka (MSWD 1.4), and the isochron age is  $47.3 \pm 3.2$  ka (MSWD 1.3), with a  $^{40}\text{Ar}/^{36}\text{Ar}$  intercept ( $302.8 \pm 5.4$ ) slightly higher than the atmospheric composition.

### ***Furnace incremental-heating analyses***

The results of incremental-heating experiments on sanidine for dome 19 (sample 11JAVMC06) and dome 31 (sample 14MCMM12) are presented in Figures 17 and 18. Age determinations are summarized in Table 2, and the complete analytical data are in Appendix 5. Sanidine from dome 19 yielded a weighted-mean plateau age of  $52.4 \pm 1.6$  ka (MSWD 0.63) from the four highest temperature steps comprising 50% of  $^{39}\text{Ar}$  released (Fig. 17). The plateau-steps yielded a concordant isochron age of  $50.8 \pm 3.3$  ka (MSWD 0.24) and an initial  $^{40}\text{Ar}/^{36}\text{Ar}$  ratio ( $303 \pm 12$ ) with a rather large uncertainty, although within error of the atmosphere (Fig. 17). An apparent isochron age of  $51.9 \pm 3.8$  (MSWD 3.5) was derived from all the argon isotope data (both plateau and non-plateau steps) that is indistinguishable from the total gas age of  $48.0 \pm 1.8$  ka ( $2\sigma$ ).

Apparent ages from all temperature steps for dome 31 were variable and did not yield a plateau (Fig. 18). The total gas age is  $27.5 \pm 1.6$  ka ( $2\sigma$ ), whereas the apparent isochron age obtained from all the isotope data is  $36.6 \pm 3.8$  ka (MSWD 3.5) with an initial  $^{40}\text{Ar}/^{36}\text{Ar}$  ratio ( $283.4 \pm 6.9$ ) that is lower than the atmospheric ratio (Fig. 18).

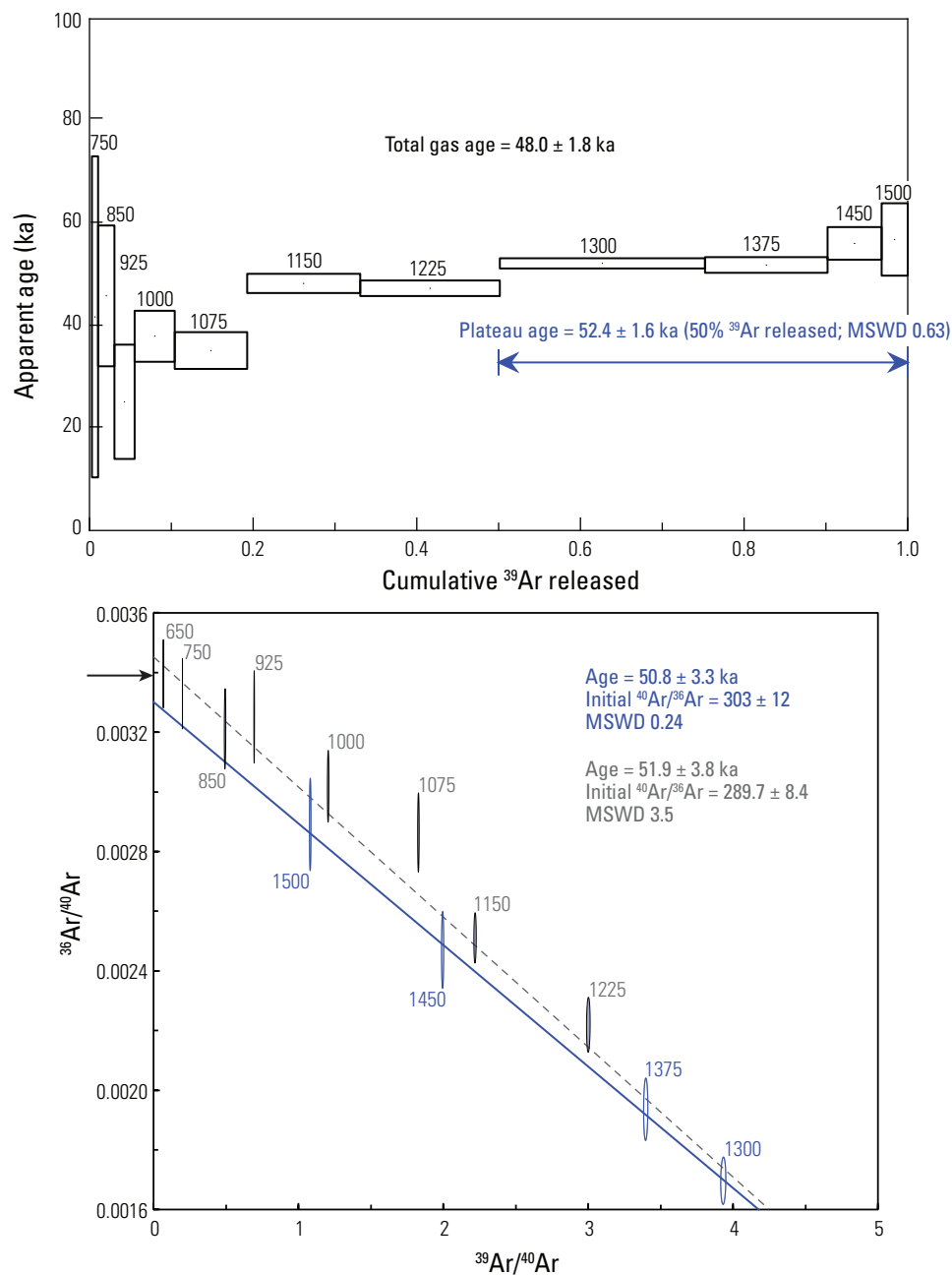


Figure 17. <sup>40</sup>Ar/<sup>39</sup>Ar age spectrum (top) and inverse isochron (bottom) for dome 19 sanidine (sample 11JACMC06). Apparent age box heights are 1 $\sigma$ ; isotopic ratio ellipses are 2 $\sigma$ . Weighted mean plateau age, isochron age, and initial <sup>40</sup>Ar/<sup>36</sup>Ar ratio are at the 95% confidence level; total gas age at 2 $\sigma$ . On the age spectrum, the blue line with arrows indicates the temperature steps (in  $^{\circ}$ C) used in the calculated plateau age, with the corresponding isochron fit and age for the particular steps shown in the isochron plot (blue line and font). The dashed line is the fit to all the isotope data in the isochron plot, from which an age is derived. Black arrow indicates the <sup>40</sup>Ar/<sup>36</sup>Ar atmospheric composition. Complete <sup>40</sup>Ar/<sup>39</sup>Ar data is in Appendix 5. MSWD: mean square of weighted deviates.

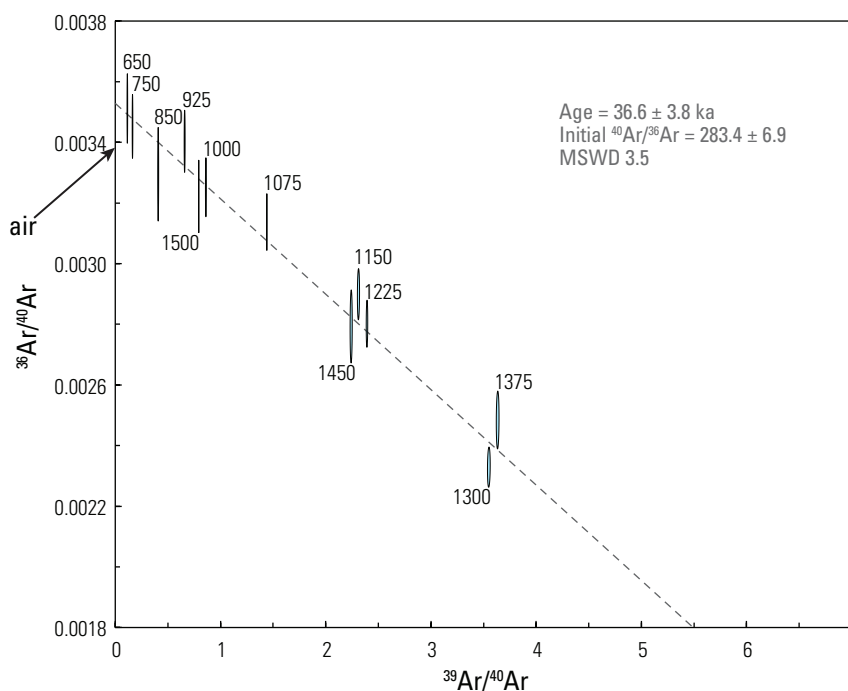
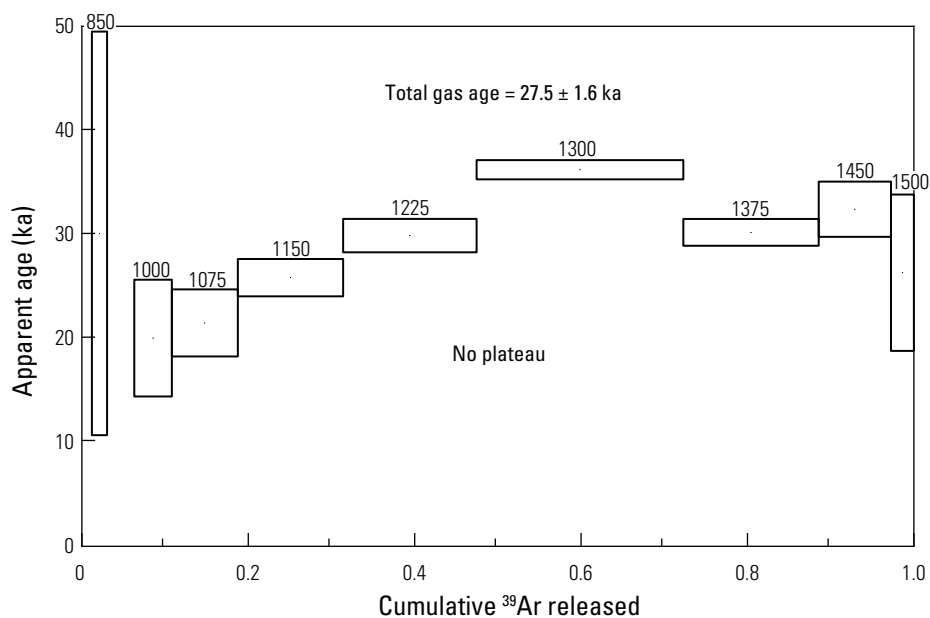


Figure 18.  $^{40}\text{Ar}/^{39}\text{Ar}$  age spectrum (top) and inverse isochron (bottom) for dome 31 sanidine (sample 14MCM12). Apparent age box heights are  $1\sigma$ ; isotopic ratio ellipses are  $2\sigma$ . Isochron age and initial  $^{40}\text{Ar}/^{36}\text{Ar}$  ratio are at the 95% confidence level; total gas age at  $2\sigma$ . On the age spectrum, no plateau was determined for dome 31. The dashed line is the fit to all the isotopic data in the isochron plot, from which an age is derived. Black arrow indicates the  $^{40}\text{Ar}/^{36}\text{Ar}$  atmospheric composition. Complete  $^{40}\text{Ar}/^{39}\text{Ar}$  data is in Appendix 5. MSWD: mean square of weighted deviates.

## DISCUSSION

### Eruption ages of domes of the Mono Craters

$^{238}\text{U}$ – $^{230}\text{Th}$  isochron dating of the outermost rims of zircon and allanite dates the final increment of crystal growth prior to eruption. The  $^{238}\text{U}$ – $^{230}\text{Th}$  isochron ages are thus interpreted to place maximum limits on the eruption age of each Mono Craters dome (e.g., Vazquez and Lidzbarski, 2012; Coombs and Vazquez, 2014; Wright et al., 2015).  $^{238}\text{U}$ – $^{230}\text{Th}$  isochron dating yields high precision (2–5%) Late Pleistocene crystallization ages for the Mono Craters rhyolites. The age results for dome 24 and the newly recognized dome 31 confirm the provisional observations from aerial terrain imagery and titanomagnetite chemistry and verify that two distinct lava flow lobes comprise what was previously mapped as one dome.

Rims on coexisting zircon and allanite from individual Mono Craters rhyolite domes generally yield well-defined  $^{238}\text{U}$ – $^{230}\text{Th}$  isochrons. However, MSWD values for the isochrons when all the data points are included fail the critical MSWD test of Mahon (1996), i.e., the MSWD values are outside the 95% confidence limits for the appropriate degrees of freedom (See Table 1 of Mahon, 1996). This indicates the presence of scatter in the data that is not attributable solely to analytical errors. Because all analyzed zircon and allanite have euhedral crystal shapes and rims that are in contact with groundmass glass (Appendix 2), they are interpreted generally to have been in thermochemical equilibrium with their host rhyolitic melt prior to eruption. Only one zircon from dome 31 is a clear outlier and is interpreted to be a xenocryst (Fig. 14). In total, outliers represent <1% of all zircon and allanite analysis spots (Figs. 12–14, red ellipses), and the

scatter is thus unlikely to indicate incorporation of zircon  $\pm$  allanite that is appreciably older than the age given by the isochron. The elevated MSWD values more likely indicate scatter due to integration of multiple growth zones within a crystal during analysis. If zircon-allanite crystallization was continuous without hiatus, the typical sampled depth of  $\sim 5 \mu\text{m}$  may integrate several hundreds to thousands of years of crystal stratigraphy, depending on the diffusion-controlled growth rates of zircon and allanite in a cooling rhyolitic melt (Watson, 1996; Vazquez and Reid, 2004; Storm et al. 2011).

In pumice-derived allanite and zircon from the Mono Craters-sourced Wilson Creek formation tephra layers, uninterrupted near-rim compositional zoning has been documented and interpreted to suggest near-eruption, continuous crystallization (Vazquez and Lidzbarski, 2012). Euhedral zircon and allanite rims yield statistically coherent and stratigraphically consistent  $^{238}\text{U}$ – $^{230}\text{Th}$  isochron ages for the Wilson Creek formation tephra layers (Vazquez and Lidzbarski, 2012), ages that are concordant with those from other dating methods (Zimmerman et al., 2006; Cox et al., 2012). Results from the study of Vazquez and Lidzbarski (2012) demonstrate that direct sampling of the outermost rims on euhedral zircon and allanite from Mono Craters-sourced rhyolitic tephras can effectively date the timing of eruption.

As noted earlier,  $^{40}\text{Ar}/^{39}\text{Ar}$  dating of sanidine is commonly used to determine the eruption age of felsic volcanic rocks because radiogenic Ar is retained only after post-eruptive cooling. Thus,  $^{40}\text{Ar}/^{39}\text{Ar}$  sanidine ages should overlap with the  $^{238}\text{U}$ – $^{230}\text{Th}$  isochron rim age for each dome within error. However, the sanidines from the dome samples give older  $^{40}\text{Ar}/^{39}\text{Ar}$  ages relative to their zircon-allanite crystallization ages.

Dome 19 has an  $^{40}\text{Ar}/^{39}\text{Ar}$  age of ca. 50 ka and a  $^{238}\text{U}$ – $^{230}\text{Th}$  isochron age of ca. 42 ka, and dome 31 has an  $^{40}\text{Ar}/^{39}\text{Ar}$  age of ca. 32 ka and a  $^{238}\text{U}$ – $^{230}\text{Th}$  isochron age of ca. 26 ka. This lack of agreement is well outside of the analytical uncertainties and means that one of the methods is less reliable for dating of the Mono Craters rhyolites. Either the  $^{238}\text{U}$ – $^{230}\text{Th}$  isochrons are underestimates of the true eruption age or the  $^{40}\text{Ar}/^{39}\text{Ar}$  dates are overestimates of the true eruption age. Because diffusion kinetics predicts that  $^{238}\text{U}$ – $^{230}\text{Th}$  isochrons should give maximum estimates of the eruption age, it is more likely that the  $^{40}\text{Ar}/^{39}\text{Ar}$  dates are anomalously old.

Incorporation of sanidine xenocrysts into the rhyolite magma prior to or during eruption is the simplest explanation for sanidine  $^{40}\text{Ar}/^{39}\text{Ar}$  ages that predate zircon–allanite  $^{238}\text{U}$ – $^{230}\text{Th}$  ages. Indeed, contamination by older material has been a persistent problem in the  $^{40}\text{Ar}/^{39}\text{Ar}$  dating of the Wilson Creek formation tephra layers, where mixed juvenile and xenocrystic populations of sanidine yield  $^{40}\text{Ar}/^{39}\text{Ar}$  ages that are significantly older than the corresponding  $^{238}\text{U}$ – $^{230}\text{Th}$  ages (Kent et al., 2002; Zimmerman et al., 2006; Cassata et al., 2010; Vazquez and Lidzbarski, 2012). However, reconnaissance electron microprobe analysis of 26 sanidine phenocrysts from dome 19 reveals a compositionally homogeneous population (Appendix 6). Moreover, sanidine apparent ages for both domes 19 and 31 generally approximate a Gaussian distribution (Figs. 15 and 16). The absence of obvious xenocrysts from the electron microprobe analysis of sanidine suggests that sanidine crystals yielding slightly older ages may not be true xenocrysts but instead are antecrysts: remobilized older sanidine crystals from earlier episodes of Mono Craters magmatism (Hildreth and Wilson, 2007). Inherited argon from

incompletely degassed sanidine antecrysts entrained during eruption may explain the somewhat elongated “tail” of apparent older grains in the age distribution (Figs. 15 and 16).

The sanidine  $^{40}\text{Ar}/^{39}\text{Ar}$  ages may also be too old because of the presence of excess argon in the juvenile phenocrysts. The initial  $^{40}\text{Ar}/^{36}\text{Ar}$  ratio of dome 19 is distinct at a 95% confidence from the atmospheric ratio (Fig. 15), which is indicative of a modest excess argon component. The gently climbing age spectrum of sanidine from dome 31 also likely reflects the release of a small amount of trapped excess argon (Fig. 18). Excess argon can significantly affect the apparent age because of the low radiogenic yields of the young sanidines (e.g., Renne et al., 1997). The source of excess argon is unknown but is possibly attributable to submicroscopic trapped melt inclusions, which would be released synchronously with the release of radiogenic argon from the mineral lattice and produce anomalously high plateau ages (Kelley, 2002). The linear isotope correlations observed in Figures 15 and 16 and the consistent age results from both laser and incremental heating experiments would require that the sanidines contained the same excess argon concentration (Kelley, 2002). This would be more likely for melt inclusions in juvenile phenocrysts as the source of excess argon, as opposed to randomly incorporated antecrystic or xenocrystic sanidine.

Because of the likely complications with the sanidine  $^{40}\text{Ar}/^{39}\text{Ar}$  dates, the preferred eruption ages are given by the  $^{238}\text{U}$ – $^{230}\text{Th}$  isochrons from euhedral zircon and allanite rims presented in the Results:  $42.5 \pm 1.1$  ka,  $38.0 \pm 1.2$  ka, and  $26.2 \pm 1.2$  ka for domes 19, 24, and 31, respectively (Figs. 12–14).

### **Wilson Creek tephtras as independent age constraints for Mono Craters lavas**

The lack of agreement between the  $^{40}\text{Ar}/^{39}\text{Ar}$  and  $^{238}\text{U}-^{230}\text{Th}$  dates for domes 31, 24, and 19 clearly complicates the interpretation of the age results. However, the Wilson Creek formation provides independent age verification for the Mono Craters domes because it contains independently dated tephra layers (Kent et al., 2002; Zimmerman et al., 2006; Cox et al., 2012; Vazquez and Lidzbarski, 2012) associated with the domes that can be correlated using titanomagnetite chemistry (Marcaida et al., 2014).

Vazquez and Lidzbarski (2012) obtained a  $^{238}\text{U}-^{230}\text{Th}$  zircon-allanite age of  $26.7 \pm 2.1$  ka (recalculated with  $\lambda_{230} = 9.1705 \times 10^{-6} \text{ a}^{-1}$ ; Cheng et al., 2013) for Ash 7 that is in remarkable agreement with the  $^{238}\text{U}-^{230}\text{Th}$  isochron age of  $26.2 \pm 1.2$  ka for dome 31 lava (this study). Their indistinguishable U–Th isochron ages and titanomagnetite chemistry (Fig. 11B) suggest that dome 31 is the extrusive equivalent of Ash 7.

Similarly, Ashes 9–10 are correlated to dome 24 based on closely matching titanomagnetite compositions (Fig. 5C; Marcaida et al., 2014) and general age concordance. Although Ashes 9–10 have not been directly dated, their depositional ages are constrained between ca. 33 ka and ca. 39 ka (Zimmerman et al., 2006; Vazquez and Lidzbarski, 2012), consistent with the  $^{238}\text{U}-^{230}\text{Th}$  isochron age of  $38.0 \pm 1.2$  ka obtained for dome 24 zircon and allanite.

Dome 19 of the Mono Craters is the most likely source of the stratigraphically important Ash 15; the first line of evidence is the distinct compositional bimodality of their respective titanomagnetite populations (Fig. 5B; Marcaida et al., 2014). Second,  $^{238}\text{U}-^{230}\text{Th}$  dating of unpolished euhedral rims of zircon and allanite from Ash 15 pumice

(Vazquez and Lidzbarski, 2012) and dome 19 lava (this study) yielded statistically indistinguishable U–Th isochron ages of  $40.7 \pm 1.9$  ka (recalculated with  $\lambda_{230} = 9.1705 \times 10^{-6} \text{ a}^{-1}$ ; Cheng et al., 2013) and  $42.5 \pm 1.1$  ka, respectively. The age of dome 19 is also consistent with the age of Ash 15 derived from (U–Th)/He dating of allanite (Cox et al., 2012) and age models of Kent et al. (2002) and Zimmerman et al. (2006) from combined  $^{14}\text{C}$  and  $^{40}\text{Ar}/^{39}\text{Ar}$  dating.

The concordance of ages for Ash 15 and its source vent dome 19 confirms that the geomagnetic excursion bisected by Ash 15 (Fig. 4B) is the global Laschamp event dated at  $40.7 \pm 1.0$  ka from combined K–Ar,  $^{40}\text{Ar}/^{39}\text{Ar}$ , and U–Th dating of several lavas at its type locality (Singer et al., 2009). This is a particularly significant result because many researchers have argued for the original interpretation that the excursion in the Wilson Creek formation is the Mono Lake excursion and not the Laschamp excursion (e.g., Cassata et al., 2010; Negrini et al., 2014) despite recent geochronological evidence (Kent et al., 2002; Zimmerman et al., 2006; Cox et al., 2012; Vazquez and Lidzbarski, 2012). As the extrusive equivalent of Ash 15, dome 19 provides independent age verification to the controversial excursion recorded in the Wilson Creek formation.

### **Late Pleistocene volcanism at Mono Craters and vicinity**

Rhyolitic volcanism at Mono Craters is inferred to have begun as early as ca. 64 ka (Zimmerman et al., 2006; Vazquez and Lidzbarski, 2012) and continued until the Recent (Bursik and Sieh, 2013), with the earliest products of explosive volcanic activity recorded as tephra layers in the Wilson Creek formation (Fig. 4A; Lajoie, 1968). However, as discussed earlier, most of the tephra layers of the Wilson Creek formation

are older than 20 ka, and so effusive equivalents were previously assumed to be buried by tephra and lavas from younger Holocene eruptions of aphyric rhyolite (Fig. 3; Wood, 1977, 1983; Bursik and Sieh, 1989). Combined titanomagnetite and geochronologic data here and in Marcaida et al. (2014) provide an unambiguous chronologic link between the currently exposed domes of the Mono Craters and the Late Pleistocene Wilson Creek formation tephra layers (Fig. 19) and demonstrate that high-silica rhyolite dome emplacement of the Mono Craters chain began in the Late Pleistocene.

The porphyritic biotite-bearing rhyolites are the most morphologically subdued domes and yield ages that are ca. 7 ka (dome 11; Vazquez et al., 2013) and ca. 25–28 ka (domes 24 and 19) older than the estimated ca. 13 ka age from the recalibrated hydration-rind chronology of Bursik and Sieh (1989). The newly recognized dome 31, which crosscuts dome 24 lava, is also a porphyritic biotite-bearing rhyolite, but is younger than the underlying dome 24 by at least ca. 12 ka. Each biotite-bearing rhyolite domes of the Mono Craters, extruded between ca. 20 ka (dome 11; Vazquez et al., 2013) and ca. 42 ka (dome 19), likely represents the culmination of an eruptive episode that began with explosive eruptions of tephra deposited in ancient Mono Lake (Figs. 2, 4A, and 19). Most of the Mono Craters-sourced tephra in the Wilson Creek formation, from Ash 19 near the base to Ash 3 near the top, have a similar mineralogical assemblage to the biotite-bearing rhyolite lavas. These tephra deposits, and not just the identified correlative tephra layers (i.e., Ashes 3, 7, 9–10, and 15; Fig. 19), were probably derived from vent-forming eruptions preceding emplacement of similar porphyritic biotite-bearing rhyolite lavas that are now covered by products from younger eruptions.

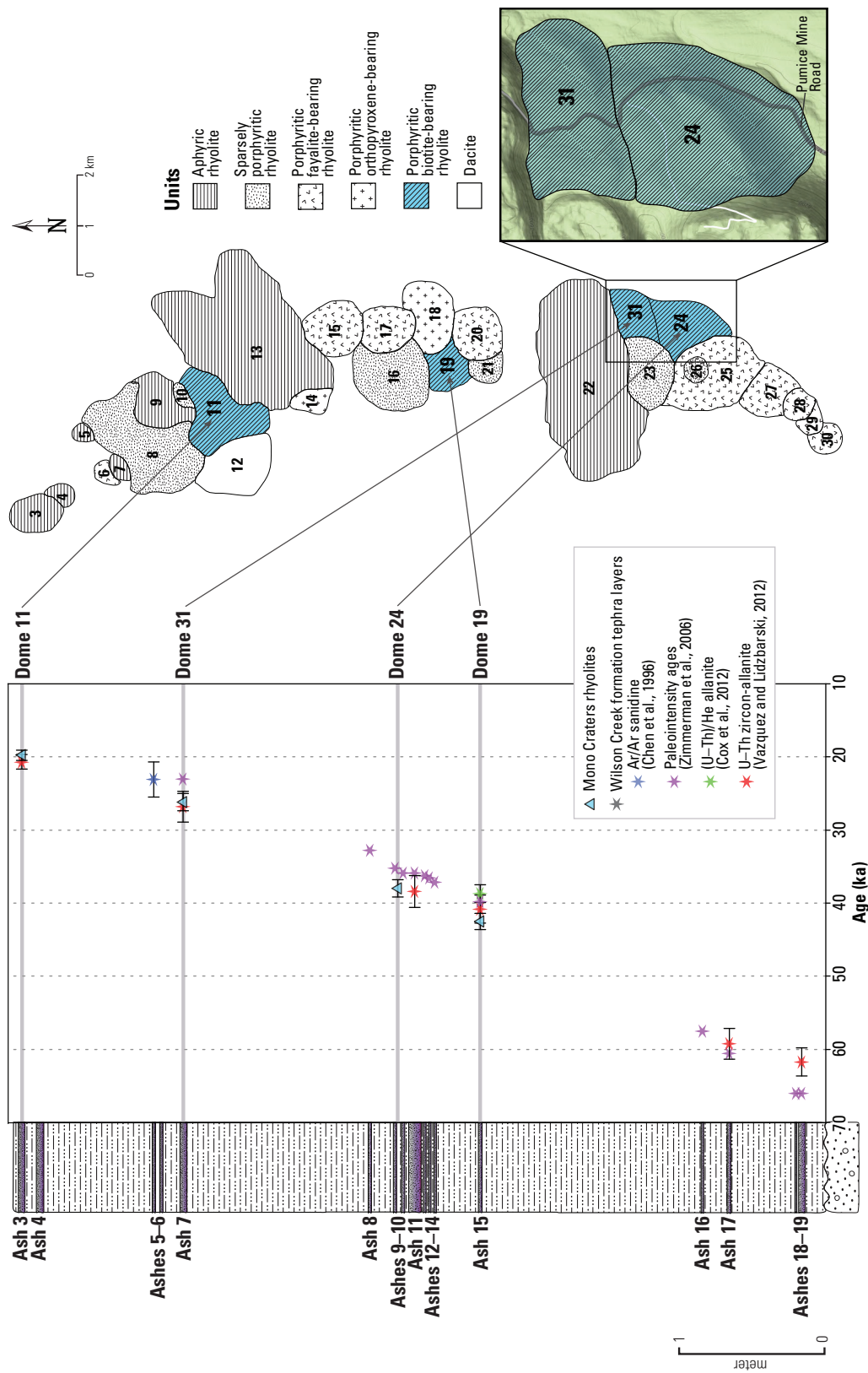


Figure 19. A schematic diagram of Late Pleistocene volcanism at Mono Craters showing the chronology of the Wilson Creek formation tephra layers and several of its identified source vents in the Mono Craters chain. New radiometric ages are reported for the porphyritic-biotite bearing rhyolite domes 19, 24, and 31. The age for dome 11 and Ash 3 is from Vazquez et al. (2013).

The new older ages for domes 19, 24, and 31 indicate a period of rhyolitic extrusion in the Mono Craters chain that is coincident with the 41–27-ka extrusion of trachydacitic lavas in the northwest margin of Long Valley caldera (Fig. 2, inset; Mahood et al., 2010; Hildreth et al., 2014). Likewise, the earliest Mono Craters eruptions (ca. 64–57 ka; Vazquez and Lidzbarski, 2012; Zimmerman et al., 2006) recorded in the Wilson Creek formation (Ashes 19–16; Fig. 19) temporally overlap with several Mammoth Mountain dome-building eruptions (ca. 100–50 ka; Hildreth et al., 2014), and a rhyodacitic tephra layer (Ash 18) of Mammoth Mountain-affinity has been recently documented in the Wilson Creek formation (Marcaida et al., 2014). Late Pleistocene volcanism in the Mono Lake–Long Valley region is thus characterized by broadly contemporaneous eruptions at Mono Craters, Long Valley, and Mammoth Mountain in the interval 64–27 ka.

## CONCLUSIONS

This study reports new U-series and  $^{40}\text{Ar}/^{39}\text{Ar}$  geochronologic data for several domes of the Mono Craters that previously had been poorly dated or whose ages were unknown. These geochronologic data are supplemented by new titanomagnetite geochemistry. The primary conclusions are as follows:

1.  $^{238}\text{U}$ – $^{230}\text{Th}$  isochron dating of zircon and allanite rims from biotite-bearing rhyolite domes 19, 24, and 31 give eruption ages of  $42.5 \pm 1.1$  ka,  $38.0 \pm 1.2$  ka and  $26.2 \pm 1.2$  ka, respectively. These are the oldest ages yet obtained for effusive eruptions from the Mono Craters and extend the chronology of effusive, high-silica rhyolite volcanism back in time, well into the Late Pleistocene.
2. The  $^{40}\text{Ar}/^{39}\text{Ar}$  sanidine laser total-fusion and step-heating ages also indicate Late Pleistocene ages for domes 19, 24, and 31, but the apparent ages are older than the  $^{238}\text{U}$ – $^{230}\text{Th}$  isochrons for the same samples. The older ages for the sanidine likely indicate the presence of excess (non-atmospheric) argon from incompletely degassed antecrysts and/or trapped melt inclusions in juvenile phenocrysts. In contrast, the well-defined  $^{238}\text{U}$ – $^{230}\text{Th}$  isochrons produced by zircon-allanite rims for the same domes demonstrate little to no evidence of antecrystic contamination and instead indicate juvenile crystallization that was occurring up to the time of eruption. These results suggest that  $^{238}\text{U}$ – $^{230}\text{Th}$  rim ages of euhedral zircon and allanite effectively date the timing of dome eruptions.
3. The Late Pleistocene dome-forming eruptions dated in this study can be linked with titanomagnetite geochemistry to dated tephras in the Wilson Creek formation

and together establish unambiguous links between Late Pleistocene eruptions and tephra recorded in the Wilson Creek formation. Additionally, the tephra provide independent age constraints for the verification of the eruption ages, and indicate that the  $^{238}\text{U}$ – $^{230}\text{Th}$  isochrons provide the best estimates of eruption ages for the Mono Craters dome lavas.

## REFERENCES CITED

- Allègre, C.L., 1968,  $^{230}\text{Th}$  dating of volcanic rocks; a comment: *Earth and Planetary Science Letters*: v. 5, p. 209–210.
- Bacon, C.R., Grove, M., Vazquez, J.A., and Coble, M.A., 2012, The Stanford–U.S. Geological Survey SHRIMP ion microprobe—a tool for micro-scale chemical and isotopic analysis: U.S. Geological Survey Fact Sheet 2012–3067, 4 p.
- Bacon, C.R., Persing, H.M., Wooden, J.L., and Ireland, T.R., 2000, Late Pleistocene granodiorite beneath Crater Lake caldera, Oregon, dated by ion microprobe: *Geology*, v. 28, no. 5, p. 467–470.
- Bailey, R.A., 1989, Geologic map of Long Valley Caldera, Mono Inyo Craters volcanic chain, and vicinity, eastern California: U.S. Geological Survey Miscellaneous Investigations Series Map I-1933, 2 sheets, 11 pages, 12 map sheets.
- Bailey, R.A., 2004, Eruptive history and chemical evolution of the precaldera and postcaldera basalt-dacite sequences, Long Valley, California; implications for magma sources, current magmatic unrest, and future volcanism: U.S. Geological Survey Professional Paper 1692, 75 p.
- Benson, L.V., Currey, D.R., Dorn, R.I., Lajoie, K.R., Oviatt, C.G., Robinson, S.W., Smith, G.I., and Stine, S., 1990, Chronology of expansion and contraction of four Great Basin lake systems during the past 35,000 years: *Palaeogeography, Palaeoclimatology, Palaeoecology*, v. 78, no. 3, p. 241–286.
- Benson, L.V., Liddicoat, J., Smoot, J., Sarna-Wojcicki, A.M., Negrini, R. and Lund, S., 2003, Age of the Mono Lake excursion and associated tephra: *Quaternary Science Reviews*, v. 22, no. 2–4, p. 35–140.
- Benson, L.V., Lund, S.P., Burdett, J.W., Kashgarian, M., Rose, T.P., Smoot, J.P. and Schwartz, M., 1998, Correlation of late-Pleistocene lake-level oscillations in Mono Lake, California, with North Atlantic climate events: *Quaternary Research*, v. 49, no. 1, p. 1–10.
- Bonhommet, N., and Zähringer, J., 1969, Paleomagnetism and potassium argon age determinations of the Laschamp geomagnetic polarity event: *Earth and Planetary Science Letters*, v. 6, no. 1, p. 43–46.
- Bursik, M.I., and Sieh, K.E., 1989, Range front faulting and volcanism in the Mono Basin, eastern California: *Journal of Geophysical Research*, v. 94, no. B11, p. 15587–15609.

- Bursik, M.I., and Sieh, K., 2013, Digital database of the Holocene tephras of the Mono–Inyo Craters, California: U.S. Geological Survey Data Series 758.
- Carmichael, I.S.E., 1967, The iron–titanium oxides of salic volcanic rocks and their associated ferromagnesian silicates: *Contributions to Mineralogy and Petrology*, v. 14, no. 1, p. 36–64.
- Cassata, W.S., Singer, B.S., Liddicoat, J.C., and Coe, R.S., 2010, Reconciling discrepant chronologies for the geomagnetic excursion in the Mono Basin, California: Insights from new  $^{40}\text{Ar}/^{39}\text{Ar}$  dating experiments and a revised relative paleointensity correlation: *Quaternary Geochronology*, v. 5, no. 5, p. 533–543.
- Channell, J.E.T., 2006, Late Brunhes polarity excursions (Mono Lake, Laschamp, Iceland Basin and Pringle Falls) recorded at ODP Site 919 (Irminger Basin): *Earth and Planetary Science Letters*, v. 244, no. 1–2, p. 378–393.
- Charlier, B.L., Peate, D.W., Wilson, C.J., Lowenstern, J.B., Storey, M., and Brown, S.J., 2003, Crystallisation ages in coeval silicic magma bodies;  $^{238}\text{U}$ – $^{230}\text{Th}$  disequilibrium evidence from the Rotoiti and Earthquake Flat eruption deposits, Taupo Volcanic Zone, New Zealand: *Earth and Planetary Science Letters*, v. 206, no. 3, p. 441–457.
- Chen, Y., Smith, P.E., Evensen, N.M., York, D. and Lajoie, K.R., 1996, The edge of time; dating young volcanic ash layers with the  $^{40}\text{Ar}/^{39}\text{Ar}$  laser probe: *Science*, v. 274, no. 5290, p. 1176–1178.
- Cheng, H., Edwards, R.L., Shen, C.C., Polyak, V.J., Asmerom, Y., Woodhead, J., Hellstrom, J., Wang, Y., Kong, X., Spötl, C., Wang, X., and Alexander, E.C., 2013, Improvements in  $^{230}\text{Th}$  dating,  $^{230}\text{Th}$  and  $^{234}\text{U}$  half-life values, and U–Th isotopic measurements by multi-collector inductively coupled plasma mass spectrometry: *Earth and Planetary Science Letters*, v. 371, p. 82–91.
- Cherniak, D.J., 2010, Diffusion in accessory minerals; zircon, titanite, apatite, monazite and xenotime: *Reviews in Mineralogy and Geochemistry*, v. 72, no. 1, p. 827–869.
- Coombs, M.L., and Vazquez, J.A., 2014, Cogenetic late Pleistocene rhyolite and cumulate diorites from Augustine Volcano revealed by SIMS  $^{238}\text{U}$ – $^{230}\text{Th}$  dating of zircon, and implications for silicic magma generation by extraction from mush: *Geochemistry, Geophysics, Geosystems*, v. 15, no. 12, p. 4846–4865.
- Cox, S.E., Farley, K.A., and Hemming, S.R., 2012, Insights into the age of the Mono Lake Excursion and magmatic crystal residence time from (U–Th)/He and  $^{230}\text{Th}$  dating of volcanic allanite: *Earth and Planetary Science Letters*, v. 319, p. 178–184.

- Dalrymple, G.B., 1967, Potassium-argon dating of recent rhyolites of the Mono and Inyo Craters, California: *Earth and Planetary Science Letters*, v. 3, p. 289–298.
- Dalrymple, G.B., 1989, The GLM continuous laser system for  $^{40}\text{Ar}/^{39}\text{Ar}$  dating; description and performance characteristics: *U.S. Geological Survey Bulletin* 1890, p. 89–96.
- Dalrymple, G.B., and Lanphere, M.A., 1969, Potassium-argon dating; principles, techniques and applications to geochronology: San Francisco, Freeman, 258 p.
- Dalrymple, G.B., Alexander, Jr., E.C., Lanphere, M.A., Kraker, G.P., 1981, Irradiation of samples for  $^{40}\text{Ar}/^{39}\text{Ar}$  dating using the Geological Survey TRIGA reactor: *U.S. Geological Survey Professional Paper* 1176, 55 p.
- Denham, C.R. and Cox, A., 1971, Evidence that the Laschamp polarity event did not occur 13,300–30,400 years ago: *Earth and Planetary Science Letters*, v. 131, p. 181–190.
- Dickin, A.P., 2005, *Radiogenic isotope geology*: New York, Cambridge University Press, 2nd ed., 492 p.
- Evernden, J.F., and Curtis, G.H., 1965, The potassium-argon dating of late Cenozoic rocks in East Africa and Italy: *Current Anthropology*, v. 6, p. 343–364.
- Fleck, R.J., Sutter, J.F., and Elliot, D.H., 1977, Interpretation of discordant  $^{40}\text{Ar}/^{39}\text{Ar}$  age-spectra of Mesozoic tholeiites from Antarctica: *Geochimica et Cosmochimica Acta*, v. 41, no. 1, p. 15–32.
- Friedman, I., 1968, Hydration rind dates rhyolite flows: *Science*, v. 159, no. 3817, p. 878–880.
- Friedman, I., and Smith, R.L., 1960, Part I, The Development of the Method: *American Antiquity*, p. 476–493.
- Hildreth, E.W., 2004, Volcanological perspectives on Long Valley, Mammoth Mountain, and Mono Craters; several contiguous but discrete systems: *Journal of Volcanology and Geothermal Research*, v. 136, no. 3–4, p. 169–198.
- Hildreth, E.W., Fierstein, J., Champion, D., and Calvert, A., 2014, Mammoth Mountain and its mafic periphery—a late Quaternary volcanic field in eastern California: *Geosphere*, v. 10, no. 6, p. 1315–1365.
- Hildreth, E.W., and Mahood, G.A., 1986, Ring fracture eruption of the Bishop Tuff: *Geological Society of America Bulletin*, v. 97, no. 4, p. 396–403.

- Hildreth, E.W., and Wilson, C.J., 2007, Compositional zoning of the Bishop Tuff: *Journal of Petrology*, v. 48, no. 5, p. 951–999.
- Hu, Q., Smith, P.E., Evensen, N.M., and York, D., 1994, Lasing in the Holocene; extending the  $^{40}\text{Ar}/^{39}\text{Ar}$  laser probe method into the  $^{14}\text{C}$  age range: *Earth and Planetary Science Letters*, v. 123, no. 1–4, p. 331–336.
- Jaffey, A.H., Flynn, K.F., Glendenin, L.E., Bentley, W.T., and Essling, A.M., 1971, Precision measurement of half-lives and specific activities of  $^{235}\text{U}$  and  $^{238}\text{U}$ : *Physical Review C*, v. 4, no. 5, p. 1889–1906.
- Kelleher, P.C., 1986, The Mono Craters–Mono Lake Islands volcanic complex, eastern California; evidence for several magma types, magma mixing, and a heterogeneous source region [M.S. Thesis]: University of California, Santa Cruz, 111 p.
- Kelleher, P.C., and Cameron, K.L., 1990, The geochemistry of the Mono Craters–Mono Lake Islands volcanic complex, eastern California: *Journal of Geophysical Research*, v. 95, no. B11, p. 17643–17659.
- Kelley, S., 2002, Excess argon in K–Ar and Ar–Ar geochronology: *Chemical Geology*, v. 188, no. 1, p. 1–22.
- Kent, D.V., Hemming, S.R., and Turrin, B.D., 2002, Laschamp Excursion at Mono Lake: *Earth and Planetary Science Letters*, v. 197, no. 3–4, p. 151–164.
- Kigoshi, K., 1967, Ionium dating of igneous rocks: *Science*, v. 156, no. 3777, p. 932–934.
- Lajoie, K.R., 1968, Late Quaternary stratigraphy and geologic history of Mono Basin, eastern California [PhD Dissertation]: University of California, Berkeley, 271 p.
- Lanphere, M.A., and Dalrymple, G.B., 2000, First-principles calibration of  $^{38}\text{Ar}$  tracers; implications for the ages of  $^{40}\text{Ar}/^{39}\text{Ar}$  fluence monitors: U.S. Geological Survey Professional Paper 1621, 10 p.
- Liddicoat, J.C., and Coe, R.S., 1979, Mono Lake geomagnetic excursion: *Journal of Geophysical Research*, v. 84, no. B1, p. 261–271.
- Lowenstern, J.B., Persing, H.M., Wooden, J.L., Lanphere, M., Donnelly-Nolan, J., and Grove, T.L., 2000, U–Th dating of single zircons from young granitoid xenoliths; new tools for understanding volcanic processes: *Earth and Planetary Science Letters*, v. 183, no. 1, p. 291–302.

- Ludwig, K.R., 2008, Manual for Isoplot 3.7: Berkeley Geochronology Center Special Publication, no. 4, 77 p.
- Madsen, D.B., Sarna-Wojcicki, A.M., and Thompson, R.S., 2002, A late Pleistocene tephra layer in the southern Great Basin and Colorado Plateau derived from Mono Craters, California: *Quaternary Research*, v. 57, no. 3, p. 382–390.
- Mahon, K., 1996, The New “York” Regression: Application of an improved statistical method to geochemistry, *International Geology Review*, v. 38, 293–303.
- Mahood, G.A., and Hildreth, E.W., 1983, Large partition coefficients for trace elements in high-silica rhyolites: *Geochimica et Cosmochimica Acta*, v. 47, no. 1, p. 11–30.
- Mahood, G.A., Ring, J.H., Manganelli, S., and McWilliams, M.O., 2010, New  $^{40}\text{Ar}/^{39}\text{Ar}$  ages reveal contemporaneous mafic and silicic eruptions during the past 160,000 years at Mammoth Mountain and Long Valley caldera, California: *Geological Society of America Bulletin*, v. 122, no. 3–4, p. 396–407.
- Marcaida, M., Mangan, M.T., Vazquez, J.A., Bursik, M.I., and Lidzbarski, M.I., 2014, Geochemical fingerprinting of Wilson Creek formation tephra layers (Mono Basin, California) using titanomagnetite compositions: *Journal of Volcanology and Geothermal Research*, v. 273, p. 1–14.
- McDougall, I., and Harrison, T.M., 1999, *Geochronology and thermochronology by the  $^{40}\text{Ar}/^{39}\text{Ar}$  method*: New York, Oxford University Press, 212 p.
- Metz, J.M., and Mahood, G.A., 1985, Precursors to the Bishop Tuff eruption; Glass Mountain, Long Valley, California: *Journal of Geophysical Research Solid Earth* (1978–2012), v. 90, no. B13, p. 11121–11126.
- Miller, C.D., 1985, Holocene eruptions at the Inyo volcanic chain, California; implications for possible eruptions in Long Valley Caldera: *Geology*, v. 13, no. 1, p. 14–17.
- Negrini, R.M., McCuan, D.T., Horton, R.A., Lopez, J.D., Cassata, W.S., Channell, J.E., Verosub, K.L., Knott, J.R., Coe, R.S., Liddicoat, J.C., Lund, S.P., Benson, L.V., and Sarna-Wojcicki, A.M., 2014, Nongeocentric axial dipole field behavior during the Mono Lake excursion: *Journal of Geophysical Research Solid Earth*, v. 119, no. 4, p. 2567–2581.
- Nier, A.O., 1950, A redetermination of the relative abundances of the isotopes of carbon, nitrogen, oxygen, argon, and potassium: *Physical Review*, v. 77, no. 6, p. 789–793.

- Putnam, W.C., 1938, The Mono Craters, California: *Geographical Review*, v. 28, no. 1, p. 68–82.
- Reid, M.R., 2003, New ages for young rhyolites, Mono Craters, California; ion microprobing into the Holocene: *Geological Society of America Abstracts with Programs*, v. 35, no. 6, p. 183.
- Reid, M.R., and Coath, C.D., 2000, In situ U–Pb ages of zircons from the Bishop Tuff; no evidence for long crystal residence times: *Geology*, v. 28, no. 5, p. 443–446.
- Reid, M.R., Coath, C.D., Harrison, T.M., and McKeegan, K.D., 1997, Prolonged residence times for the youngest rhyolites associated with Long Valley Caldera;  $^{230}\text{Th}$ – $^{238}\text{U}$  ion microprobe dating of young zircons: *Earth and Planetary Science Letters*, v. 150, no. 1, p. 27–39.
- Renne, P.R., Sharp, W.D., Deino, A.L., Orsi, G., and Civetta, L., 1997,  $^{40}\text{Ar}/^{39}\text{Ar}$  dating into the historical realm; calibration against Pliny the Younger: *Science*, v. 277, no. 5330, p. 1279–1280.
- Rivera, T.A., Storey, M., Zeeden, C., Hilgen, F.J., Kuiper, K., 2011, A refined astronomically calibrated  $^{40}\text{Ar}/^{39}\text{Ar}$  age for Fish Canyon sanidine: *Earth and Planetary Science Letters*, v. 311, p. 420–426.
- Schmitt, A.K., 2011, Uranium series accessory crystal dating of magmatic processes: *Annual Review of Earth and Planetary Sciences*, v. 39, p. 321–349.
- Schmitt, A.K., Stockli, D.F., Lindsay, J.M., Robertson, R., Lovera, O.M., and Kislitsyn, R., 2010, Episodic growth and homogenization of plutonic roots in arc volcanoes from combined U–Th and (U–Th)/He zircon dating: *Earth and Planetary Science Letters*, v. 295, no. 1, p. 91–103.
- Schmitt, A.K., and Vazquez, J.A., 2006, Alteration and remelting of nascent oceanic crust during continental rapture; evidence from zircon geochemistry of rhyolites and xenoliths from the Salton Trough, California: *Earth and Planetary Science Letters*, v. 252, no. 3, p. 260–274.
- Sieh, K.E., and Bursik, M.I., 1986, Most recent eruption of the Mono Craters, eastern central California: *Journal of Geophysical Research*, v. 91, no. B12, p. 12539–12571.
- Simon, J.I., Renne, P.R., and Mundil, R., 2008, Implications of pre-eruptive magmatic histories of zircons for U–Pb geochronology of silicic extrusions: *Earth and Planetary Science Letters*, v. 266, no. 1, p. 182–194.

- Simon, J.I., Vazquez, J.A., Renne, P.R., Schmitt, A.K., Bacon, C.R., and Reid, M.R., 2009, Accessory mineral U–Th–Pb ages and  $^{40}\text{Ar}/^{39}\text{Ar}$  eruption chronology, and their bearing on rhyolitic magma evolution in the Pleistocene Coso volcanic field, California: *Contributions to Mineralogy and Petrology*, v. 158, no. 4, p. 421–446.
- Singer, B.S., Guillou, H., Jicha, B.R., Laj, C., Kissel, C., Beard, B.L., and Johnson, C.M., 2009,  $^{40}\text{Ar}/^{39}\text{Ar}$ , K–Ar and  $^{230}\text{Th}$ – $^{238}\text{U}$  dating of the Laschamp excursion; a radioisotopic tie-point for ice core and climate chronologies: *Earth and Planetary Science Letters*, v. 286, no. 1, p. 80–88.
- Steiger, R., and Jäger, E., 1977, Subcommittee on geochronology; convention on the use of decay constants in geo- and cosmochronology: *Earth and Planetary Science Letters*, v. 36, no. 3, p. 359–362.
- Stelten, M.E., Cooper, K.M., Vazquez, J.A., Reid, M.R., Barfod, G.H., Wimpenny, J., and Yin, Q.Z., 2013, Magma mixing and the generation of isotopically juvenile silicic magma at Yellowstone caldera inferred from coupling  $^{238}\text{U}$ – $^{230}\text{Th}$  ages with trace elements and Hf and O isotopes in zircon and Pb isotopes in sanidine: *Contributions to Mineralogy and Petrology*, v. 166, no. 2, p. 587–613.
- Storm, S., Shane, P., Schmitt, A.K., and Lindsay, J.M., 2011, Contrasting punctuated zircon growth in two syn-erupted rhyolite magmas from Tarawera volcano; insights to crystal diversity in magmatic systems: *Earth and Planetary Science Letters*, v. 301, no. 3–4, p. 511–520.
- Taddeucci, A., Broecker, W.S., and Thurber, D.L., 1968,  $^{230}\text{Th}$  dating of volcanic rocks: *Earth and Planetary Science Letters*, v. 3, p. 338–342.
- Vazquez, J.A., and Lidzbarski, M. I., 2012, High-resolution tephrochronology of the Wilson Creek Formation (Mono Lake, California) and Laschamp event using  $^{238}\text{U}$ – $^{230}\text{Th}$  SIMS dating of accessory mineral rims: *Earth and Planetary Science Letters*, v. 357–358, p. 54–67.
- Vazquez, J.A., and Reid, M.R., 2004, Probing the accumulation history of the voluminous Toba magma: *Science*, v. 305, no. 5686, p. 991–994.
- Vazquez, J.A., Velasco, N.O., Schmitt, A.K., Bleick, H.A., and Stelten, M.E., 2014,  $^{238}\text{U}$ – $^{230}\text{Th}$  dating of chevkinite in high-silica rhyolites from La Primavera and Yellowstone calderas: *Chemical Geology*, v. 390, p. 109–118.
- Watson, E.B., 1996, Dissolution, growth and survival of zircons during crustal fusion; kinetic principles, geological models and implications for isotopic inheritance, *in* Brown, M., Candela, P.A., Peck, D.L., Stephens, W.E., Walker, R.J., and Zen, E.A., eds., *Geological Society of America Special Paper 315*, p. 43–56.

- Wendt, I., and Carl, C., 1991, The statistical distribution of the mean squared weighted deviation: *Chemical Geology Isotope Geoscience Section*, v. 86, no. 4, p. 275–285.
- Wood, S.H., 1977, Distribution, correlation, and radiocarbon dating of late Holocene tephra, Mono and Inyo craters, eastern California: *Geological Society of America Bulletin*, v. 88, no. 1, p. 89–95.
- Wood, S.H., 1983, Chronology of late Pleistocene and Holocene volcanics, Long Valley and Mono Basin geothermal areas, eastern California: U.S. Geological Survey Open-File Report 83–747, 84 p.
- Wright, H.M., Vazquez, J.A., Champion, D.E., Calvert, A.T., Mangan, M.T., Stelten, M., Cooper, K.M., Herzig, C., and Schriener, Jr., A., 2015, Episodic Holocene eruption of the Salton Buttes rhyolites, California, from paleomagnetic, U–Th, and Ar/Ar dating: *Geochemistry, Geophysics, Geosystems*, v. 16, p. 1198–1210.
- York, D., 1969, Least squares fitting of a straight line with correlated errors: *Earth and Planetary Science Letters*, v. 5, p. 320–324.
- Zimmerman, S.H., Hemming, S. R., Kent, D. V., and Searle, S. Y., 2006, Revised chronology for late Pleistocene Mono Lake sediments based on paleointensity correlation to the global reference curve: *Earth and Planetary Science Letters*, v. 252, no. 1–2, p. 94–106.
- Zimmerman, S.H., Hemming, S.R., Hemming, N.G., Tomascak, P. B., and Pearl, C., 2011, High-resolution chemostratigraphic record of late Pleistocene lake-level variability, Mono Lake, California: *Geological Society of America Bulletin*, v. 123, no. 11–12, p. 2320–2334.

Appendix 1. Expanded details of dating methods.

### **<sup>238</sup>U–<sup>230</sup>Th dating method using secondary ion mass spectrometry (SIMS)**

The ion microprobe is a large SIMS instrument that uses a primary beam of high-energy charged particles (ions) focused onto a target sample surface to generate (or “sputter”) secondary ions (both molecular and atomic) that reflect the isotopic and chemical characteristics of the sample. The positive secondary ions generated are extracted and accelerated into the mass spectrometer to be measured and analyzed, and the data collected generally consist of peak heights of different isotopes of an element (for an isotopic analysis), which are converted to isotope ratios for geochronology. Since these peaks are separated according to mass, high mass resolution is needed to fully resolve potential interferences (resulting from coincident masses) under the peaks of interest. The mass resolution is the mass of the peak divided by the base width of that peak ( $M/\Delta M$ ) at 10% of the peak height. The ion microprobe generally operates at mass resolutions on the order of 7000–10000, and its large magnet radius allows full separation of two adjacent masses without reducing the secondary ion intensity (Bacon et al., 2012). The ion microprobe also allows for *in situ* measurements of crystal-face (e.g., Vazquez and Lidzbarski, 2012) and intracrystal isotopic composition (e.g., Vazquez and Reid, 2004) because the primary ion beam can be focused to a diameter of 10–40  $\mu\text{m}$  that removes only a few atomic layers ( $\leq 5 \mu\text{m}$  sputtered pit depth) from the sample surface. Because of its high spatial resolution as well as its high mass resolution, the ion microprobe is routinely used for U-series analysis of accessory minerals (Schmitt, 2011).

## **$^{40}\text{Ar}/^{39}\text{Ar}$ dating method**

In the K–Ar dating method, the contents of K and Ar in a sample are determined by separate isotopic analyses on different splits of the sample, usually by isotope dilution. In contrast, the contents of K and Ar are determined in a single isotopic analysis on the same aliquot of sample in the  $^{40}\text{Ar}/^{39}\text{Ar}$  dating method, after neutron activation transforms some proportion of  $^{39}\text{K}$  to  $^{39}\text{Ar}$ . Conversion of some atoms of  $^{39}\text{K}$  to  $^{39}\text{Ar}$  occurs by bombardment of fast neutrons during irradiation of the K-bearing sample in a nuclear reactor. The amount of  $^{39}\text{Ar}$  derived from neutron bombardment of  $^{39}\text{K}$  ( $^{39}\text{Ar}_\text{K}$ ) is proportional to the amount of  $^{39}\text{K}$  in the sample, which is a proxy for the amount of the parent isotope  $^{40}\text{K}$ , based on the underlying assumption that the relative isotopic abundances of the isotopes of K are essentially constant in nature (Dalrymple and Lanphere, 1969).

Following irradiation, Ar is released from the sample by fusion, extracted in a high-vacuum system, and purified before analysis in a mass spectrometer where the relative abundances of the isotopes of Ar are measured. After correction for peak interferences from “undesirable” Ar isotopes produced by neutron reactions with K and Ca, the  $^{40}\text{Ar}^*/^{39}\text{Ar}_\text{K}$  ratio is derived (see Eq. 3.42 of McDougall and Harrison, 1999), and an age can be calculated because this ratio is proportional to the  $^{40}\text{Ar}^*/^{39}\text{K}$  in the sample, and thus to age. Because the conversion of  $^{39}\text{K}$  to  $^{39}\text{Ar}$  depends upon the duration of the irradiation, the neutron flux, and the neutron capture cross section, a dimensionless irradiation parameter ( $J$ ) is needed to correct for these effects when calculating the  $^{40}\text{Ar}/^{39}\text{Ar}$  age of the sample. For a given irradiation, this parameter  $J$  is determined by

irradiating a standard sample of known age (as a neutron fluence monitor) together with the unknown sample to be dated:

$$J = \frac{(e^{\lambda t} - 1)}{\left( \frac{{}^{40}\text{Ar}^*}{{}^{39}\text{Ar}_K} \right)} \quad (1)$$

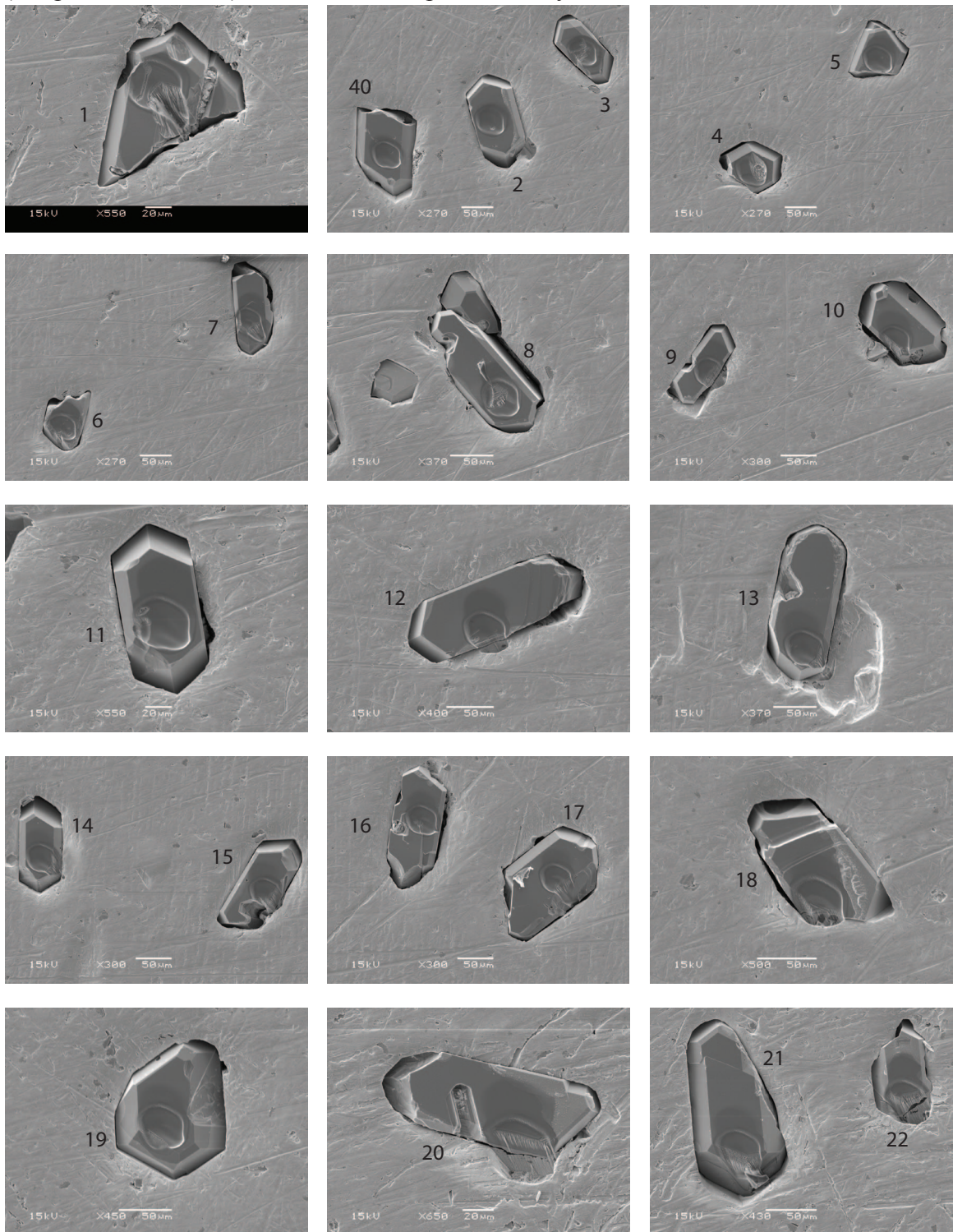
Where  $t$  and  ${}^{40}\text{Ar}^*/{}^{39}\text{Ar}_K$  is the age and the measured isotopic composition of the fluence monitor standard, respectively, and  $\lambda$  is the total decay constant of  ${}^{40}\text{K}$ . The  $J$  value determined for a specific irradiation is used to calculate the age  $t$  of an unknown sample:

$$t = \frac{1}{\lambda} \ln \left( 1 + J \frac{{}^{40}\text{Ar}^*}{{}^{39}\text{Ar}_K} \right) \quad (2)$$

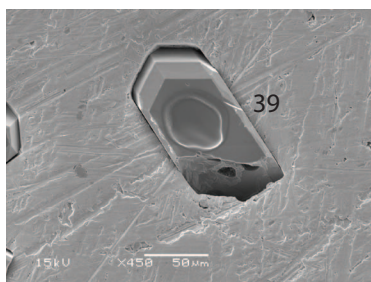
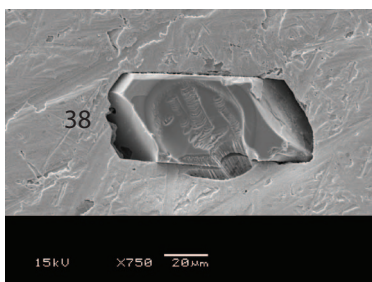
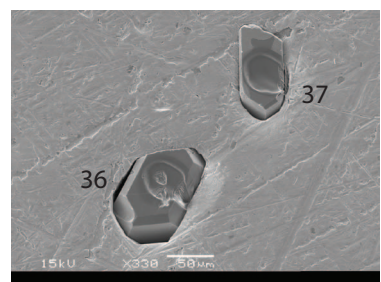
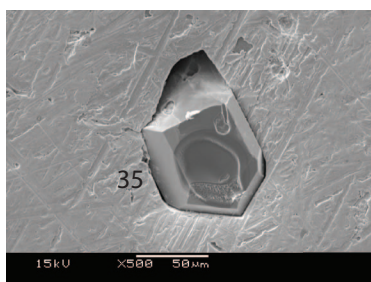
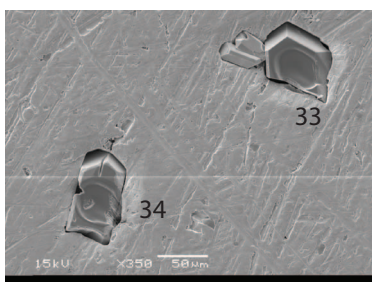
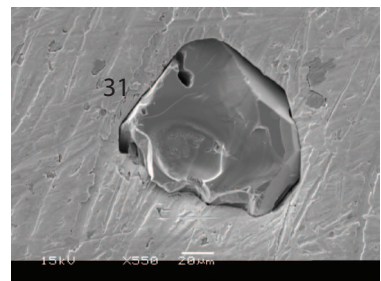
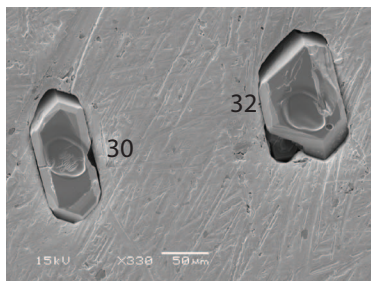
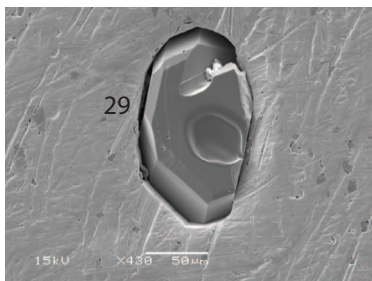
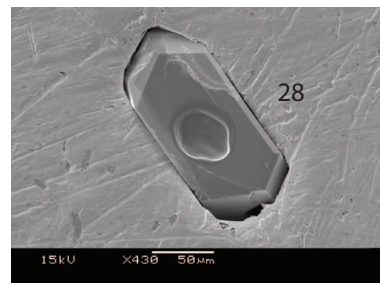
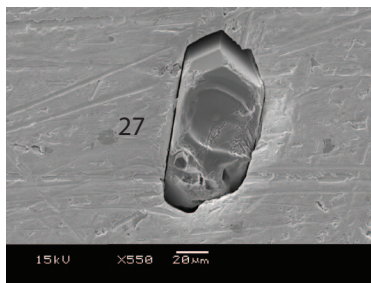
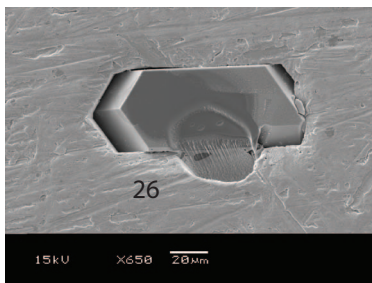
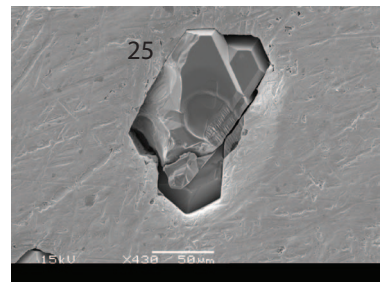
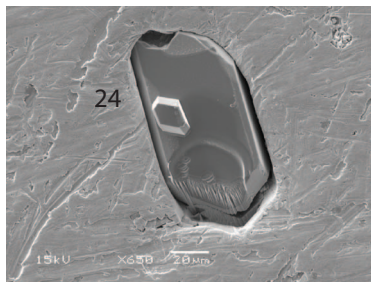
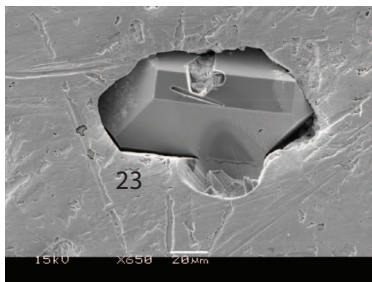
The main advantage of  ${}^{40}\text{Ar}/{}^{39}\text{Ar}$  dating over K–Ar dating is that only Ar isotopic ratios of irradiated samples are needed to calculate an age, which allows analysis of very small sample fractions, even down to the scale of individual crystals. In the  ${}^{40}\text{Ar}/{}^{39}\text{Ar}$  laser fusion technique, gas is released when a continuous laser heats the sample until it melts. With this technique, a total  ${}^{40}\text{Ar}/{}^{39}\text{Ar}$  gas age can be determined for individual crystals, which limits uncertainties coming from sample heterogeneity and allows identification of xenocrystic contamination. In the incremental heating technique, gas is released at several temperature steps and analyzed separately as the sample is incrementally heated from a low temperature until it fuses completely. Such technique results in an age spectrum for the sample, in which an age can be calculated over the gas release plateau. The age can also be obtained using a “normal” isochron diagram ( ${}^{40}\text{Ar}/{}^{36}\text{Ar}$  vs.  ${}^{39}\text{Ar}/{}^{36}\text{Ar}$ ), in which the age is a function of the slope of the regression line, and the Y-intercept yields the  ${}^{40}\text{Ar}/{}^{36}\text{Ar}$  ratio of the initially trapped argon, which, in a

closed isotopic system, should be atmospheric in composition ( $^{40}\text{Ar}/^{36}\text{Ar} = 295.5$ ; Nier, 1950). An alternative is an “inverse” isochron diagram ( $^{36}\text{Ar}/^{40}\text{Ar}$  vs.  $^{39}\text{Ar}/^{40}\text{Ar}$ ), in which the inverse of the X-intercept yields the  $^{40}\text{Ar}^*/^{39}\text{Ar}_K$  ratio, and thus the age (Eq. 2), and the inverse of the Y-intercept yields the initial  $^{40}\text{Ar}/^{36}\text{Ar}$  ratio.

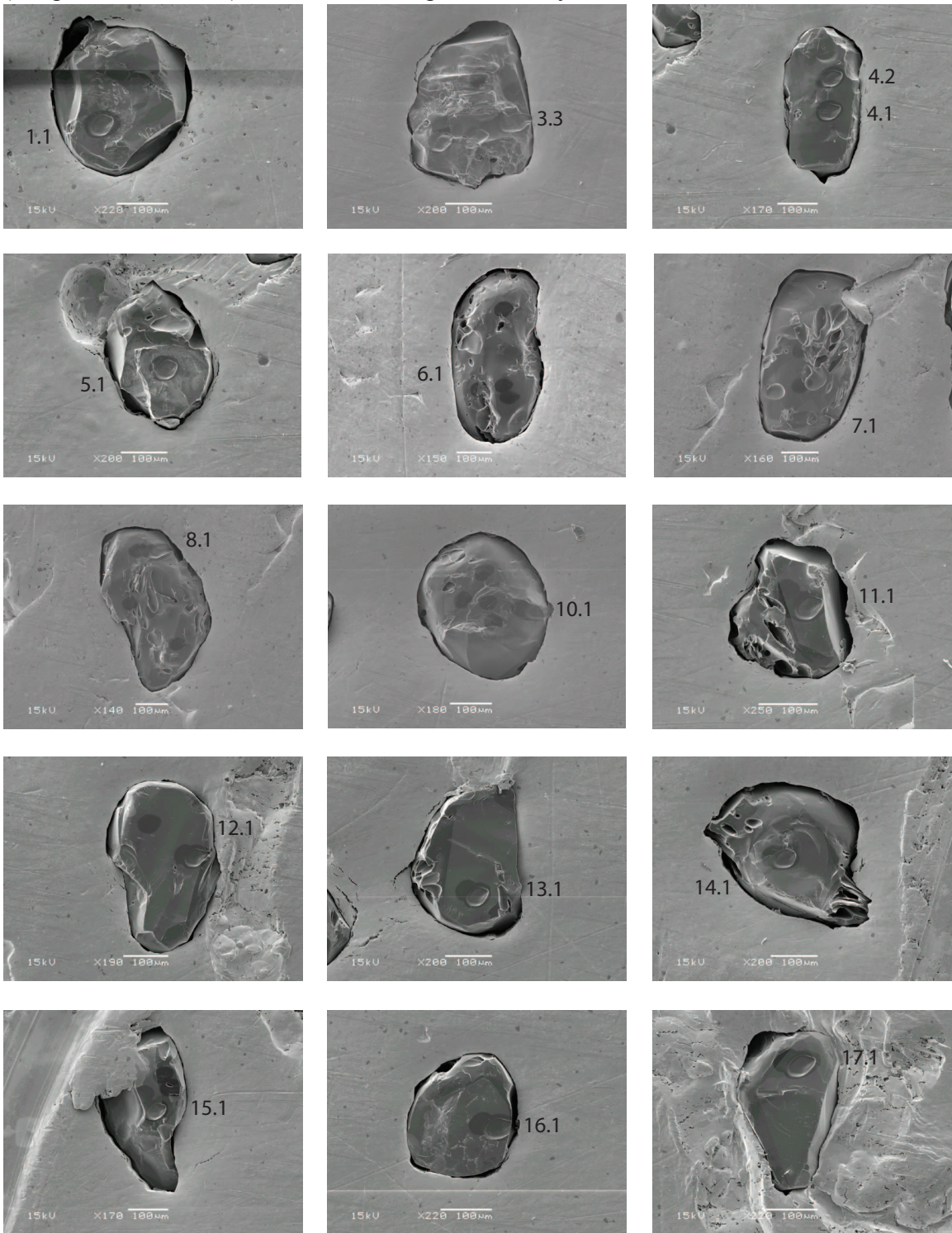
Appendix 2A. Backscattered electron images (BSE) of analyzed zircon from dome 19 (sample 11JAVMC06). Numbers correspond to analysis number in Table 1.



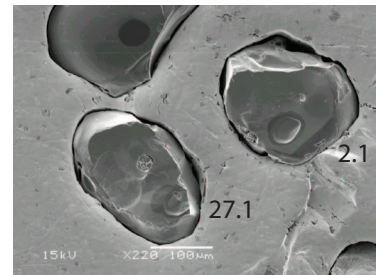
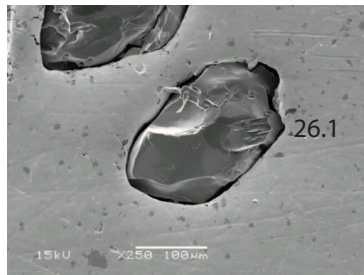
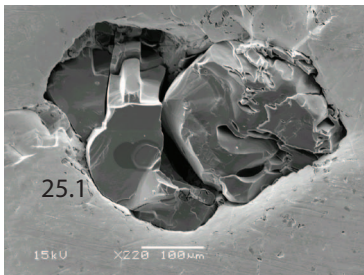
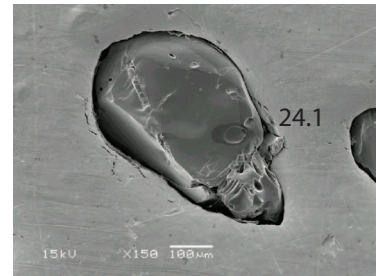
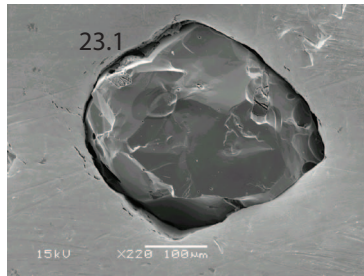
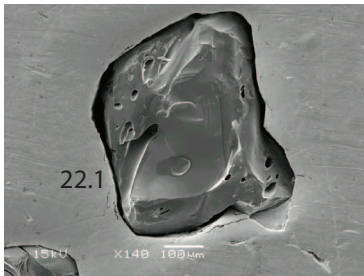
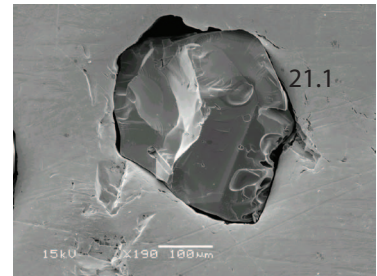
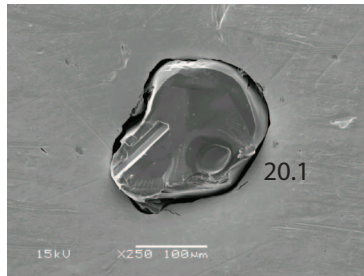
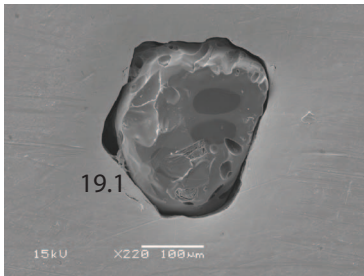
Appendix 2A (continued)



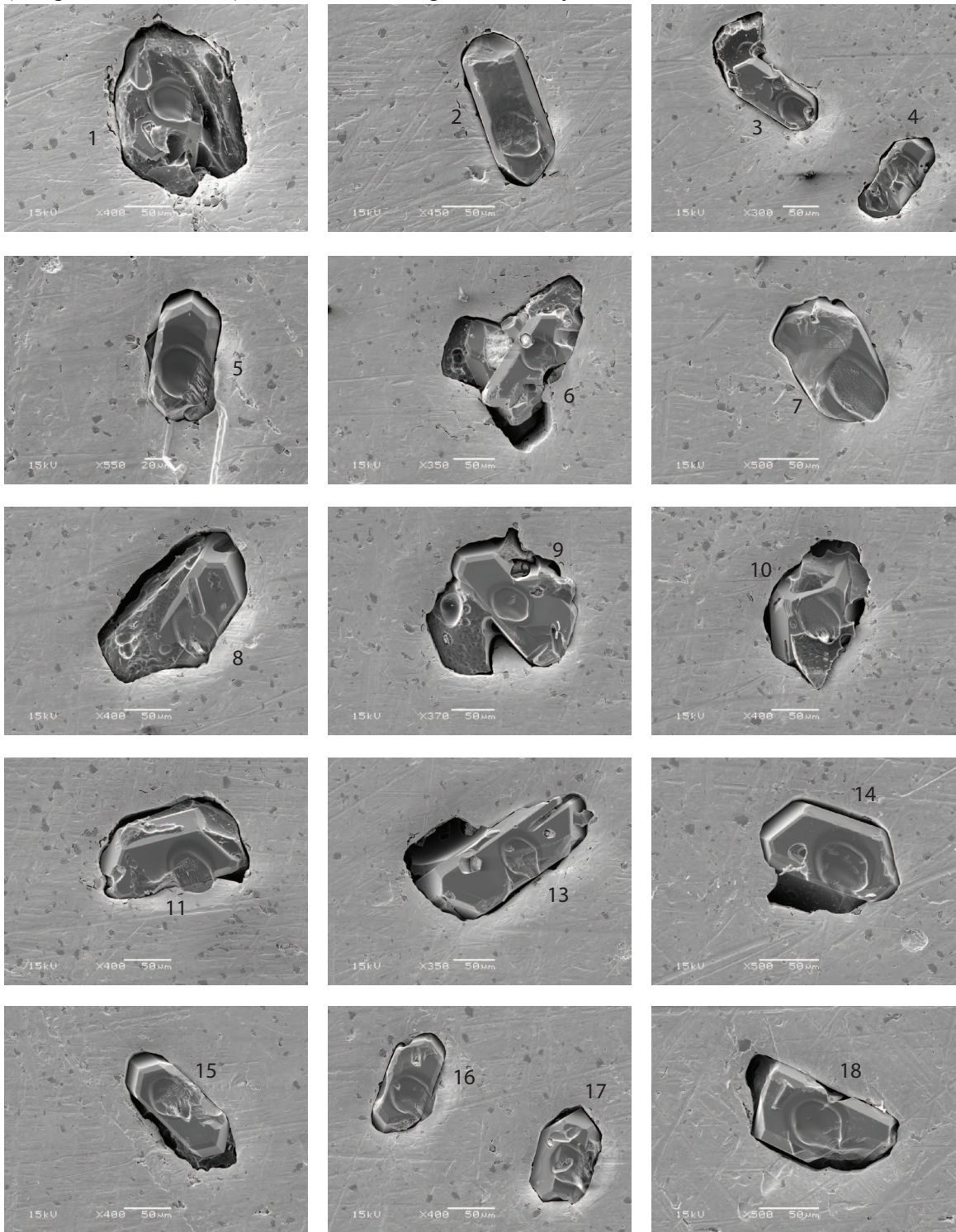
Appendix 2B. Backscattered electron images (BSE) of analyzed allanite from dome 19 (sample 11JAVMC06). Numbers correspond to analysis number in Table 1.



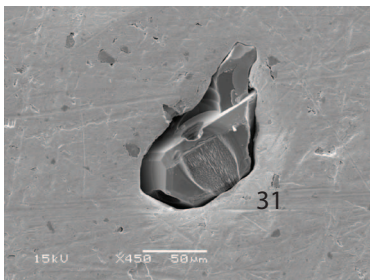
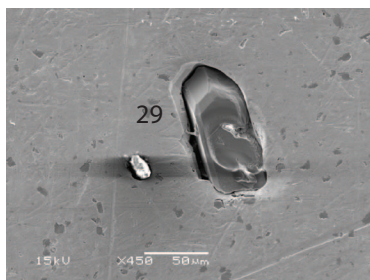
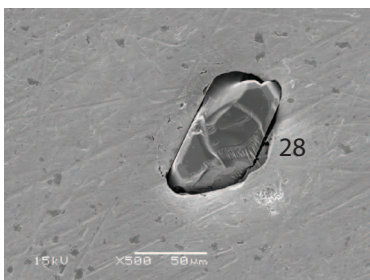
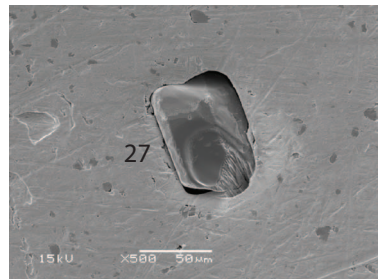
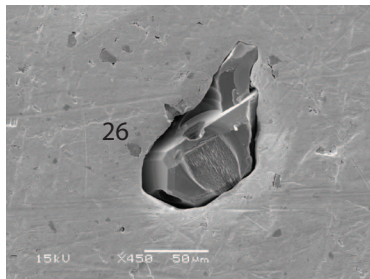
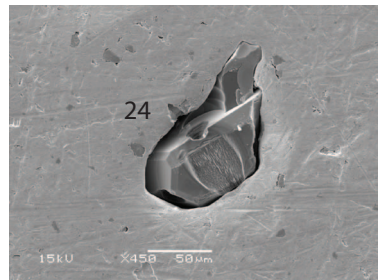
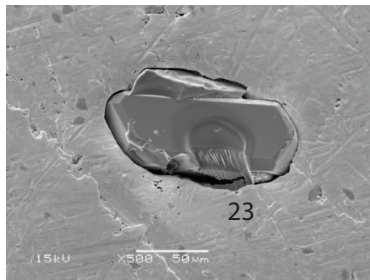
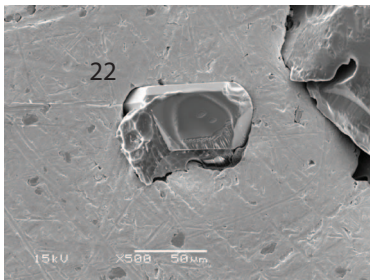
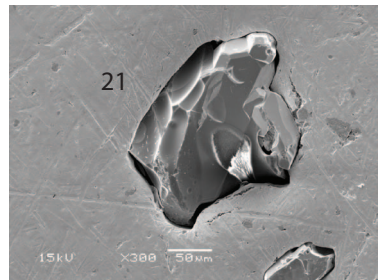
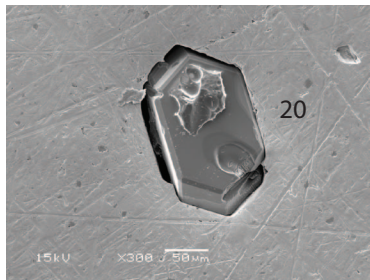
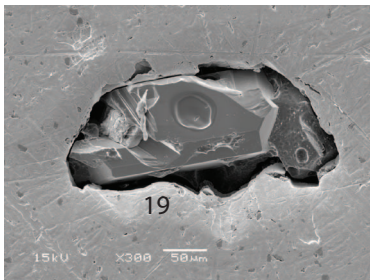
Appendix 2B (continued)



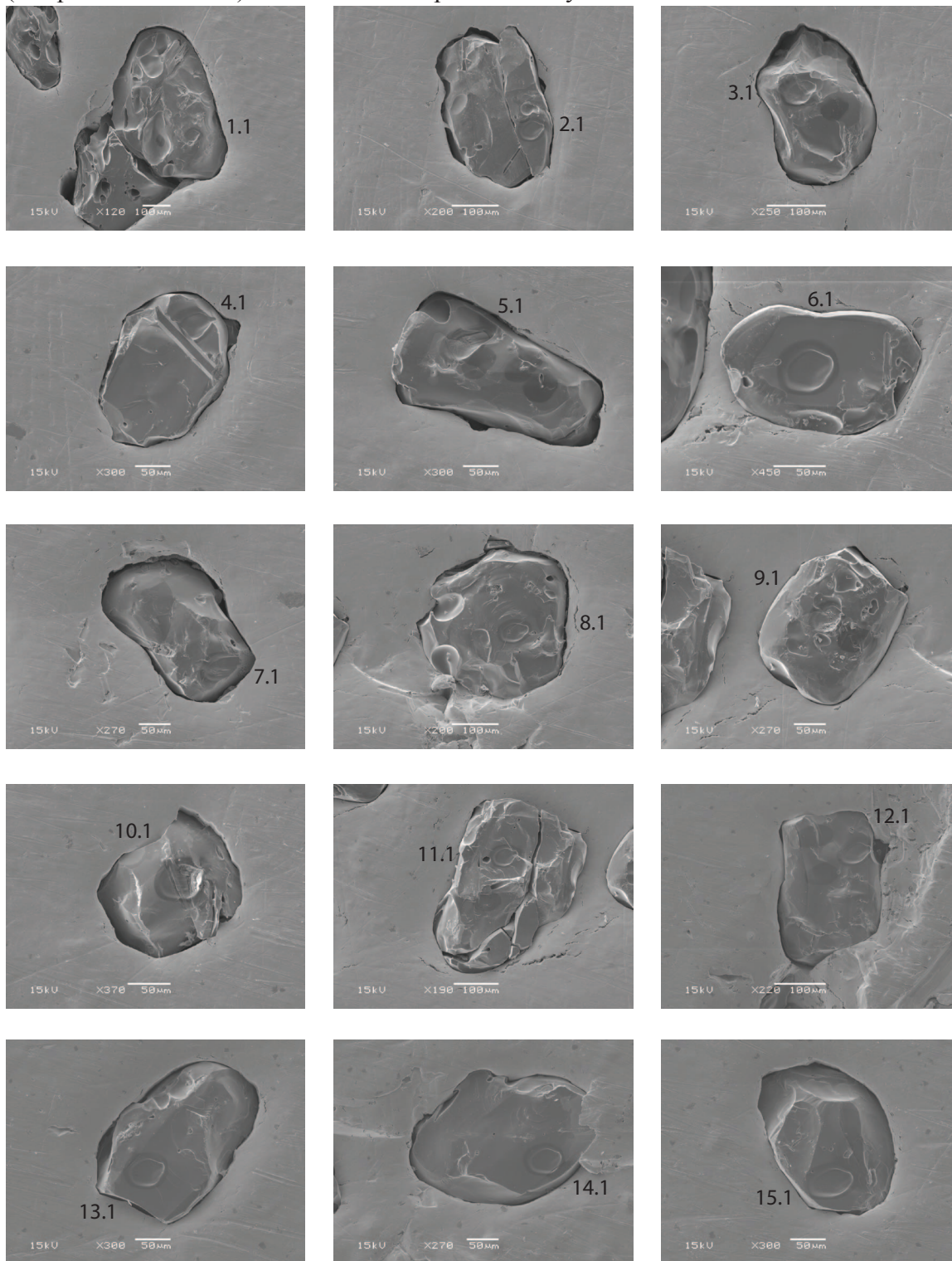
Appendix 2C. Backscattered electron images (BSE) of analyzed zircon from dome 24 (sample 11MCMM05). Numbers correspond to analysis number in Table 1.



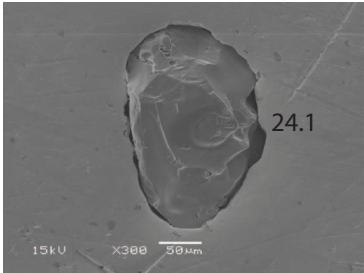
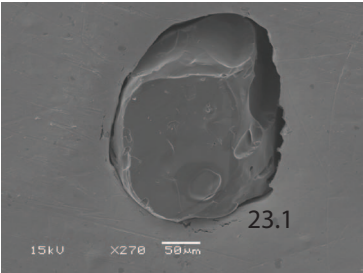
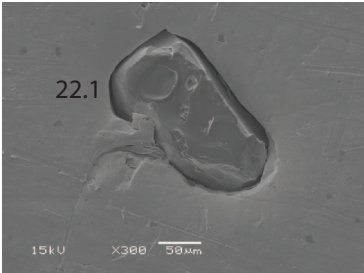
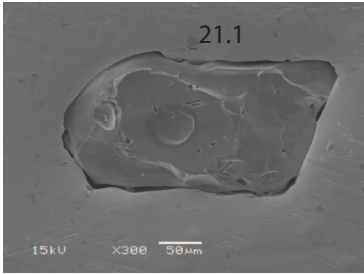
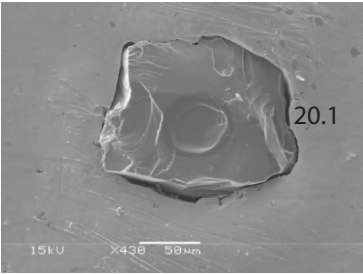
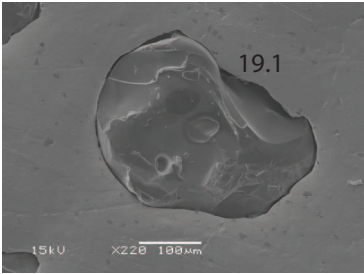
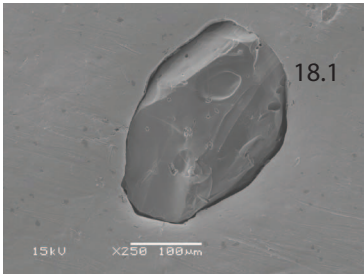
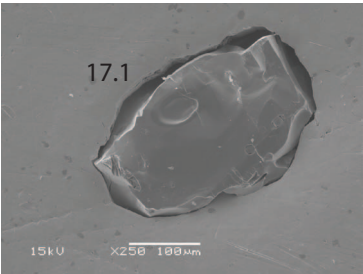
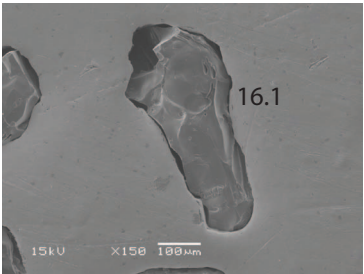
Appendix 2C (continued)



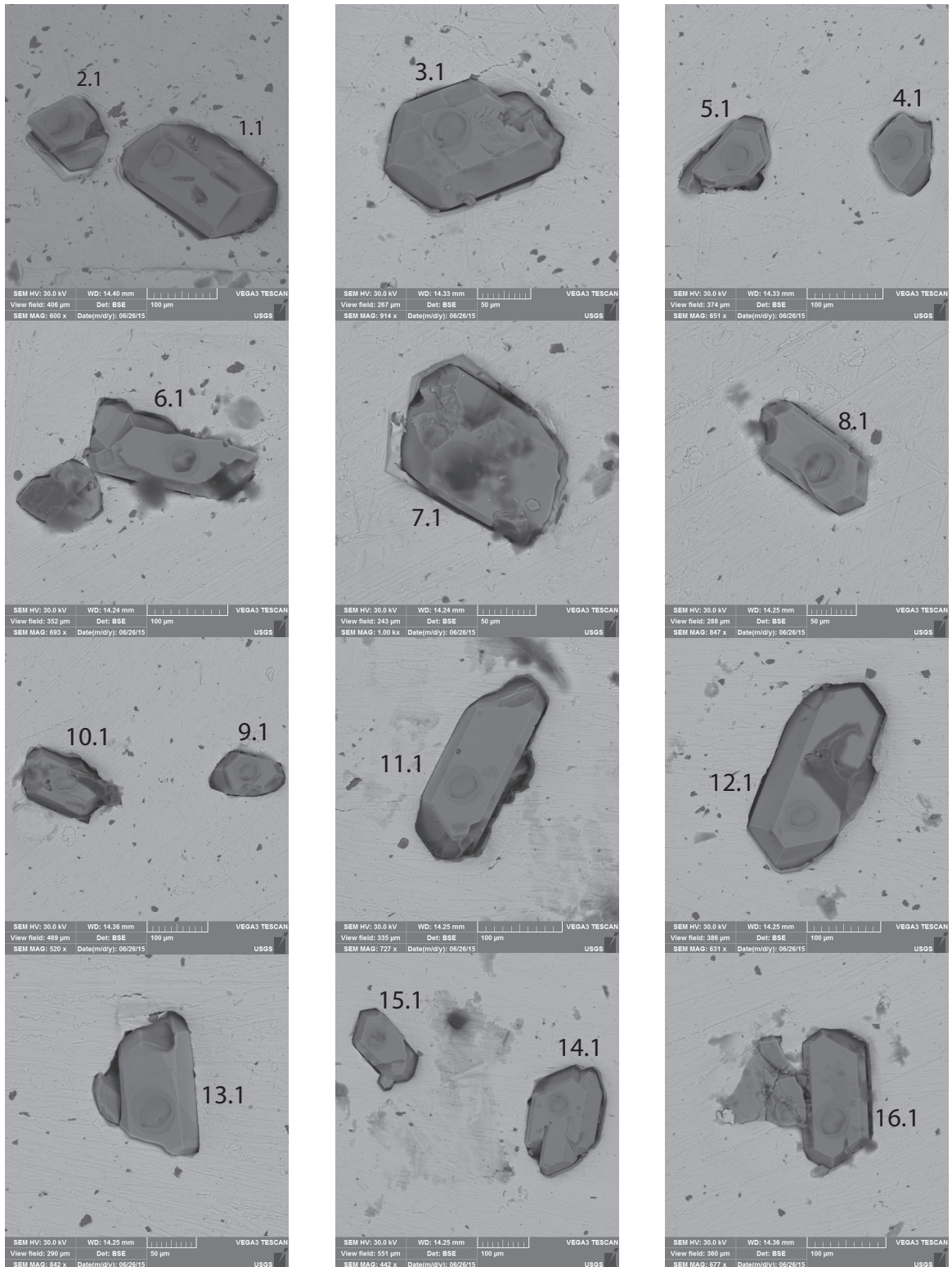
Appendix 2D. Backscattered electron images (BSE) of analyzed allanite from dome 24 (sample 11MCMM05). Numbers correspond to analysis number in Table 1.



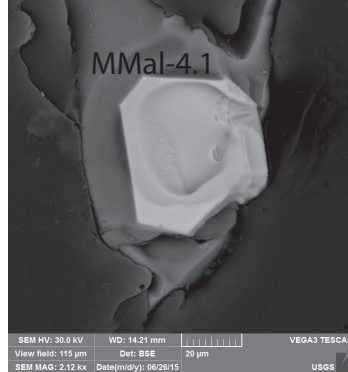
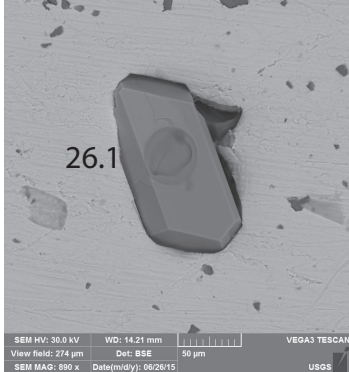
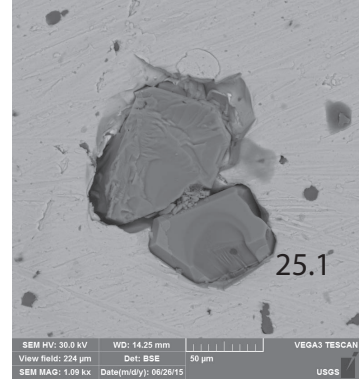
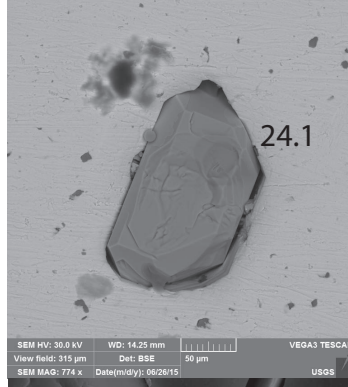
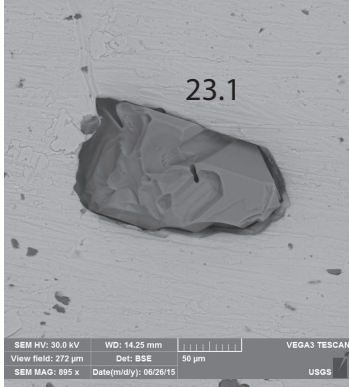
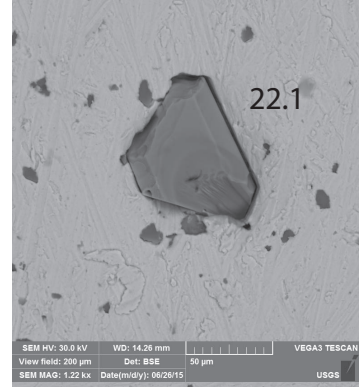
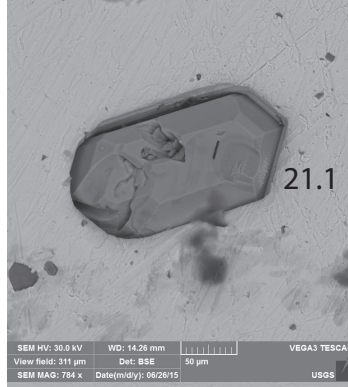
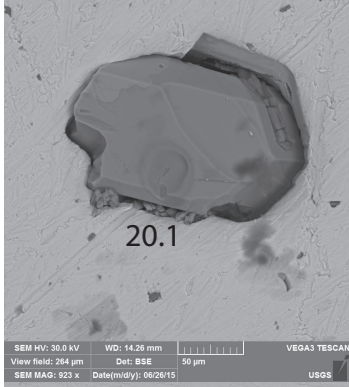
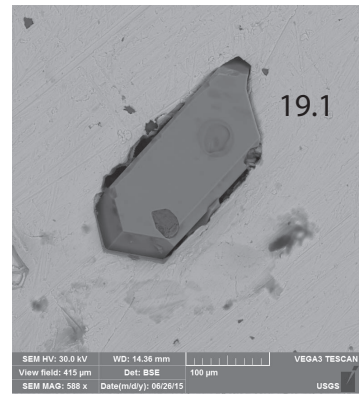
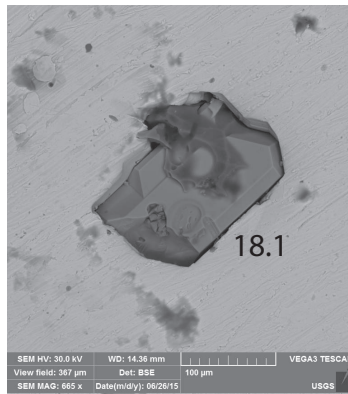
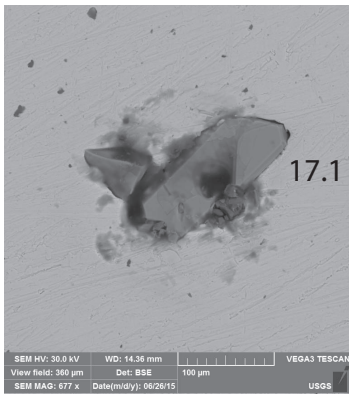
Appendix 2D (continued)



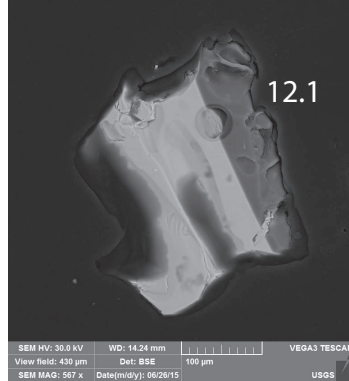
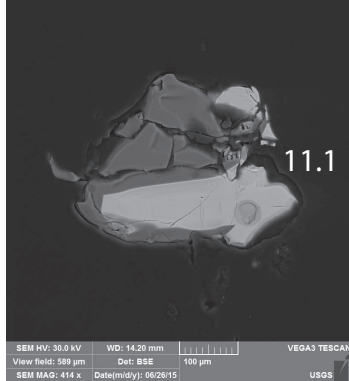
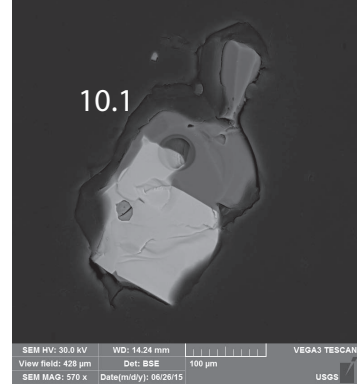
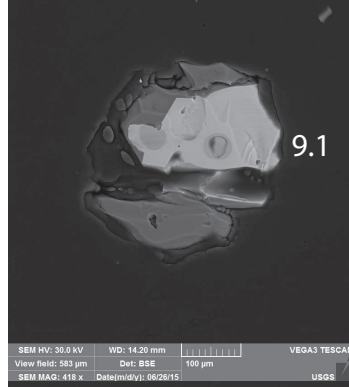
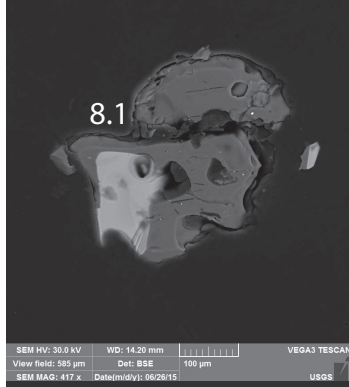
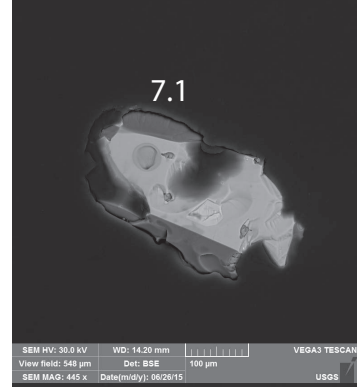
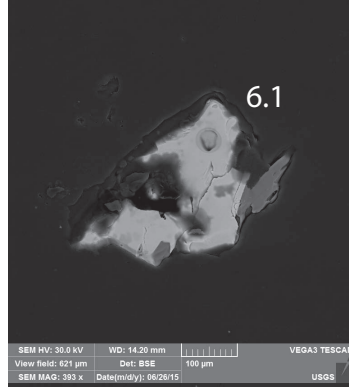
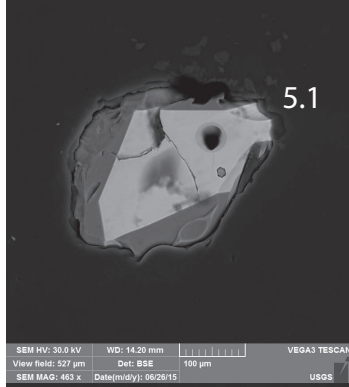
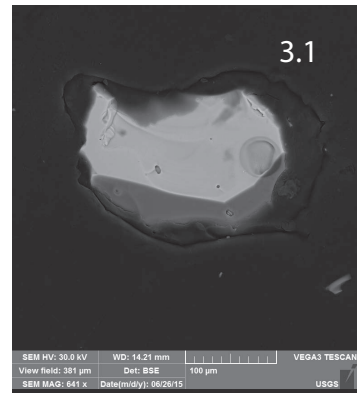
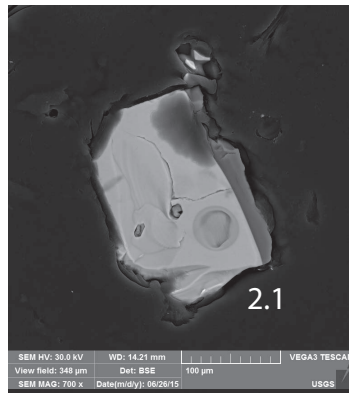
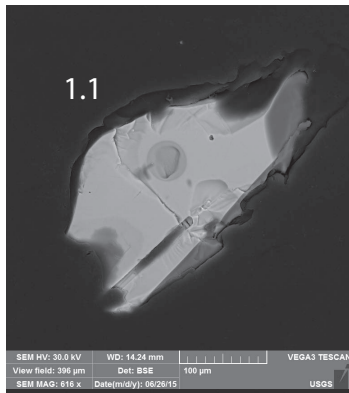
Appendix 2E. Backscattered electron images (BSE) of analyzed zircon from dome 31 (sample 14MCMM12). Numbers correspond to analysis number in Table 1.



Appendix 2E (continued)



Appendix 2F. Backscattered electron images (BSE) of analyzed allanite from dome 31 (sample 14MCMM12). Numbers correspond to analysis number in Table 1.



Appendix 3. Titanomagnetite chemistry of dome 31 (sample 14MCM12).

*Analysis ID	oxide wt%													stdv								
	SiO <sub>2</sub>	TiO <sub>2</sub>	Al <sub>2</sub> O <sub>3</sub>	FeO	MnO	MgO	Cr <sub>2</sub> O <sub>3</sub>	V <sub>2</sub> O <sub>5</sub>	NiO	CaO	Total	SiO <sub>2</sub>	TiO <sub>2</sub>	Al <sub>2</sub> O <sub>3</sub>	FeO	MnO	MgO	Cr <sub>2</sub> O <sub>3</sub>	V <sub>2</sub> O <sub>5</sub>	NiO	CaO	
14MCM12_1	0.11	12.10	1.18	80.82	0.89	0.18	0.00	0.02	0.00	0.01	95.31	0.01	0.03	0.02	0.38	0.04	0.01	0.00	0.02	0.01	0.00	0.00
14MCM12_2	0.09	12.24	1.18	81.75	0.85	0.19	0.00	0.06	0.00	0.00	96.37	0.00	0.08	0.00	0.16	0.02	0.01	0.00	0.02	0.00	0.00	0.00
14MCM12_3	0.09	12.18	1.20	81.14	0.90	0.17	0.02	0.02	0.01	0.01	95.76	0.00	0.14	0.02	0.46	0.07	0.01	0.00	0.03	0.01	0.01	0.01
14MCM12_4	0.09	11.94	1.14	81.09	0.86	0.17	0.00	0.00	0.03	0.00	95.32	0.00	0.04	0.02	0.01	0.03	0.00	0.00	0.00	0.00	0.02	0.00
14MCM12_5	0.07	12.13	1.14	81.28	0.84	0.19	0.00	0.01	0.02	0.00	95.68	0.00	0.08	0.03	0.21	0.02	0.00	0.00	0.01	0.01	0.01	0.00
14MCM12_6	0.11	11.90	1.17	81.13	0.89	0.19	0.00	0.02	0.03	0.01	95.46	0.01	0.17	0.01	0.63	0.02	0.00	0.01	0.00	0.01	0.01	0.00
14MCM12_7	0.11	12.13	1.15	81.62	0.89	0.19	0.01	0.01	0.01	0.02	96.13	0.01	0.10	0.02	0.53	0.03	0.00	0.01	0.01	0.01	0.02	0.00
14MCM12_8	0.09	11.94	1.17	80.92	0.87	0.19	0.01	0.02	0.02	0.01	95.25	0.02	0.11	0.01	1.33	0.03	0.01	0.01	0.03	0.02	0.00	0.00
14MCM12_9	0.10	11.85	1.15	81.14	0.87	0.18	0.00	0.01	0.03	0.00	95.34	0.01	0.12	0.01	1.67	0.03	0.01	0.00	0.01	0.01	0.02	0.00
14MCM12_10	0.09	12.19	1.16	81.98	0.91	0.19	0.00	0.01	0.00	0.01	96.54	0.01	0.26	0.01	0.58	0.02	0.01	0.00	0.02	0.00	0.01	0.01
14MCM12_11	0.09	11.93	1.14	81.89	0.88	0.18	0.01	0.02	0.00	0.00	96.12	0.01	0.18	0.02	0.17	0.02	0.00	0.01	0.01	0.00	0.00	0.00
14MCM12_12	0.10	12.15	1.16	80.80	1.01	0.20	0.00	0.00	0.00	0.01	95.43	0.00	0.09	0.02	0.20	0.02	0.01	0.00	0.00	0.00	0.00	0.01
14MCM12_13	0.11	12.20	1.14	81.46	0.90	0.19	0.00	0.05	0.00	0.00	96.06	0.01	0.05	0.02	0.64	0.01	0.00	0.00	0.03	0.00	0.00	0.00
14MCM12_14	0.08	12.05	1.16	82.18	0.92	0.19	0.00	0.00	0.00	0.00	96.58	0.01	0.10	0.01	0.23	0.01	0.01	0.00	0.00	0.00	0.00	0.00
14MCM12_15	0.10	12.32	1.14	81.30	0.91	0.19	0.00	0.03	0.01	0.00	96.01	0.01	0.07	0.02	0.32	0.02	0.01	0.00	0.02	0.01	0.00	0.00
14MCM12_16	0.09	12.09	1.15	81.90	0.86	0.18	0.00	0.02	0.00	0.01	96.31	0.00	0.17	0.02	0.53	0.02	0.00	0.00	0.02	0.00	0.00	0.00
14MCM12_17	0.11	11.99	1.13	81.83	0.91	0.18	0.01	0.01	0.02	0.00	96.19	0.01	0.12	0.01	0.11	0.04	0.01	0.01	0.01	0.01	0.02	0.00
14MCM12_18	0.10	12.23	1.18	81.44	0.86	0.19	0.00	0.02	0.01	0.01	96.04	0.00	0.12	0.02	0.71	0.03	0.00	0.00	0.00	0.00	0.01	0.01
14MCM12_19	0.11	11.99	1.14	81.56	0.87	0.16	0.01	0.00	0.01	0.01	95.87	0.01	0.14	0.01	0.17	0.03	0.01	0.01	0.00	0.00	0.02	0.01
14MCM12_20	0.10	12.04	1.14	81.82	0.85	0.20	0.01	0.00	0.02	0.01	96.19	0.02	0.12	0.01	0.46	0.03	0.01	0.01	0.00	0.01	0.01	0.01
14MCM12_21	0.11	12.10	1.12	81.67	0.91	0.20	0.00	0.00	0.00	0.00	96.11	0.00	0.11	0.02	0.19	0.04	0.01	0.00	0.00	0.00	0.01	0.00
14MCM12_22	0.09	12.09	1.16	81.78	0.86	0.19	0.00	0.00	0.00	0.01	96.18	0.00	0.05	0.03	0.48	0.05	0.01	0.00	0.00	0.00	0.00	0.00
14MCM12_23	0.11	12.24	1.13	81.42	0.93	0.17	0.00	0.00	0.01	0.00	96.03	0.01	0.14	0.01	0.37	0.01	0.00	0.00	0.00	0.00	0.02	0.00
14MCM12_24	0.09	12.35	1.18	81.59	0.88	0.19	0.00	0.01	0.00	0.01	96.31	0.01	0.01	0.02	0.27	0.02	0.00	0.00	0.02	0.00	0.00	0.00
14MCM12_25	0.11	11.95	1.15	81.45	0.83	0.21	0.02	0.01	0.00	0.00	95.71	0.02	0.14	0.03	0.24	0.02	0.00	0.01	0.01	0.00	0.00	0.00
14MCM12_26	0.11	11.99	1.15	81.73	0.88	0.18	0.01	0.01	0.00	0.01	96.07	0.01	0.18	0.03	0.26	0.03	0.01	0.01	0.02	0.00	0.00	0.01
14MCM12_27	0.09	12.03	1.16	81.70	0.88	0.20	0.00	0.01	0.00	0.01	96.08	0.01	0.18	0.03	0.69	0.03	0.01	0.00	0.01	0.00	0.00	0.01
14MCM12_28	0.11	11.87	1.14	81.76	0.83	0.18	0.01	0.01	0.01	0.00	95.91	0.01	0.10	0.01	0.20	0.03	0.01	0.01	0.01	0.01	0.01	0.00
14MCM12_29	0.12	12.07	1.16	80.91	0.81	0.17	0.00	0.00	0.00	0.00	95.25	0.01	0.01	0.02	0.46	0.04	0.01	0.00	0.00	0.00	0.00	0.00
14MCM12_30	0.09	11.79	1.14	81.68	0.94	0.18	0.00	0.00	0.00	0.01	95.83	0.01	0.09	0.01	0.19	0.04	0.01	0.00	0.00	0.00	0.01	0.01
14MCM12_31	0.09	11.93	1.15	80.31	0.91	0.19	0.01	0.01	0.02	0.01	94.64	0.01	0.25	0.03	0.21	0.03	0.00	0.01	0.00	0.00	0.03	0.01
14MCM12_32	0.10	12.18	1.12	80.54	0.95	0.18	0.00	0.03	0.00	0.01	95.10	0.01	0.26	0.02	0.14	0.05	0.01	0.00	0.00	0.00	0.00	0.00
14MCM12_33	0.09	12.17	1.17	80.35	0.91	0.19	0.00	0.00	0.01	0.00	94.88	0.01	0.16	0.01	0.55	0.03	0.01	0.00	0.00	0.00	0.02	0.00
14MCM12_34	0.10	11.80	1.15	80.92	0.85	0.17	0.01	0.00	0.00	0.00	95.02	0.01	0.08	0.01	1.27	0.01	0.00	0.01	0.01	0.00	0.00	0.00
14MCM12_35	0.10	11.72	1.13	81.17	0.89	0.19	0.01	0.01	0.02	0.00	95.22	0.00	0.10	0.01	0.58	0.05	0.01	0.01	0.01	0.01	0.01	0.00
14MCM12_36	0.10	11.88	1.14	81.49	0.83	0.18	0.02	0.00	0.03	0.00	95.68	0.02	0.23	0.01	0.19	0.03	0.01	0.02	0.01	0.02	0.01	0.00
14MCM12_37	0.09	11.89	1.15	81.90	0.89	0.18	0.02	0.00	0.05	0.00	96.17	0.01	0.18	0.02	0.44	0.04	0.01	0.00	0.00	0.00	0.01	0.00

Reported compositions are averages and standard deviation of 3 point analyses on an individual titanomagnetite crystal.

\*Analysis ID is the name assigned to an individual grain after taking the average of 3 point-analyses.

Run conditions: 20 nA beam current, focused beam, background every 3rd point; standards ran every 60 points.

Oxide standards: TiO<sub>2</sub>, Fe<sub>2</sub>O<sub>3</sub>, Mn<sub>2</sub>O<sub>3</sub>, MgAl<sub>2</sub>O<sub>4</sub>, NiO, Cr<sub>2</sub>O<sub>3</sub>, V<sub>2</sub>O<sub>5</sub>; silicate standard: CPX1 (clinopyroxene)

Appendix 4. Sanidine  $^{40}\text{Ar}/^{39}\text{Ar}$  laser total-fusion data.

Exp #	Apparent age (ka)	$^{40}\text{Ar}^*/^{39}\text{Ar}_K$	% $^{40}\text{Ar}^*$	K/Ca	$^{39}\text{Ar}/^{40}\text{Ar}$	$^{36}\text{Ar}/^{40}\text{Ar}$
<b>Dome 19, sample 11JAVMC06</b>						
Packet IRR332-Y0, single-crystal sanidine						
$J = 0.00022818931391948 \pm 0.0000006259$ ( $1\sigma$ )						
15K0025A	81.13 ± 30.46	0.1971 ± 0.0740	14.88 ± 5.59	47.46 ± 16.46	0.7556 ± 0.0020	0.0029 ± 0.0002
15K0025B	40.00 ± 30.96	0.0972 ± 0.0752	5.58 ± 4.32	40.15 ± 5.69	0.5743 ± 0.0016	0.0032 ± 0.0001
15K0025C	59.72 ± 34.58	0.1451 ± 0.0840	8.50 ± 4.92	44.52 ± 7.66	0.5864 ± 0.0020	0.0031 ± 0.0002
15K0025D	92.18 ± 73.64	0.2239 ± 0.1789	7.17 ± 5.73	59.46 ± 42.69	0.3202 ± 0.0014	0.0031 ± 0.0002
15K0025E	62.17 ± 15.38	0.1510 ± 0.0374	19.55 ± 4.84	50.42 ± 7.85	1.2961 ± 0.0035	0.0027 ± 0.0002
15K0025F	37.59 ± 7.28	0.0913 ± 0.0177	17.73 ± 3.43	60.60 ± 4.91	1.9449 ± 0.0040	0.0028 ± 0.0001
15K0025G	33.94 ± 19.33	0.0824 ± 0.0470	8.69 ± 4.95	88.62 ± 18.23	1.0548 ± 0.0032	0.0031 ± 0.0002
15K0025H	61.26 ± 14.93	0.1488 ± 0.0363	18.87 ± 4.60	57.63 ± 6.86	1.2696 ± 0.0028	0.0027 ± 0.0002
15K0025I	74.83 ± 31.45	0.1818 ± 0.0764	12.29 ± 5.17	166.43 ± 81.20	0.6766 ± 0.0022	0.0030 ± 0.0002
15K0025J	58.61 ± 24.94	0.1424 ± 0.0606	9.96 ± 4.24	66.59 ± 37.58	0.7003 ± 0.0020	0.0030 ± 0.0001
15K0025K	55.80 ± 25.86	0.1355 ± 0.0628	12.01 ± 5.56	55.71 ± 15.03	0.8865 ± 0.0025	0.0030 ± 0.0002
15K0025L	72.66 ± 32.09	0.1765 ± 0.0780	7.66 ± 3.38	74.30 ± 40.68	0.4344 ± 0.0011	0.0031 ± 0.0001
15K0025M	58.84 ± 31.96	0.1429 ± 0.0776	9.56 ± 5.20	68.47 ± 34.23	0.6697 ± 0.0022	0.0031 ± 0.0002
15K0025N	-17.42 ± 56.82	-0.0423 ± 0.1380	-1.31 ± 4.28	20.37 ± 3.05	0.3105 ± 0.0013	0.0034 ± 0.0001
15K0025P	123.65 ± 45.31	0.3004 ± 0.1101	17.66 ± 6.47	65.67 ± 33.33	0.5882 ± 0.0022	0.0028 ± 0.0002
15K0025P	160.18 ± 40.31	0.3891 ± 0.0979	22.87 ± 5.76	78.49 ± 48.88	0.5882 ± 0.0021	0.0026 ± 0.0002
15K0025Q	77.59 ± 39.03	0.1885 ± 0.0948	12.94 ± 6.51	75.50 ± 41.23	0.6869 ± 0.0022	0.0029 ± 0.0002
15K0025Q	108.36 ± 34.91	0.2632 ± 0.0848	18.07 ± 5.82	89.72 ± 59.49	0.6870 ± 0.0022	0.0028 ± 0.0002
15K0025R	70.26 ± 33.31	0.1707 ± 0.0809	10.50 ± 4.98	69.88 ± 20.40	0.6157 ± 0.0020	0.0030 ± 0.0002
15K0025R	94.62 ± 30.31	0.2298 ± 0.0736	14.14 ± 4.53	79.06 ± 27.12	0.6157 ± 0.0020	0.0029 ± 0.0002
15K0025S	83.85 ± 24.81	0.2037 ± 0.0603	21.95 ± 6.49	58.49 ± 12.34	1.0787 ± 0.0032	0.0026 ± 0.0002
15K0025S	102.17 ± 22.52	0.2482 ± 0.0547	26.76 ± 5.90	63.09 ± 14.76	1.0792 ± 0.0031	0.0025 ± 0.0002
15K0025T	52.40 ± 28.39	0.1273 ± 0.0690	11.80 ± 6.39	57.04 ± 8.62	0.9278 ± 0.0029	0.0030 ± 0.0002
15K0025T	74.78 ± 25.38	0.1817 ± 0.0617	16.84 ± 5.72	62.48 ± 11.13	0.9281 ± 0.0029	0.0028 ± 0.0002
15K0025U	61.08 ± 16.89	0.1484 ± 0.0410	21.48 ± 5.94	78.39 ± 20.98	1.4496 ± 0.0032	0.0027 ± 0.0002
15K0025U	73.96 ± 15.21	0.1797 ± 0.0370	26.02 ± 5.35	84.20 ± 24.58	1.4504 ± 0.0031	0.0025 ± 0.0002
15K0025V	9.63 ± 44.62	0.0234 ± 0.1084	1.46 ± 6.78	90.53 ± 53.90	0.6259 ± 0.0021	0.0033 ± 0.0002
15K0025V	43.33 ± 40.30	0.1053 ± 0.0979	6.58 ± 6.12	114.48 ± 88.91	0.6259 ± 0.0021	0.0032 ± 0.0002
15K0025W	155.32 ± 45.89	0.3773 ± 0.1115	21.03 ± 6.21	89.16 ± 65.74	0.5576 ± 0.0017	0.0027 ± 0.0002
15K0025X	75.33 ± 42.69	0.1830 ± 0.1037	11.65 ± 6.60	50.60 ± 10.24	0.6371 ± 0.0021	0.0030 ± 0.0002
15K0025Y	6.25 ± 58.86	0.0152 ± 0.1430	0.68 ± 6.42	83.26 ± 45.41	0.4495 ± 0.0016	0.0034 ± 0.0002
15K0025Z	62.82 ± 23.33	0.1526 ± 0.0567	15.15 ± 5.63	110.09 ± 33.98	0.9940 ± 0.0027	0.0029 ± 0.0002
15K0026A	55.85 ± 42.86	0.1357 ± 0.1041	1.42 ± 1.09	94.17 ± 33.22	0.1048 ± 0.0002	0.0033 ± 0.0000
15K0026B	102.15 ± 51.74	0.2481 ± 0.1257	3.57 ± 1.81	83.93 ± 41.65	0.1437 ± 0.0004	0.0033 ± 0.0001
15K0026C	55.25 ± 37.78	0.1342 ± 0.0918	8.25 ± 5.64	58.80 ± 31.61	0.6153 ± 0.0019	0.0031 ± 0.0002
15K0026D	52.77 ± 37.02	0.1282 ± 0.0899	7.87 ± 5.52	74.32 ± 27.32	0.6144 ± 0.0020	0.0031 ± 0.0002
15K0026E	-38.01 ± 77.31	-0.0923 ± 0.1878	-0.39 ± 0.79	73.35 ± 32.37	0.0423 ± 0.0001	0.0034 ± 0.0000
15K0026F	65.92 ± 25.75	0.1601 ± 0.0626	10.91 ± 4.26	73.20 ± 18.44	0.6816 ± 0.0016	0.0030 ± 0.0001

Appendix 4 (continued)

Exp #	Apparent age (ka)	$^{40}\text{Ar}^*/^{39}\text{Ar}_K$	% $^{40}\text{Ar}^*$	K/Ca	$^{39}\text{Ar}/^{40}\text{Ar}$	$^{36}\text{Ar}/^{40}\text{Ar}$
<b>Dome 19, sample 11JAVMC06</b>						
Packet IRR332-YQ, multi-crystal sanidine						
$J = 0.00022775275545189 \pm 0.0000004571 (1\sigma)$						
15K0087A	59.75 ± 5.26	0.1454 ± 0.0128	24.09 ± 2.12	55.58 ± 6.51	1.6596 ± 0.0024	0.0026 ± 0.0001
15K0087B	60.39 ± 6.86	0.1470 ± 0.0167	30.67 ± 3.48	63.04 ± 11.08	2.0913 ± 0.0041	0.0023 ± 0.0001
15K0087C	47.66 ± 4.29	0.1160 ± 0.0104	32.85 ± 2.95	28.82 ± 1.83	2.8401 ± 0.0054	0.0023 ± 0.0001
15K0087D	52.75 ± 4.63	0.1284 ± 0.0113	35.10 ± 3.08	60.77 ± 7.49	2.7417 ± 0.0055	0.0022 ± 0.0001
15K0087E	41.43 ± 4.57	0.1008 ± 0.0111	30.22 ± 3.33	71.97 ± 13.68	3.0054 ± 0.0062	0.0024 ± 0.0001
15K0087F	48.55 ± 3.50	0.1182 ± 0.0085	34.37 ± 2.47	59.35 ± 6.92	2.9178 ± 0.0054	0.0022 ± 0.0001
15K0087G	51.08 ± 5.28	0.1243 ± 0.0129	32.82 ± 3.40	51.36 ± 5.79	2.6472 ± 0.0062	0.0023 ± 0.0001
15K0087H	50.78 ± 8.52	0.1236 ± 0.0207	22.96 ± 3.85	11.73 ± 0.78	1.8615 ± 0.0042	0.0026 ± 0.0001
15K0087I	58.19 ± 6.05	0.1416 ± 0.0147	33.86 ± 3.52	70.66 ± 14.02	2.3969 ± 0.0062	0.0022 ± 0.0001
15K0087J	52.36 ± 5.45	0.1274 ± 0.0133	35.01 ± 3.64	85.49 ± 17.72	2.7550 ± 0.0071	0.0022 ± 0.0001
15K0087K	41.22 ± 6.21	0.1003 ± 0.0151	26.68 ± 4.02	59.12 ± 8.06	2.6669 ± 0.0062	0.0025 ± 0.0001
15K0087L	48.80 ± 5.71	0.1188 ± 0.0139	29.04 ± 3.40	68.64 ± 12.35	2.4510 ± 0.0057	0.0024 ± 0.0001
15K0087M	39.02 ± 5.54	0.0950 ± 0.0135	25.08 ± 3.56	59.02 ± 9.96	2.6478 ± 0.0070	0.0025 ± 0.0001
15K0087N	48.55 ± 6.01	0.1182 ± 0.0146	29.80 ± 3.69	71.11 ± 13.35	2.5280 ± 0.0057	0.0024 ± 0.0001
15K0087O	53.51 ± 11.12	0.1302 ± 0.0271	22.46 ± 4.67	11.99 ± 0.79	1.7277 ± 0.0048	0.0026 ± 0.0002
15K0087P	41.16 ± 7.68	0.1002 ± 0.0187	23.02 ± 4.29	53.09 ± 9.67	2.3033 ± 0.0055	0.0026 ± 0.0001
15K0087Q	57.24 ± 4.73	0.1393 ± 0.0115	39.29 ± 3.25	57.29 ± 5.95	2.8287 ± 0.0056	0.0021 ± 0.0001
15K0087R	42.60 ± 5.96	0.1037 ± 0.0145	25.62 ± 3.59	60.65 ± 7.01	2.4775 ± 0.0059	0.0025 ± 0.0001
15K0087S	45.29 ± 6.80	0.1102 ± 0.0166	24.89 ± 3.74	63.27 ± 12.62	2.2627 ± 0.0065	0.0025 ± 0.0001
15K0087T	61.13 ± 7.92	0.1488 ± 0.0193	26.43 ± 3.43	45.60 ± 7.05	1.7797 ± 0.0043	0.0025 ± 0.0001
15K0087U	35.61 ± 8.01	0.0867 ± 0.0195	18.79 ± 4.23	93.05 ± 26.25	2.1732 ± 0.0055	0.0027 ± 0.0001
15K0087V	37.63 ± 4.87	0.0916 ± 0.0119	23.89 ± 3.09	57.50 ± 6.63	2.6160 ± 0.0051	0.0026 ± 0.0001
15K0087W	48.45 ± 6.39	0.1179 ± 0.0156	28.17 ± 3.72	90.69 ± 24.03	2.3945 ± 0.0055	0.0024 ± 0.0001
15K0087X	37.86 ± 7.40	0.0921 ± 0.0180	20.62 ± 4.03	10.21 ± 0.68	2.2430 ± 0.0054	0.0027 ± 0.0001
15K0087Y	45.92 ± 6.58	0.1118 ± 0.0160	27.59 ± 3.95	103.01 ± 19.18	2.4743 ± 0.0059	0.0024 ± 0.0001
15K0088A	45.17 ± 4.98	0.1099 ± 0.0121	24.19 ± 2.66	78.68 ± 14.34	2.2050 ± 0.0049	0.0026 ± 0.0001
15K0088B	49.11 ± 5.07	0.1195 ± 0.0123	34.07 ± 3.52	59.95 ± 9.57	2.8591 ± 0.0068	0.0022 ± 0.0001
15K0088C	41.54 ± 4.94	0.1011 ± 0.0120	30.01 ± 3.57	56.87 ± 6.90	2.9770 ± 0.0069	0.0024 ± 0.0001
15K0088D	49.23 ± 5.78	0.1198 ± 0.0141	32.44 ± 3.81	57.92 ± 11.34	2.7147 ± 0.0068	0.0023 ± 0.0001
15K0088E	63.85 ± 6.42	0.1554 ± 0.0156	41.18 ± 4.14	73.17 ± 13.77	2.6571 ± 0.0063	0.0020 ± 0.0001
15K0088F	47.19 ± 5.30	0.1148 ± 0.0129	29.60 ± 3.33	73.38 ± 13.32	2.5838 ± 0.0064	0.0024 ± 0.0001
15K0088G	65.78 ± 6.19	0.1601 ± 0.0151	39.20 ± 3.69	58.95 ± 7.12	2.4546 ± 0.0053	0.0021 ± 0.0001
15K0088H	59.36 ± 5.37	0.1445 ± 0.0131	35.51 ± 3.22	109.34 ± 27.18	2.4637 ± 0.0064	0.0022 ± 0.0001
15K0088I	69.51 ± 11.96	0.1692 ± 0.0291	26.21 ± 4.51	118.74 ± 69.31	1.5518 ± 0.0045	0.0025 ± 0.0002
15K0088J	56.84 ± 7.04	0.1383 ± 0.0171	26.09 ± 3.23	50.07 ± 7.79	1.8897 ± 0.0043	0.0025 ± 0.0001
15K0088K	56.05 ± 10.98	0.1364 ± 0.0267	23.22 ± 4.55	11.46 ± 0.87	1.7054 ± 0.0040	0.0026 ± 0.0002
15K0088L	55.08 ± 6.81	0.1340 ± 0.0166	31.15 ± 3.85	84.88 ± 15.39	2.3290 ± 0.0056	0.0023 ± 0.0001
15K0088M	54.61 ± 5.25	0.1329 ± 0.0128	38.12 ± 3.66	56.15 ± 6.65	2.8762 ± 0.0068	0.0021 ± 0.0001
15K0088N	44.32 ± 7.61	0.1079 ± 0.0185	23.89 ± 4.10	67.94 ± 16.29	2.2192 ± 0.0048	0.0026 ± 0.0001
15K0088O	61.15 ± 5.91	0.1488 ± 0.0144	34.31 ± 3.31	65.61 ± 10.07	2.3106 ± 0.0048	0.0022 ± 0.0001
15K0088P	48.96 ± 6.59	0.1192 ± 0.0160	28.93 ± 3.89	73.57 ± 13.84	2.4337 ± 0.0061	0.0024 ± 0.0001
15K0088Q	48.19 ± 5.91	0.1173 ± 0.0144	30.57 ± 3.75	79.35 ± 16.86	2.6132 ± 0.0061	0.0023 ± 0.0001
15K0088R	50.91 ± 10.26	0.1239 ± 0.0250	24.30 ± 4.90	75.02 ± 14.77	1.9653 ± 0.0054	0.0026 ± 0.0002
15K0088S	52.34 ± 6.85	0.1274 ± 0.0167	32.82 ± 4.30	64.78 ± 9.44	2.5830 ± 0.0065	0.0023 ± 0.0001
15K0088T	43.05 ± 7.93	0.1048 ± 0.0193	21.97 ± 4.05	97.61 ± 30.71	2.1012 ± 0.0060	0.0026 ± 0.0001

Appendix 4 (continued)

Exp #	Apparent age (ka)	$^{40}\text{Ar}^*/^{39}\text{Ar}_K$	% $^{40}\text{Ar}^*$	K/Ca	$^{39}\text{Ar}/^{40}\text{Ar}$	$^{36}\text{Ar}/^{40}\text{Ar}$
<b>Dome 31, sample 14MCM12</b>						
Packet IRR332-YS, single-crystal sanidine						
$J = 0.00022653940694861 \pm 0.0000002727 (1\sigma)$						
15K0027A	23.46 ± 19.70	0.0574 ± 0.0482	6.50 ± 5.45	89.26 ± 15.25	1.1328 ± 0.0026	0.0032 ± 0.0002
15K0027B	47.68 ± 20.61	0.1167 ± 0.0504	11.71 ± 5.06	59.58 ± 10.58	1.0047 ± 0.0027	0.0030 ± 0.0002
15K0027C	21.88 ± 16.79	0.0535 ± 0.0411	7.05 ± 5.41	49.83 ± 5.46	1.3186 ± 0.0034	0.0031 ± 0.0002
15K0027D	9.87 ± 46.94	0.0242 ± 0.1148	1.29 ± 6.15	56.24 ± 14.85	0.5354 ± 0.0020	0.0033 ± 0.0002
15K0027E	-5.44 ± 37.16	-0.0133 ± 0.0909	-0.67 ± 4.59	88.62 ± 21.78	0.5054 ± 0.0014	0.0034 ± 0.0002
15K0027F	54.49 ± 28.10	0.1333 ± 0.0687	5.15 ± 2.65	92.54 ± 38.66	0.3862 ± 0.0008	0.0032 ± 0.0001
15K0027G	65.85 ± 17.36	0.1611 ± 0.0425	10.58 ± 2.79	54.41 ± 7.94	0.6569 ± 0.0011	0.0030 ± 0.0001
15K0027H	16.87 ± 25.28	0.0413 ± 0.0619	2.12 ± 3.17	56.70 ± 14.46	0.5129 ± 0.0012	0.0033 ± 0.0001
15K0027I	36.19 ± 25.42	0.0885 ± 0.0622	6.59 ± 4.63	53.33 ± 7.15	0.7450 ± 0.0021	0.0032 ± 0.0002
15K0027J	98.20 ± 45.64	0.2403 ± 0.1117	10.99 ± 5.11	96.78 ± 46.41	0.4577 ± 0.0015	0.0030 ± 0.0002
15K0027K	32.03 ± 16.74	0.0784 ± 0.0409	9.35 ± 4.88	72.41 ± 18.18	1.1940 ± 0.0030	0.0031 ± 0.0002
15K0027L	23.53 ± 24.34	0.0576 ± 0.0595	5.52 ± 5.71	66.68 ± 19.64	0.9596 ± 0.0026	0.0032 ± 0.0002
15K0027M	19.35 ± 19.45	0.0473 ± 0.0476	4.56 ± 4.59	60.74 ± 8.83	0.9647 ± 0.0025	0.0032 ± 0.0002
15K0027N	45.93 ± 39.59	0.1124 ± 0.0969	5.65 ± 4.87	50.81 ± 17.07	0.5031 ± 0.0018	0.0032 ± 0.0002
15K0027O	7.64 ± 27.24	0.0187 ± 0.0667	1.49 ± 5.30	63.96 ± 12.23	0.7953 ± 0.0022	0.0033 ± 0.0002
15K0027P	22.39 ± 20.76	0.0548 ± 0.0508	4.49 ± 4.16	65.10 ± 12.63	0.8199 ± 0.0017	0.0032 ± 0.0001
15K0027Q	16.67 ± 31.52	0.0408 ± 0.0771	2.36 ± 4.46	85.90 ± 58.58	0.5781 ± 0.0016	0.0033 ± 0.0002
15K0027R	-25.66 ± 31.31	-0.0628 ± 0.0766	-3.09 ± 3.76	63.99 ± 12.30	0.4916 ± 0.0012	0.0035 ± 0.0001
15K0027S	65.60 ± 26.22	0.1605 ± 0.0642	6.85 ± 2.74	68.25 ± 15.34	0.4268 ± 0.0010	0.0032 ± 0.0001
15K0027T	29.55 ± 15.43	0.0723 ± 0.0378	7.82 ± 4.08	65.43 ± 16.66	1.0823 ± 0.0026	0.0031 ± 0.0001
15K0027U	87.32 ± 42.25	0.2137 ± 0.1034	9.46 ± 4.58	134.11 ± 77.26	0.4428 ± 0.0015	0.0031 ± 0.0002
15K0027V	18.02 ± 33.91	0.0441 ± 0.0830	2.50 ± 4.71	149.96 ± 79.63	0.5680 ± 0.0014	0.0033 ± 0.0002
15K0027W	46.62 ± 28.67	0.1141 ± 0.0701	8.38 ± 5.15	53.55 ± 7.99	0.7348 ± 0.0023	0.0031 ± 0.0002
15K0027X	10.05 ± 27.16	0.0246 ± 0.0665	1.25 ± 3.37	66.41 ± 9.14	0.5070 ± 0.0014	0.0033 ± 0.0001
15K0027Y	10.55 ± 39.61	0.0258 ± 0.0969	0.54 ± 2.04	55.84 ± 9.51	0.2107 ± 0.0004	0.0034 ± 0.0001
15K0028A	33.83 ± 26.81	0.0828 ± 0.0656	1.40 ± 1.11	48.62 ± 9.39	0.1687 ± 0.0003	0.0033 ± 0.0000
15K0028B	21.03 ± 72.98	0.0515 ± 0.1786	0.22 ± 0.77	62.21 ± 24.46	0.0431 ± 0.0001	0.0034 ± 0.0000
15K0028C	-71.74 ± 64.90	-0.1755 ± 0.1588	-1.50 ± 1.36	55.54 ± 14.41	0.0853 ± 0.0002	0.0034 ± 0.0000
15K0028D	84.18 ± 40.41	0.2060 ± 0.0989	4.23 ± 2.03	42.80 ± 9.48	0.2054 ± 0.0005	0.0032 ± 0.0001
15K0028E	31.02 ± 25.20	0.0759 ± 0.0617	6.95 ± 5.65	140.72 ± 60.11	0.9167 ± 0.0024	0.0031 ± 0.0002

All uncertainties are give at  $1\sigma$ . Apparent age does not include uncertainty in the J-value. All ratios are corrected for blank, background, mass discrimination, interference reactions, and radioactive decay. Experiments in red are not included in the age calculation because of low K/Ca (<20) and negative radiogenic yield (%  $^{40}\text{Ar}^*$ ). Exp #: experiment number;  $^{40}\text{Ar}^*$ : radiogenic argon;  $^{39}\text{Ar}_K$ : argon derived from neutron bombardment of  $^{39}\text{K}$ .

## Appendix 5. Sanidine <sup>40</sup>Ar/<sup>39</sup>Ar furnace incremental-heating data.

**Dome 19, sample 11JAVM06**

Temp(°C)	Age (ka)	% <sup>40</sup> Ar*	K/Ca	K/Cl	moles <sup>40</sup> Ar*	Σ <sup>39</sup> Ar	<sup>40</sup> Ar	<sup>39</sup> Ar	<sup>38</sup> Ar	<sup>37</sup> Ar	<sup>36</sup> Ar
650	-5.4±103.5	-0.07	0.66	97	-1.92E-17	0	0.181649±0.000211	0.009842±0.000163	0.000680±0.000068	0.007776±0.000659	0.000617±0.000008
750	41.8±31.4	1.88	8.06	491	3.73E-16	0.01	0.133830±0.000185	0.024799±0.000104	0.000626±0.000052	0.001614±0.000399	0.000445±0.000006
850	45.9±13.8	5.36	8.77	1221	1.09E-15	0.03	0.136941±0.000396	0.065877±0.000125	0.001179±0.000060	0.003942±0.000338	0.000439±0.000007
925	25.2±11.2	4.18	17.28	2292	7.36E-16	0.06	0.119044±0.000234	0.081311±0.000127	0.001293±0.000043	0.002469±0.000179	0.000386±0.000007
1000	38.0±5.0	11	14.66	3517	2.20E-15	0.1	0.135387±0.000211	0.161410±0.000171	0.002394±0.000053	0.005777±0.000257	0.000409±0.000007
1075	35.2±3.6	15.53	33.39	14615	3.69E-15	0.19	0.160613±0.000139	0.291799±0.000217	0.004006±0.000057	0.004586±0.000336	0.000459±0.000009
1150	48.3±1.9	25.9	44.79	45252	7.91E-15	0.33	0.206347±0.000148	0.455183±0.000232	0.006121±0.000047	0.005332±0.000134	0.000517±0.000007
1225	47.4±1.5	34.4	20.9	-53746	9.58E-15	0.5	0.188057±0.000141	0.562133±0.000341	0.007420±0.000069	0.014111±0.000144	0.000420±0.000007
1300	52.2±1.0	49.7	14.47	-11496	1.55E-14	0.75	0.210984±0.000119	0.826166±0.000381	0.010615±0.000035	0.029959±0.000388	0.000365±0.000007
1375	51.9±1.5	42.69	16.42	-12042	9.21E-15	0.9	0.145846±0.000107	0.493514±0.000287	0.006362±0.000043	0.015766±0.000553	0.000286±0.000006
1450	56.1±3.2	27.08	8.48	-17288	4.40E-15	0.97	0.109675±0.000103	0.217755±0.000180	0.002858±0.000030	0.013480±0.000126	0.000274±0.000006
1500	56.9±7.1	14.76	8.54	-82908	2.15E-15	1	0.098428±0.000138	0.105087±0.000122	0.001429±0.000031	0.006460±0.000101	0.000285±0.000006

Packet IRR332-YP, Experiment #15Z0062, 0.0514 g Sanidine, all errors ±1σ

J = 0.0002280436734±5.4648E-07

<sup>40</sup>Ar\* is radiogenic argon, isotopes in volts (1.48e-13 moles/volt), corrected for blank, background, discrimination, and decay  
 Calculated bulk K/Ca = 15.537 ± 31.116, Calculated K<sub>2</sub>O = 16.02 wt%, Calculated CaO = 1.26 wt%, Calculated Cl = 1.0ppm

Total gas age = 48.0 ± 1.8 ka (2σ)

Weighted mean plateau age = 52.4 ± 1.6 ka (95% confidence, including ± J), 50% of <sup>39</sup>Ar released

MSWD 0.63 (good fit, MSWD < 3.117)

Steps 9-12 (1300, 1375, 1450, 1500 °C)

Isochron age (plateau-steps only) = 50.8 ± 3.3 ka (95% confidence, including ± J)

MWSD 0.24 (good fit, MSWD < 3.69)

<sup>40</sup>Ar/<sup>36</sup>Ar intercept = 303 ± 12 (95% confidence)

Apparent isochron age (all steps) = 51.9 ± 3.8 ka (95% confidence, including ± J)

MSWD 3.5 (poor fit, MSWD > 2.05)

<sup>40</sup>Ar/<sup>36</sup>Ar intercept = 289.7 ± 8.4 (95% confidence)

Appendix 5 (continued)

Dome 31, sample 14MCGMM12											
Temp(°C)	Age (ka)	% <sup>40</sup> Ar*	K/Ca	K/Cl	moles <sup>40</sup> Ar*	Σ <sup>39</sup> Ar	<sup>40</sup> Ar	<sup>39</sup> Ar	<sup>38</sup> Ar	<sup>37</sup> Ar	<sup>36</sup> Ar
650	-1.49.5±58.3	-3.51	2.63	127	-1.05E-15	0.01	0.202425±0.000304	0.0194659±0.000193	0.001045±0.000125	0.003890±0.000940	0.000710±0.000009
750	-49.5±35.8	-1.76	6.28	301	-4.45E-16	0.01	0.170728±0.000157	0.024896±0.000132	0.000792±0.000059	0.002080±0.000450	0.000588±0.000007
850	30.1±19.4	2.86	11.43	4648	7.31E-16	0.03	0.172608±0.000243	0.067248±0.000133	0.001052±0.000035	0.003086±0.000108	0.000568±0.000011
925	-2.0±7.9	-0.32	18	2694	-8.91E-17	0.06	0.188494±0.000186	0.120606±0.000151	0.001897±0.000062	0.003516±0.000405	0.000640±0.000008
1000	20.0±5.6	4.13	36.28	6928	1.20E-15	0.11	0.197200±0.000144	0.166534±0.000155	0.002411±0.000060	0.002408±0.000228	0.000640±0.000008
1075	21.5±3.2	7.47	42.24	13808	2.27E-15	0.19	0.205308±0.000147	0.292466±0.000247	0.004054±0.000051	0.003633±0.000310	0.000643±0.000008
1150	25.8±1.8	14.46	48.99	125413	4.35E-15	0.31	0.203376±0.000127	0.466573±0.000235	0.006257±0.000054	0.004997±0.000308	0.000589±0.000007
1225	29.9±1.6	17.29	39.64	-70460	6.38E-15	0.47	0.249353±0.000166	0.591593±0.000298	0.007868±0.000066	0.007830±0.000239	0.000688±0.000008
1300	36.2±0.9	31.15	26.65	-12209	1.20E-14	0.72	0.259903±0.000152	0.916119±0.000348	0.011829±0.000068	0.018036±0.000295	0.000607±0.000007
1375	30.2±1.3	26.6	23.02	-13206	6.54E-15	0.89	0.166139±0.000119	0.600065±0.000350	0.007767±0.000062	0.013679±0.000236	0.000414±0.000006
1450	32.4±2.7	17.61	31.75	-21177	3.75E-15	0.97	0.143848±0.000145	0.320265±0.000206	0.004218±0.000054	0.005293±0.000206	0.000401±0.000007
1500	26.3±7.5	5	13.52	-523894	9.64E-16	1	0.130320±0.000111	0.101497±0.000094	0.001411±0.000023	0.003940±0.000093	0.000420±0.000006

Packet IRR332-YR, Experiment #15Z0063; 0.0553 g Sanidine, all errors ±1σ  
 J = 0.0002271899948±3.4001E-07

<sup>40</sup>Ar\* is radiogenic argon, isotopes in volts (1.48e-13 moles/volt), corrected for blank, background, discrimination, and decay  
 Calculated bulk K/Ca = 26.727 ± 69.148, Calculated K<sub>2</sub>O = 16.72 wt%, Calculated CaO = 0.77 wt%, Calculated Cl = 1.0ppm

Total gas age = 27.5 ± 1.6 ka (2σ)

No plateau

Apparent isochron age (all steps) = 36.3 ± 3.8 ka (95% confidence, including ±J)

MSWD 3.5 (poor fit, MSWD > 1.991)

<sup>40</sup>Ar/<sup>36</sup>Ar intercept = 283.4 ± 6.9 (95% confidence)

Appendix 6. Sanidine chemistry of dome 19 (sample 11JAVMC06).

Analysis ID	Grain no.	SiO <sub>2</sub>	Al <sub>2</sub> O <sub>3</sub>	BaO	CaO	Na <sub>2</sub> O	K <sub>2</sub> O	Total	% Or content
MC06fspar-1	1	65.41	18.98	0.69	0.19	3.31	11.57	100.15	69
MC06fspar-2	1	65.60	18.84	0.57	0.17	3.27	11.64	100.08	69
MC06fspar-3	1	65.94	18.78	0.48	0.16	3.26	11.75	100.36	70
MC06fspar-4	1	65.53	18.80	0.51	0.16	3.32	11.71	100.02	69
MC06fspar-5	2	65.49	19.13	1.13	0.23	3.53	11.25	100.75	67
MC06fspar-6	2	65.22	19.13	1.22	0.19	3.47	11.10	100.32	67
MC06fspar-7	2	64.90	19.02	1.09	0.21	3.41	11.10	99.73	67
MC06fspar-8	3	65.41	18.93	0.62	0.20	3.30	11.43	99.88	69
MC06fspar-9	3	65.06	18.96	0.63	0.21	3.41	11.36	99.62	68
MC06fspar-10	4	65.37	19.17	1.05	0.21	3.57	11.26	100.64	67
MC06fspar-11	4	65.19	19.05	0.92	0.21	3.38	11.17	99.93	68
MC06fspar-31	5	65.70	18.71	0.41	0.14	3.21	11.77	99.95	70
MC06fspar-32	5	65.82	18.71	0.43	0.13	3.21	12.01	100.31	71
MC06fspar-33	5	65.75	18.80	0.36	0.17	3.22	11.87	100.18	70
MC06fspar-34	5	66.25	18.90	0.43	0.14	3.30	11.93	100.95	70
MC06fspar-35	5	66.05	18.93	0.42	0.17	3.25	11.88	100.70	70
MC06fspar-38	6	65.67	18.90	0.79	0.19	3.52	11.38	100.44	67
MC06fspar-39	6	66.35	18.93	0.38	0.18	3.46	11.59	100.89	68
MC06fspar-40	7	65.64	18.95	0.67	0.18	3.51	11.35	100.30	67
MC06fspar-41	7	66.13	18.88	0.42	0.22	3.53	11.50	100.68	67
MC06fspar-42	8	66.36	19.10	0.70	0.22	3.53	11.41	101.32	67
MC06fspar-43	8	65.70	19.01	0.69	0.19	3.43	11.56	100.58	68
MC06fspar-44	9	66.16	18.96	0.64	0.19	3.42	11.53	100.90	68
MC06fspar-45	9	65.79	19.02	0.71	0.20	3.46	11.44	100.61	68
MC06fspar-46	9	65.94	18.75	0.46	0.17	3.42	11.57	100.30	68
MC06fspar-47	9	66.22	18.77	0.40	0.15	3.42	11.59	100.55	69
MC06fspar-48	10	65.79	19.02	0.65	0.19	3.41	11.55	100.61	68
MC06fspar-49	10	65.57	18.95	0.71	0.19	3.35	11.49	100.25	69
MC06fspar-50	10	65.55	18.95	0.68	0.22	3.36	11.37	100.13	68
MC06fspar-51	11	66.10	19.02	0.58	0.15	3.15	11.88	100.88	71
MC06fspar-52	11	65.90	18.99	0.49	0.16	3.26	11.86	100.67	70
MC06fspar-53	11	65.28	18.77	0.44	0.18	3.23	11.77	99.66	70
MC06fspar-56	12	65.38	18.97	0.72	0.22	3.47	11.41	100.17	68
MC06fspar-57	12	65.12	18.95	0.71	0.19	3.45	11.36	99.78	68
MC06fspar-58	12	65.08	18.90	0.72	0.21	3.40	11.43	99.73	68
MC06fspar-59	12	64.97	18.62	0.71	0.21	3.36	11.51	99.38	69
MC06fspar-60	13	65.25	18.84	0.44	0.15	3.17	11.95	99.80	71
MC06fspar-61	13	65.42	18.74	0.42	0.14	3.14	11.87	99.72	71
MC06fspar-62	14	65.57	18.77	0.50	0.17	3.24	11.84	100.08	70
MC06fspar-63	14	65.59	18.66	0.46	0.17	3.17	11.81	99.85	70
MC06fspar-64	14	65.59	18.83	0.50	0.15	3.25	11.86	100.17	70
MC06fspar-65	15	65.46	18.93	0.73	0.21	3.38	11.42	100.12	68
MC06fspar-66	15	65.49	18.94	0.62	0.20	3.28	11.49	100.02	69
MC06fspar-67	16	65.47	18.88	0.43	0.19	3.38	11.67	100.02	69
MC06fspar-68	16	65.44	18.93	0.68	0.19	3.28	11.52	100.03	69
MC06fspar-69	16	65.59	19.01	0.66	0.18	3.42	11.46	100.33	68
MC06fspar-70	16	65.74	18.81	0.49	0.15	3.30	11.74	100.24	70
MC06fspar-71	16	65.68	18.83	0.44	0.16	3.30	11.67	100.07	69

Appendix 6 (continued)

Analysis ID	Grain no.	SiO <sub>2</sub>	Al <sub>2</sub> O <sub>3</sub>	BaO	CaO	Na <sub>2</sub> O	K <sub>2</sub> O	Total	% Or content
MC06fspar-72	17	65.25	18.99	0.61	0.19	3.27	11.59	99.91	69
MC06fspar-73	17	65.32	18.76	0.63	0.16	3.23	11.52	99.61	70
MC06fspar-74	17	65.60	18.94	0.59	0.18	3.41	11.43	100.15	68
MC06fspar-75	17	65.63	19.08	0.69	0.21	3.60	11.27	100.48	67
MC06fspar-76	17	65.56	18.94	0.69	0.18	3.43	11.45	100.26	68
MC06fspar-81	18	65.67	19.02	0.63	0.19	3.37	11.59	100.47	69
MC06fspar-82	18	65.66	18.99	0.69	0.19	3.33	11.49	100.35	69
MC06fspar-83	18	65.62	18.77	0.51	0.17	3.38	11.54	99.99	69
MC06fspar-84	18	65.67	18.77	0.51	0.16	3.25	11.65	100.01	70
MC06fspar-85	19	65.59	19.08	0.91	0.20	3.41	11.37	100.56	68
MC06fspar-86	19	65.62	19.02	0.96	0.20	3.38	11.30	100.48	68
MC06fspar-87	19	66.16	19.00	0.51	0.17	3.45	11.57	100.86	68
MC06fspar-88	19	65.54	18.82	0.53	0.19	3.38	11.50	99.95	68
Line 1 MC06fspar-89	20	65.00	19.12	0.97	0.22	3.57	11.19	100.06	67
Line 2 MC06fspar-90	20	65.03	19.05	0.98	0.24	3.60	11.03	99.93	66
Line 2 MC06fspar-91	20	64.88	19.05	0.82	0.21	3.55	11.08	99.60	67
Line 2 MC06fspar-92	20	65.05	19.06	0.65	0.22	3.55	11.16	99.69	67
Line 2 MC06fspar-93	20	65.81	18.90	0.58	0.18	3.53	11.40	100.38	67
Line 2 MC06fspar-94	20	65.69	18.93	0.65	0.22	3.58	11.24	100.31	67
Line 2 MC06fspar-95	20	65.38	18.83	0.64	0.21	3.51	11.22	99.79	67
Line 2 MC06fspar-96	20	65.20	19.10	0.96	0.25	3.51	11.11	100.13	67
Line 2 MC06fspar-97	20	65.38	19.14	0.90	0.23	3.46	11.07	100.18	67
Line 2 MC06fspar-98	20	65.23	18.99	0.94	0.22	3.49	11.19	100.05	67
MC06fspar-99	21	65.01	18.86	0.68	0.20	3.41	11.43	99.59	68
MC06fspar-100	21	65.55	18.79	0.53	0.19	3.45	11.35	99.86	68
MC06fspar-101	22	65.67	19.02	0.67	0.21	3.48	11.35	100.40	67
MC06fspar-102	22	65.72	19.00	0.82	0.20	3.41	11.32	100.47	68
MC06fspar-103	22	65.47	18.97	0.61	0.18	3.36	11.65	100.24	69
MC06fspar-104	23	65.43	18.91	0.63	0.20	3.50	11.38	100.05	67
MC06fspar-105	23	65.53	18.95	0.73	0.22	3.57	11.22	100.22	67
MC06fspar-106	23	65.36	19.00	0.64	0.19	3.39	11.43	100.01	68
MC06fspar-110	24	65.21	18.87	0.67	0.19	3.41	11.44	99.79	68
MC06fspar-111	24	65.08	18.96	0.70	0.21	3.42	11.38	99.74	68
MC06fspar-112	24	65.26	18.91	0.68	0.21	3.48	11.33	99.87	67
MC06fspar-113	25	65.25	18.85	0.73	0.16	3.36	11.42	99.77	69
MC06fspar-114	25	65.11	18.96	0.91	0.19	3.46	11.20	99.83	67
MC06fspar-115	25	65.98	18.64	0.41	0.16	3.55	11.24	99.99	67
MC06fspar-116	26	65.63	18.96	0.73	0.20	3.44	11.45	100.41	68
MC06fspar-117	26	65.39	18.86	0.50	0.18	3.42	11.35	99.70	68
MC06fspar-118	26	65.36	18.80	0.45	0.16	3.39	11.45	99.59	68

Run conditions: 20 nA beam current, 5 µm beam, background every 3rd point.

Silicate standards: Or1, An100, Tiburon albite, barite; standards ran every 50 points.